THE USE OF CANTILEVERS AS BLAST WAVE GAUGES

by

Alexander Antony van Netten
B.Sc., University of Victoria, 1985
M.Sc., University of Victoria, 1988

A Dissertation Submitted in Partial Fulfillment of the
Requirements for the Degree of

DOCTOR OF PHILOSOPHY

in the Department of Physics and Astronomy

We accept this dissertation as conforming
to the required standard

Dr. J.M. Dewey, Supervisor (Department of Physics and Astronomy)

Dr. R.M. Clements, Departmental Member (Department of Physics and Astronomy)

Dr. G.D. Spence, Departmental Member (Department of Physics and Astronomy)

Dr. G.W. Vickers, Outside Member (Department of Mechanical Engineering)

Dr. J.B. Haddow, Outside Member (Department of Mechanical Engineering)

Dr. D.K. Walker, Additional Member (Department of Physics and Astronomy)

Dr. J.J. Gottlieb, External Examiner (Institute for Aerospace Studies, U. of Toronto)

©ALEXANDER ANTONY VAN NETTEN, 1995
UNIVERSITY OF VICTORIA
All rights reserved. This dissertation may not be reproduced in whole or in part, by photocopying or other means, without the permission of the author.

Abstract

A study has been made of the response of elastic-plastic and brittle cantilevers when subjected to blast wave loading with a view to using such devices as passive blast wave gauges, and of using the deformation of cantilevers to assess the characteristics of accidental explosions.

The study was restricted to cantilevers that were circular in cross-section and made of readily available materials. A cantilever, when loaded by a blast wave, either deforms plastically, in which case the amount of deformation is the critical parameter, or fractures, in which case the failing or not failing of the cantilever provides the required information.

Two numerical models were developed to describe the deformation of a dynamically loaded cantilever. Both models assume that the plastic deformation is localized in a region near the fixed end, and that the loading force was a function of the dynamic pressure time history and a variable drag coefficient, dependent on the Reynolds number, Mach number and angle of attack.

The first numerical model assumed a rigid-plastic response of the cantilevers. The model accurately described the response only of cantilevers made of 50/50 lead/tin alloy. It overestimated the deformation of cantilevers made of other materials exposed in both high explosive and shock tube experiments.

The second model assumed an elastic-plastic response for the blast loaded cantilever with strain hardening effects included. The algorithm was based on the premise that the elastic curvature of the cantilever was limited by the plastic yield stress of the material and that as the curvature approached this limit the cantilever was rotated by the necessary amount to keep the curvature constant and equal to this maximum. The amount of rotation was determined by fitting a fourth order polynomial with a constrained second derivative based on the maximum allowed curvature. The rotation angle was found from the angle derived from the slope of the fitted function at the origin. A rotation by this angle yields a minimum in curvature in the rotated reference frame. This model improved the predictions for cantilevers constructed of aluminum and steel.

The numerical models were evaluated by studying the response of cantilevers exposed to shock waves produced in a shock tube, and to blast waves produced

by the detonation of two large high-explosive chemical sources. The response of the cantilevers to the shock tube flows was recorded by high-speed photography which showed good agreement between the observed modes of deformation and those predicted by the model. The models which were finally developed also provided good predictions of the deformation or fracture of a wide range of cantilevers exposed to the free-field blast waves. These models were also used to detect any non-radial flows and to study the boundary layers in the blast wave over different surfaces.

Finally, it is demonstrated how the numerical modelling can be used to determine the type of cantilever that might be used as a passive gauge for monitoring the blast wave from an explosive event, and for evaluating the deformation of a cantilever exposed to the blast wave from an accidental explosion so as to characterize that explosion.

Examiners:

Dr. J.M. Dewey, Supervisor (Department of Physics and Astronomy)

Dr. R.M. Clements, Departmental Member (Department of Physics and Astronomy)

Dr. G.D. Spence, Departmental Member (Department of Physics and Astronomy)

Dr. G.W. Vickers, Outside Member (Department of Mechanical Engineering)

Dr. J.B. Haddow, Outside Member (Department of Mechanical Engineering)

Dr. D.K. Walker, Additional Member (Department of Physics and Astronomy)

Dr. J.J. Gottlieb, External Examiner (Institute for Aerospace Studies, U. of Toronto)

Table of Contents

List of Tables

List of Figures

Acknowledgements

I wish to thank Dr. John Dewey for his encouragement and guidance in the supervision of this project. He gave me the opportunity to work in a field that I had always wanted. I remember the day that I first walked into his office and saw the photographs on the wall and I said to myself, "This is what I want to do".

I also wish to thank Arnfinn Jenssen of the Norwegian Defence Construction Service without whose financial and enthusiastic support this project would not have been pursued. When anything was needed Arnfinn always came through. Special thanks are due to Theodore von Haimberger for his most valuable discussions and allowing me to bounce any idea off him, no matter how crazy.

Chapter 1

Introduction

Lord Penny(1969) determined the effective energy yields of the explosions which occurred at Hiroshima and Nagasaki in 1945 by observing the damage that occurred to various simple structures that surrounded the explosions. These structures included bent or broken poles, toppled gravestones, crushed paint cans, broken glass windows, dished in cabinet walls, etc. By understanding the modes of failure of these structures he related the damage to the various blast wave properties which in turn could be used to determine the energy yields of the explosion.

The ideas developed by Penny were later used by other researchers to develop a series of passive gauges. These gauges are in general simple in design and have modes of failure that can be easily related to some property of the blast wave. Many of these gauges are currently being used at various high explosive events as a less expensive alternative to electronic devices. For example, Ewing et al (1957) and Baker et al (1958) used cantilevers with rectangular cross-section around various charges to calibrate these gauges in the impulsively loaded regime; Dewey(1962) studied the deformation of solder cantilevers surrounding TNT and ammonium nitrate/fuel oil (ANFO) explosions to determine the uniformity and efficiency of these events; Binninger et al (1981,1983) and Deel (1984) used cantilevers constructed of I-beams, also in the impulsively loaded regime, to measure the effects of dust and height of burst on the dynamic pressure impulse exerted on the cantilever; Ethridge(1992) related

the displacement of cubes constructed of different materials to the dynamic pressure impulse imparted from a 2.650 kt ANFO explosion(DISTANT IMAGE), and van Netten et al(1992) used cantilevers with circular cross-sections and constructed of different materials to measure the variation of dynamic pressure with distance from the charge and height above the ground at the same event.

Blast waves are produced by the rapid expansion of material within an atmosphere. The expansion produces a pressure wave which eventually steepens as it propagates until it exhibits a nearly discontinuous increase in pressure, density and temperature. The air molecules are also accelerated by the discontinuity, in a radial direction away from the explosion center. In order to predict the damage that may occur it is necessary to measure these various physical properties.

The most frequently used method of measuring the blast pressures from explosions or shock tube flows uses the output from a piezoelectric transducer in conjunction with an appropriate amplifier and data storage system. Such instrumentation, which is both complex and expensive, provides an excellent recording of the pressure-time history during the passage of the blast wave. These gauges require the knowledge of two essential parameters: an approximate value of the expected pressure so that the gain of the amplifiers can be set, and a estimate of the time of arrival of the shock so that the storage system can begin acquiring data. In addition the measurement of dynamic pressure requires an exact knowledge of the flow direction so that the transducers can be orientated correctly. In situations where these parameters are not well known or where a large number of measurements are required, techniques using passive gauges, such as those previously described, may be preferred.

Passive gauges are particularly useful in situations where a large number of gauges are required to map a non-symmetrical blast field. Examples are the blast waves emerging from a tunnel entrance, or tests where the uniformity of the blast wave is not known. A knowledge of the relationship between blast wave properties and

the resulting deformation, displacement or damage to simple structures is also useful when studying the damage due to an accidental explosion since such structures can be usually found.

The work presented here deals mainly with the bending or breaking of cylindrical cantilevers when subjected to loading by blast and shock waves, and relates the damage to the blast wave properties. The cantilevers were subjected to the loading produced by blast waves created in a shock tube and by the detonation of two large ammonium nitrate/fuel-oil(ANFO) explosive charges with masses of 2,650 tons (DISTANT IMAGE,1991) and 2,431 tons (MINOR UNCLE,1993). Numerical models were developed to predict the deformation of cantilevers under shock wave loading. High speed photography was used to record the time history of the deformation of various cantilevers subjected to shock tube flows and these results were compared to the predictions of the various numerical models. These same numerical models were also used to predict the responses of a large number of cantilevers of various sizes and materials exposed in the blast waves produced by the ANFO explosions.

The main objectives of the project described in this dissertation are: to understand the relationships between the physical properties of shock and blast waves and the response of circular cross-section cantilevers exposed to those waves, to use that understanding to design cantilever gauges that can be used to monitor the physical properties of blast waves, and, to illustrate how the deformation of cantilever structures may be used to describe the source of blast waves produced by accidental explosions.

Chapter 2 of this dissertation presents a brief description of the properties of blast waves caused by the detonation of a high explosive and of shock waves produced by a shock tube. Chapter 3 describes the numerical models which predict the time-resolved loading on the cantilevers and their subsequent response. The loading on a cantilever depends on two time varying properties, the drag coefficient and the

dynamic pressure. The predicted deformation of the cantilevers was based on three possible types of response: rigid-plastic; elastic-plastic and rigid-brittle. Chapter 4 describes the experimental procedures used in both the shock tube and HE experiments and also details the methods by which the material properties were obtained. Chapter 5 compares the predictions of the numerical models to the results of the experiments and records some blast wave properties attained from the cantilevers at the HE events. Chapter 6 gives a summary of the results with a discussion of the ways in which cantilever gauges might be used to study explosive events.

Chapter 2

Shock and blast waves

2.1 Introduction

Shock waves occur whenever a compressional disturbance of finite amplitude propagates through a medium. The finite compression produces a non-linear wave, the profile of which changes with time, and is characterized by a leading edge known as the shock front, across which there is an almost instantaneous change in the physical properties of the medium. The thickness of the shock front is of the order of 10 to 20 mean free paths and in air at atmospheric pressure this corresponds to a distance of approximately 10^{-5} cm. It is therefore assumed that beyond the molecular level the shock front may be treated as a boundary through which the thermodynamic properties change abruptly.

A blast wave is generated by the rapid release of a centered source of energy which produces a pressure wave of finite amplitude. This pressure wave steepens to form a shock front at its leading edge. The physical properties in a blast wave decay approximately exponentially behind the shock front, similar to the time-history of the pressure as shown in figure 2.1. The magnitude of the pressure jump across the shock front decreases with distance from the explosion center as the blast wave expands in three dimensions.

Shock waves can also be produced in a shock tube(see section 2.3.1), in which a diaphragm separating a high and a low pressure region is ruptured or removed. In

general a shock tube produces a flow similar to that generated by a centered explosion; however, in most cases the time history is such that a region exists where the flow properties remain constant for some time before decaying back to the ambient conditions. A typical shock-tube pressure time history is shown in figure 2.2. The length of the constant flow region is a function of the characteristics of the shock tube, which can be adjusted so that the wave profile is similar to that of a blast wave.

2.2 Shock front equations

The two principal features which describe a blast wave are: the strength of the shock front, defined by the ratio of the magnitudes of a physical property on the two sides of the shock, and the time for the physical property to decay to its ambient value. This is known as the positive duration and is in general, different for each physical property. The changes in properties of a gas as it passes through a shock can be related to one another by the use of the conservation of mass, momentum and energy.

The three conservation equations valid for inviscid compressible flow, in differential form, are:

Mass

$$\frac{\partial \rho}{\partial t} + \nabla \cdot (\rho \vec{V}) = 0; \tag{2.1}$$

Energy

$$\frac{\partial}{\partial t}[\rho(E + \frac{V^2}{2})] + \nabla \cdot [\rho(E + \frac{V^2}{2})\vec{V}] = -\nabla \cdot (p\vec{V}) + \rho\dot{q} + \rho(\vec{f} \cdot \vec{V}), \tag{2.2}$$

and the x and y components of momentum respectively

$$\frac{\partial(\rho u)}{\partial t} + \nabla \cdot (\rho u \vec{V}) = -\frac{\partial p}{\partial x} + \rho f_x,$$

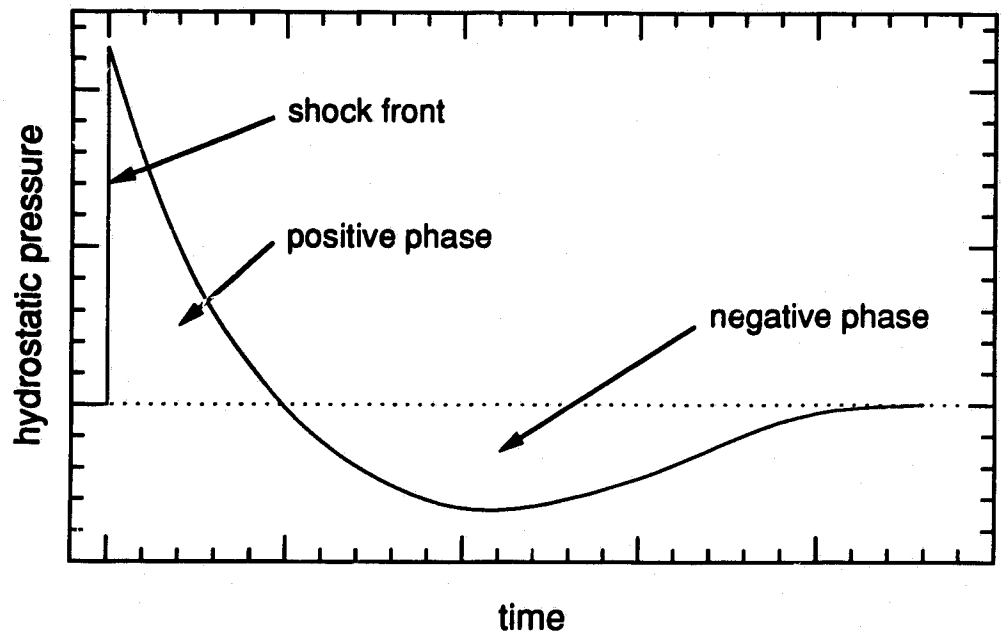

Figure 2.1: Pressure-time history of an ideal blast wave.

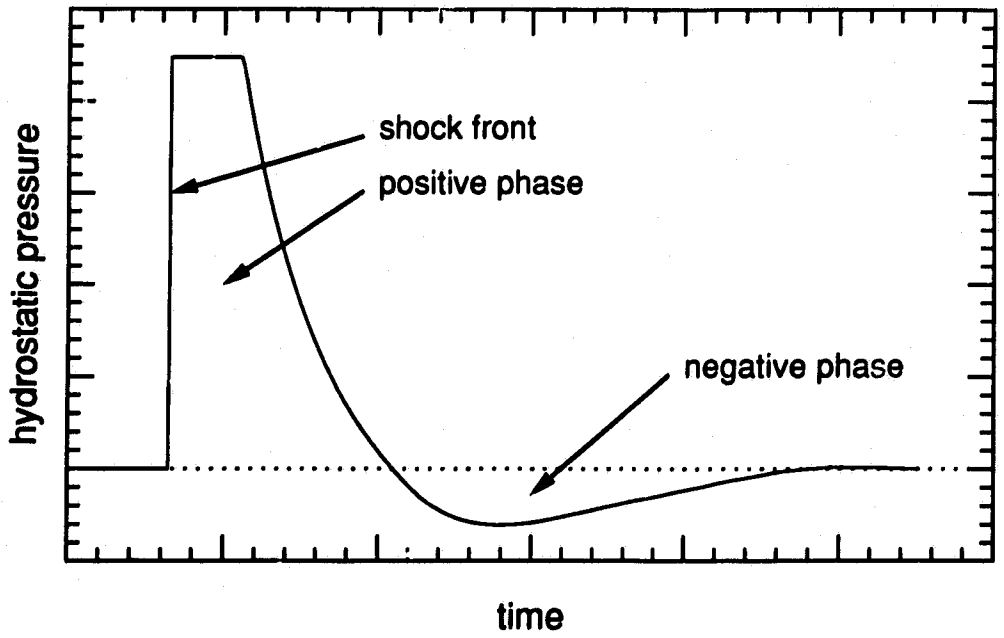

Figure 2.2: Pressure-time history produced by an ideal shock tube.

and

$$\frac{\partial(\rho v)}{\partial t} + \nabla \cdot (\rho v \vec{V}) = -\frac{\partial p}{\partial y} + \rho f_y. \tag{2.3}$$

p and ρ respectively denote the pressure and density; u and v the x and y components of the velocity vector ($\vec{V}$); f_x and f_y the x and y components of the body forces ($\vec{f}$); $\partial/\partial t$ the partial derivative with respect to time; $\dot{q}$ the rate of change of heat per unit mass, and E the internal energy per unit mass.

Rankine(1870) and Hugoniot(1887) solved these equations with the assumption of a thermally and calorically perfect gas with no body forces or heat conduction to produce a set of equations which relate the pressure ($\frac{p_1}{p_0}$), density ($\frac{\rho_1}{\rho_0}$), and temperature ($\frac{T_1}{T_0}$) ratios to the speed of the shock wave, where the subscripts 0 and 1 denote the conditions ahead of and behind the shock front, respectively. As a normal shock wave moves into a region 0 which is a stationary gas with thermodynamic properties p_0, ρ_0, and T_0, it induces a flow in region 1 of speed u and changes the flow properties to p_1, ρ_1, and T_1. The resulting set of equations, known as the Rankine-Hugoniot equations, are:

$$\frac{T_1}{T_0} = \frac{p_1}{p_0}\left(\frac{\frac{\gamma+1}{\gamma-1} + \frac{p_1}{p_0}}{1 + \frac{(\gamma+1)p_1}{(\gamma-1)p_0}}\right), \tag{2.4}$$

$$\frac{\rho_1}{\rho_0} = \frac{1 + \frac{(\gamma+1)p_1}{(\gamma-1)p_0}}{\frac{\gamma+1}{\gamma-1} + \frac{p_1}{p_0}}, \tag{2.5}$$

and

$$u = \frac{a_0}{\gamma}\left(\frac{p_1}{p_0} - 1\right)\left(\frac{\frac{2\gamma}{\gamma+1}}{\frac{p_1}{p_0} + \frac{\gamma-1}{\gamma+1}}\right)^{1/2}, \tag{2.6}$$

where $\gamma = C_p/C_v$ the ratio of specific heats. The above three equations are all functions of the pressure ratio across the shock wave. The pressure ratio can be

expressed as a function of the shock front Mach number M, viz.

$$\frac{p_1}{p_0} = 1 + \frac{2\gamma}{\gamma+1}(M^2 - 1). \tag{2.7}$$

The shock front Mach number M is defined as the ratio of the speed of propagation of the shock, V, to the local speed of sound, a_o.

$$a_0 = \sqrt{\gamma R T_o}, \tag{2.8}$$

where R is the specific gas constant(287 J/(kg K) for air) and T_o is the temperature of the gas in degrees Kelvin in front of the shock wave.

This set of equations describes the relationship between the flow properties on the two sides of a moving normal shock front and its most important feature is that each equation is directly or indirectly completely defined by one parameter, the shock front Mach number. Knowing this parameter and the ambient flow conditions, the conditions immediately behind the shock front can be found.

2.3 Shock waves

2.3.1 Shock tube

The shock waves to which the cantilevers in this study were exposed, were produced in a shock tube and by surface burst chemical explosions. The flows used to load the cantilevers structures under laboratory conditions were generated in a shock tube (Whitten, 1969) with internal cross-sectional dimensions of 7.65 cm by 25.4 cm(see figure 2.3). The shock tube consisted of a 1.05 m long compression chamber and a 7.01 m long expansion chamber that was open to atmosphere. The compression chamber could be filled with air to pressures up to 6 atm. Acetate diaphragms varying in thickness from 0.1 mm to 0.4 mm, were used to separate the two chambers and could be burst with a needle driven by a solenoid. When

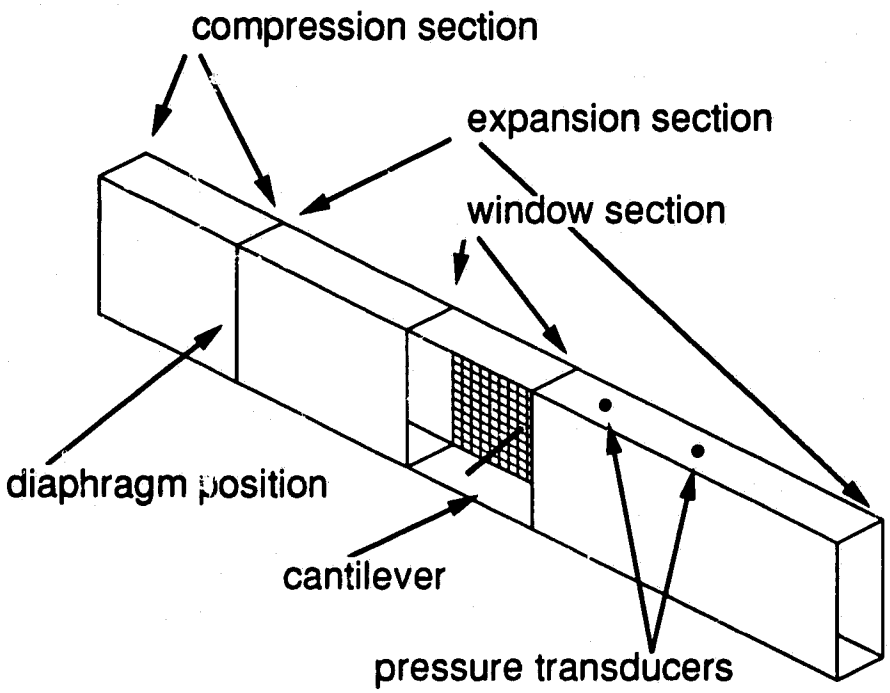

Figure 2.3: Shock tube layout showing cantilever position (not to scale).

the diaphragm was broken a shock wave propagated down the expansion section. A window section was placed 3.15 m from the diaphragm, in which a cantilever could be mounted and the deformations could be visualized and recorded by high-speed photography. This position in the shock tube was chosen to minimize any effects of both instabilities in the shock wave due to the non-planar rupturing of the diaphragm, and of reflections from the open end of the shock tube.

The shock velocity was controlled by varying the pressure in the compression section and was measured by two piezo-electric pressure transducers (PCB model 113A21) mounted 0.2 m apart on the ceiling of the shock tube. The outputs from the transducers were amplified (PCB model 494A) and used to start and stop an interval timer (HP model 5302A) in order to obtain the transit time. The Mach number of the incident shock was calculated by

$$M = \frac{V}{\sqrt{\gamma R T_o}}, \tag{2.9}$$

where T_o is the temperature of the laboratory in Kelvin and V was the shock velocity.

2.4 Blast waves

2.4.1 Explosions

An explosion is the sudden release of energy from a centered source which produces a rapid expansion of material. For chemical explosions such as TNT the solid form of the explosive takes up much less volume than the gaseous products of the explosion. This gas expands rapidly and compresses the surrounding air to produce a blast wave. There are many other means of depositing energy at a specific point or volume of space. The rupture of a container of a compressed gas, the release of electrical energy in a spark gap or wire, and the muzzle blast from a gun are all energy sources that can be classified as explosions. An example of a "point" source

deposition of energy is the initiation of a nuclear reaction within a super critical sample of fusionable or fissionable material.

Two high explosive detonations of ANFO(ammonium-nitrate/fuel-oil) at White Sands Missile Range, New Mexico were used to study the response of a number of cantilever structures. The first explosive event, code named DISTANT IMAGE, consisted of 2,650 tons of ANFO and was detonated on 20 June 1991. The second, code named MINOR UNCLE was 2,431 tons and was detonated on 10 June 1993. Both were hemispherical surface burst charges to approximately simulate the blast environment that would be produced by a 4.0 kt nuclear detonation.

2.4.2 Ideal blast waves

Consider a pressure transducer, mounted with its sensitive surface side-on to the flow, located at some distance from a centered explosion in a homogenous atmosphere. If it can follow the variations of pressure perfectly the output would look like that shown if figure 2.1. Initially the the pressure is at the ambient pressure P_o until at the arrival time t_a the pressure increases abruptly to a peak value of P_s. The pressure returns to the ambient value at a time $t_a + t^+$ (t^+ is the positive phase duration). The pressure continues to drop below the ambient value and eventually returns at a time $t_a + t^+ + t^-$ (t^- is the negative phase duration). The negative phase may contain weak secondary and tertiary shocks produced by the deceleration and rebound of the detonation products.

The positive and negative impulses are defined by

$$I_s^+ = \int_{t_a}^{t_a+t^+} [p(t) - p_o]dt \tag{2.10}$$

and

$$I_s^- = \int_{t_a+t^+}^{t_a+t^++t^-} [p(t) - p_o]dt \tag{2.11}$$

respectively and are important blast wave properties when considering the blast loading on structures.

It is useful in some instances to have a functional form for the pressure-time relationship to describe measured time histories. The modified Friedlander equation is the most common formulation and is used to describe the positive phase which is generally the most damaging section of the blast wave. This equation is

$$p(t) = p_o + P_s(1 - t/t^+)e^{-bt/t^+}, \tag{2.12}$$

where P_s is the peak pressure and b is the decay constant. Non-linear least square fits of measured pressures to this equation can be made by iterating on P_s, t^+, and b.

All the physical properties of a blast wave, such as hydrostatic, dynamic and total pressure, density, temperature, and particle velocity may be described by a Friedlander type function although the decay constant and positive phase duration will in general be different for each property. Some properties, e.g. temperature and density, do not return to the ambient values after the passage of the blast wave. The variation of some of the properties may also have sudden discontinuities associated with a contact surface or region such as that between the air and the detonation products of an explosion. These contact regions may be large and unstable. Blast waves may also pick up dust and debris, which will significantly affect the loading experienced by a structure exposed to the blast.

2.4.3 Blast wave scaling

An important feature of blast waves is their scalability. Blast waves that are produced by two explosives of similar geometry but of different masses will produce similar blast waves at identical scaled distances and times if detonated in the same atmosphere. This law was first formulated by Hopkinson (1915) and is referred to as the "cube-root" scaling law.

If the shock front of a blast wave has a Mach number M at a distance R_{sc} from a centered explosion with an energy release E_{sc} then the same shock Mach number will be observed at a distance R from an energy release E, such that

$$\frac{R}{R_{sc}} = \left(\frac{E}{E_{sc}}\right)^{1/3} = \left(\frac{W}{W_{sc}}\right)^{1/3} \tag{2.13}$$

where, in the case of a chemical explosion W is the charge mass, assumed proportional to the energy yield. If W_{sc} is chosen as a unit mass(e.g. 1 kg or 1 kt), then

$$\frac{R}{R_{sc}} = W^{1/3} \Longrightarrow R_{sc} = \frac{R}{W^{1/3}}. \tag{2.14}$$

Times, such as t_a, the time of arrival of the shock front, or t^+, the positive phase can be scaled in the same manner,

$$t_{sc} = \frac{t}{W^{1/3}} \tag{2.15}$$

where t is the time.

The integral over the positive phase duration of any physical property of a blast wave such as the hydrostatic overpressure, will also scale as the cube root of the charge mass

$$I_{sc} = \frac{I}{W^{1/3}}, \tag{2.16}$$

where I is the impulse. The distances at which a scaled impulse or scaled time will occur are themselves scaled according to the cube root law.

If the atmospheric conditions are significantly different from the reference atmospheric conditions a correction should be made. The corrections to 2.14, 2.15, and 2.16 are given below and are obtained from Glasstone et al (1977),

$$R_{sc} = \frac{R}{W^{1/3}} \left(\frac{P}{P_o}\right)^{1/3}, \tag{2.17}$$

$$t_{sc} = \frac{t}{W^{1/3}} \left(\frac{P}{P_o}\right)^{1/3} \left(\frac{T}{T_o}\right)^{1/2}, \tag{2.18}$$

and

$$I_{sc} = \frac{I}{W^{1/3}} \left(\frac{P_o}{P}\right)^{2/3} \left(\frac{T}{T_o}\right)^{1/2}, \tag{2.19}$$

where T_o and P_o are the ambient conditions of the reference charge and T and P are the atmospheric conditions for the charge of interest.

These scaling laws have been tested for charges ranging from less than a gram to thousands of tons with excellent agreement.

2.4.4 Pressure definitions

There are essentially four types of pressure considered in the study of blast waves. The hydrostatic pressure is the pressure associated with a side-on measurement and therefore sometimes called side-on pressure. This is the simplest blast wave property to measure, and the peak value at the shock front is frequently used to define the strength of the blast wave.

Dynamic pressure is the pressure associated with the motion of the fluid and is defined as

$$P_d = \frac{1}{2}\rho u^2, \tag{2.20}$$

where ρ is the fluid density and u is the fluid velocity. The dynamic pressure is extremely high near the explosion but rapidly decreases with distance since it is a function of the square of the particle velocity.

Reflected pressure is the pressure associated with the reflection of the shock front from a surface and in the case of a normal reflection the pressure is a factor two or more greater the the incident hydrostatic pressure. This is accomplished by converting the energy associated with the dynamic pressure into hydrostatic pressure since at

the reflecting surface the boundary condition requires the flow velocity perpendicular to the surface to be zero.

Total or stagnation pressure is the pressure measured by positioning a measuring device or transducer head on to the oncoming flow. The gauge is therefore essentially measuring the sum of the hydrostatic pressure and the dynamic pressure with a compressibility factor that depends on the local Mach number of the flow.

It is often useful to know the difference between the hydrostatic pressure and the ambient pressure and this is called the overpressure. It is also sometimes convenient to have this as a ratio with respect to the ambient pressure, and is called the overpressure ratio.

Figure 2.4 shows the way in which the hydrostatic, total and dynamic pressures varied with distance from the surface burst explosion DISTANT IMAGE, obtained from a commercially available code called *AirBlast* which will be discussed in chapter 3.

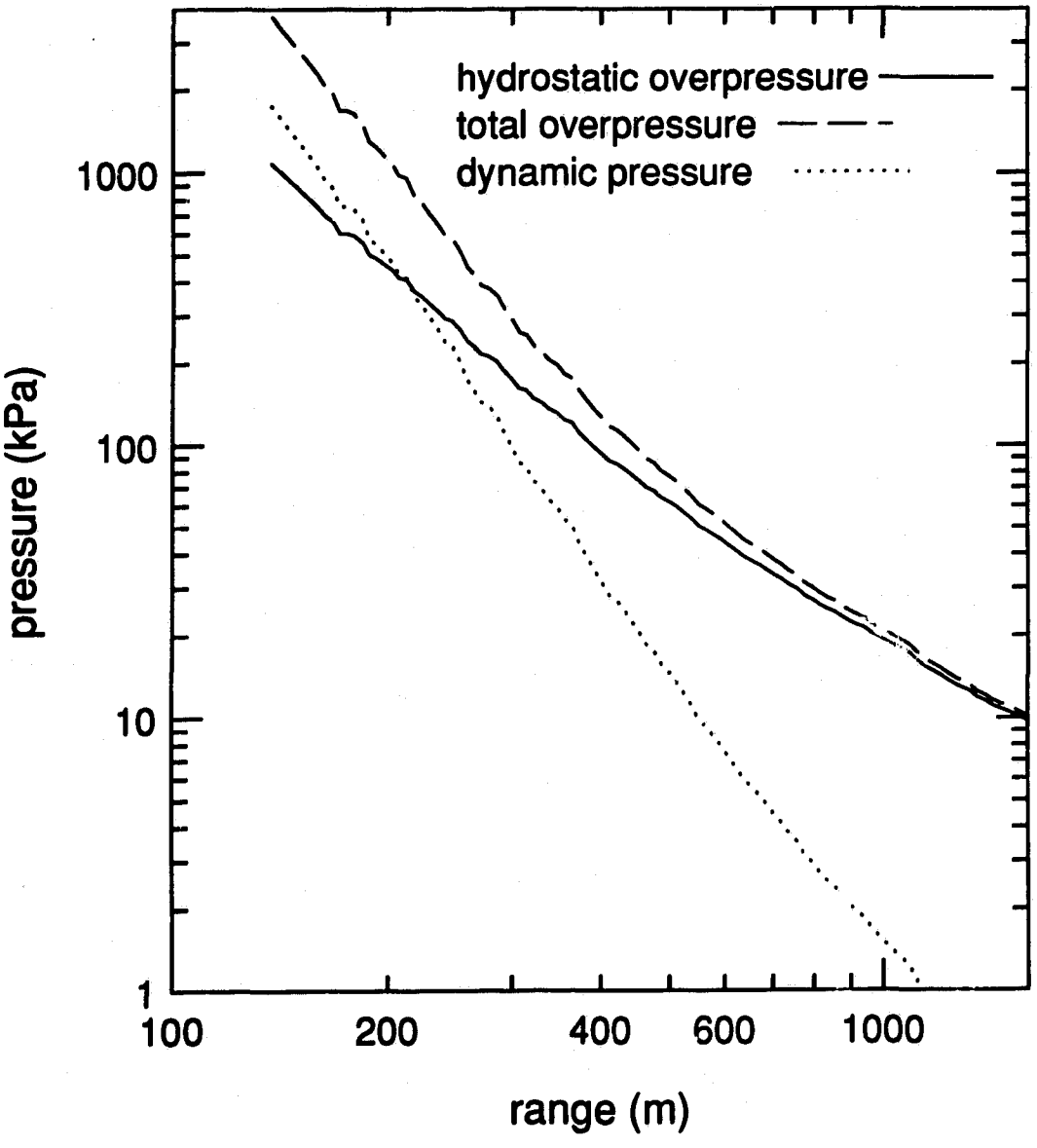

Figure 2.4: Variation of blast wave properties for the DISTANT IMAGE experiment.

Chapter 3

Cantilever modeling

3.1 Introduction

A cantilever can be described as a structure that is clamped at one end and free to move on the other end. The cantilevers described in this work were circular in cross-section and were assumed to have failure modes that were either brittle or ductile. All breaking or plastic bending was assumed to occur at or near the clamped end since it was observed that after being loaded the ductile cantilevers were straight throughout the entire length except at the clamped end where they bent through an angle α. For these cantilevers the critical parameter was the angle of deformation at the base.

3.2 Dynamic blast loads

The blast wave generated in an explosion imposes a dynamic load on any structure in its path. A static load is defined as one that is applied slowly so that the momentum of the structure itself is not a factor and the structure is allowed to shape itself until equilibrium is established between the loading forces and the internal stresses. Dynamic loads are applied rapidly so that the momentum and inertia of the structure are important, and imbalances between the loading forces and the internal forces induce vibrations in the structure.

The net load depends on the physical properties of the blast wave and the shape

and dimensions of the object. For structures such as cantilevers there are two types of possible loading, diffraction loading and drag-type loading. The interaction of the shock front with a cylindrical object is illustrated in figure 3.1. Initially as the shock wave passes over the structure it reflects as a regular reflection off the leading-edge surface and produces a high pressure on the front surface. The back surface has yet not felt the effect of the shock wave and is still at the ambient pressure conditions. The pressure difference on the two sides of the object produces a net force which accelerates the object. As the shock front propagates towards the back of the cylinder it undergoes a transition from regular reflection to Mach reflection when the angle between the incident shock and surface of the cylinder becomes greater than a certain critical value. Mach reflection is characterized by the development of a third shock wave called the Mach stem, as shown by the configuration in figure 3.1 (b). The pressure on the back side of the cylinder is increased with the arrival of the Mach stem thus reducing the net force on the cylinder. Eventually the Mach stems from the two sides of the cylinder interact and momentarily produce a small region of high pressure on the back of the cylinder. This is essentially the end of the diffraction phase and the loading force on the cylinder is now generated by the difference between the stagnation pressure on the front surface and the drag pressure on the back. This force is generally represented by a factor called the drag coefficient(C_d) multiplied by the dynamic pressure($\frac{1}{2}\rho u^2$) and the frontal area.

Both diffraction and drag-phase loading occur on any object in a blast wave flow, but in most cases one is more dominant than the other. The relative contribution made by each type of loading is determined by the size of the object and the duration of the blast wave. If the positive phase duration of the blast wave is of similar order of magnitude to the transit time for the blast wave to engulf the object then the loading is considered diffraction dominant however if the structure is small and hence this transit time is small compared to the positive phase duration then the loading is considered to be drag-type loading. The following paragraph describes a calculation

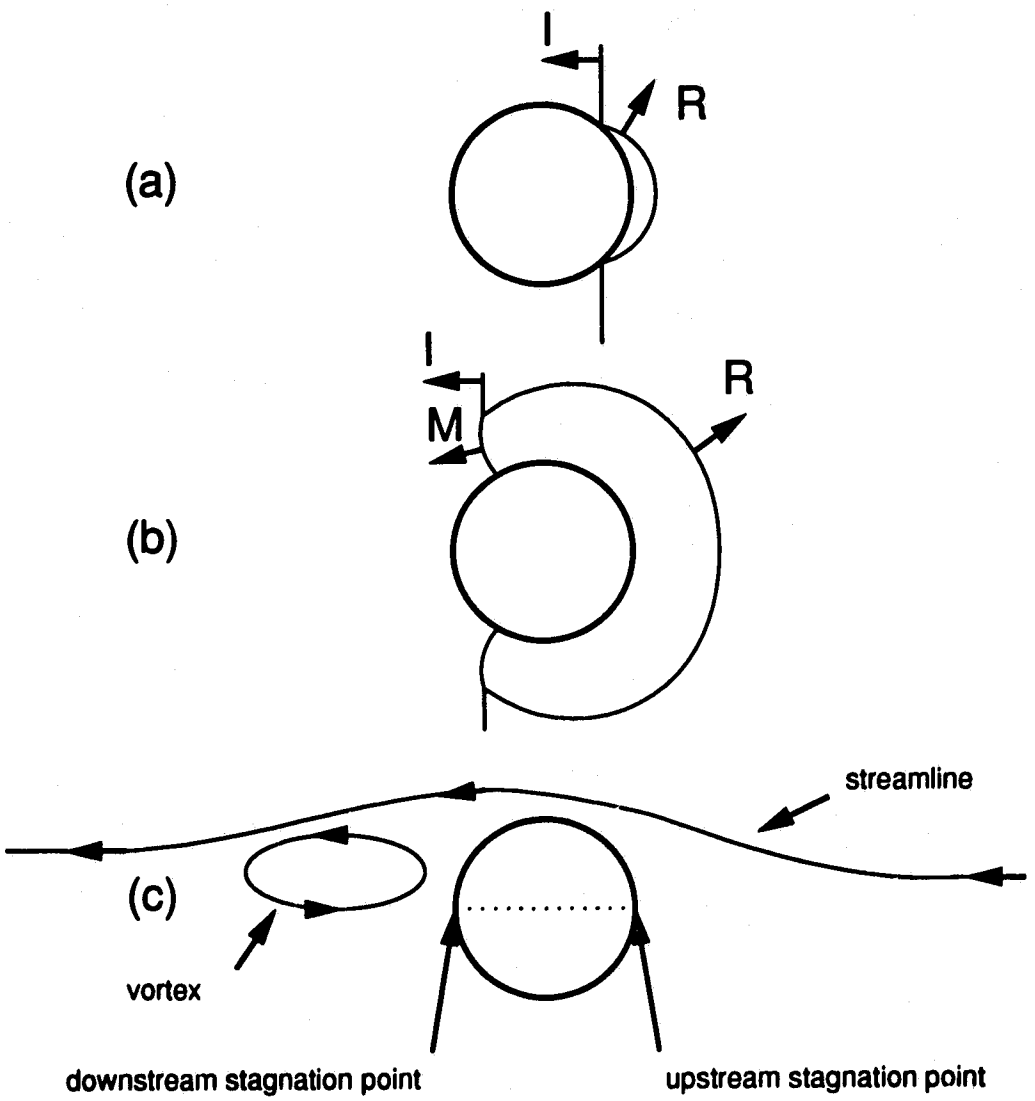

Figure 3.1: Interaction of a shock front with a cylinder. Diffraction phase: (a) regular reflection, (b) Mach reflection. Drag loading phase: (c) pseudo-steady flow. I is the incident shock, R is the reflected shock and M is the Mach stem shock.

which was done to estimate the relative contribution that each type of loading might have on a typical cantilever subjected to a shock tube flow.

The cantilever was assumed to have a length of 0.2 m and a diameter of 1.55 mm. The hypothetical loading on this particular cantilever was generated by a shock tube flow with an incident shock Mach number equal to 1.4, a profile similar to that shown in figure 2.2, and a positive phase duration of 14.4 ms. To approximate the calculation and make it a worst case scenario it was assumed that the shock wave reflected normally from the front surface and that the pressure at this position was equal to that produced by a shock wave reflecting normally from a flat surface. An incident shock Mach number of 1.4 produces a reflected pressure ratio of approximately 4.2 under these conditions. If the pressure on the back surface is equal to one atmosphere then the pressure difference will produce a force on the cantilever during the diffraction phase. In general, as the shock wave propagates around the cantilever expansion waves are produced which reduce the pressure on the front surface. As the shock front reaches the back surface the pressure there will increase and these two effects reduce the force on the cantilever during the diffraction phase. For this calculation however it was assumed that the pressure difference between the front and back surface remains constant throughout the diffraction phase to stay in accordance with the worst case scenario. Kinney et al, (1962) states that diffraction phase lasts for a time that is equal to approximately twice the time it takes for the shock wave to propagate the diameter of the cantilever. This corresponds to a time of 6.4 μs. Using this criterion and the dimensions of the cantilever, the impulse imparted to the cantilever during the diffraction phase would be approximately 6.4 $\times 10^{-4}$ N s. The impulse generated by the dynamic pressure during the drag loading phase, assuming a drag coefficient of 1.2, would be equal to about 0.10 N s. The relative contribution of the impulse during the diffraction phase to the total impulse imparted to the cantilever is therefore about 0.6 %. This value is a overestimate of the relative contribution and it will therefore be assumed that in the remainder of

this project that the cantilevers are loaded only by the drag forces and the shock wave diffraction effects can be ignored. It must be noted however, that although the imparted impulse during the diffraction phase is significantly less than that of the drag loading phase the magnitude of the force is approximately 10.0 times that during the drag phase. It is because the transit time of the cantilever is so small that its effects can be assumed negligible, but for larger objects or shorter duration flows this will not be the case.

The damage produced by a blast wave depends on the force that the flow exerts on a structure, on the length of time this force is applied and on the ability of the structure to withstand this force. Some drag loaded targets do not deform appreciably during the passage of the shock but absorb its energy. These type of structures are impulse sensitive and the damage to these structures can be considered to be purely a function of impulse of the blast wave (Ethridge, 1992). If impulse sensitive structures were to be employed as gauges to measure blast wave impulses the amount of damage would have to be calibrated against impulse. Using this calibration and the experimentally measured damage, a value for the dynamic pressure impulse at the point of measurement can be determined. For objects, such as cantilevers or buildings, the critical time within which the impulse must be received to inflict damage, so that the structure can be considered as impulse sensitive, is estimated to be about one quarter of its natural period of vibration (Kinney,1962).

Objects with a critical time which is much less than the duration of the blast wave will generally fail in the early stages of the blast loading. These gauges are primarily sensitive to the peak pressure and not the impulse. In general objects are sensitive to both peak pressure and a partial impulse. This can be more clearly seen by plotting a pressure-impulse (P-I) diagram of damage for a given structure. Such a diagram defines the target's susceptibility to airblast and an example is shown in figure 3.2. The rectangular hyperbola shaped curve defines a threshold of damage and can be considered as an isodamage curve. This curve defines those values of

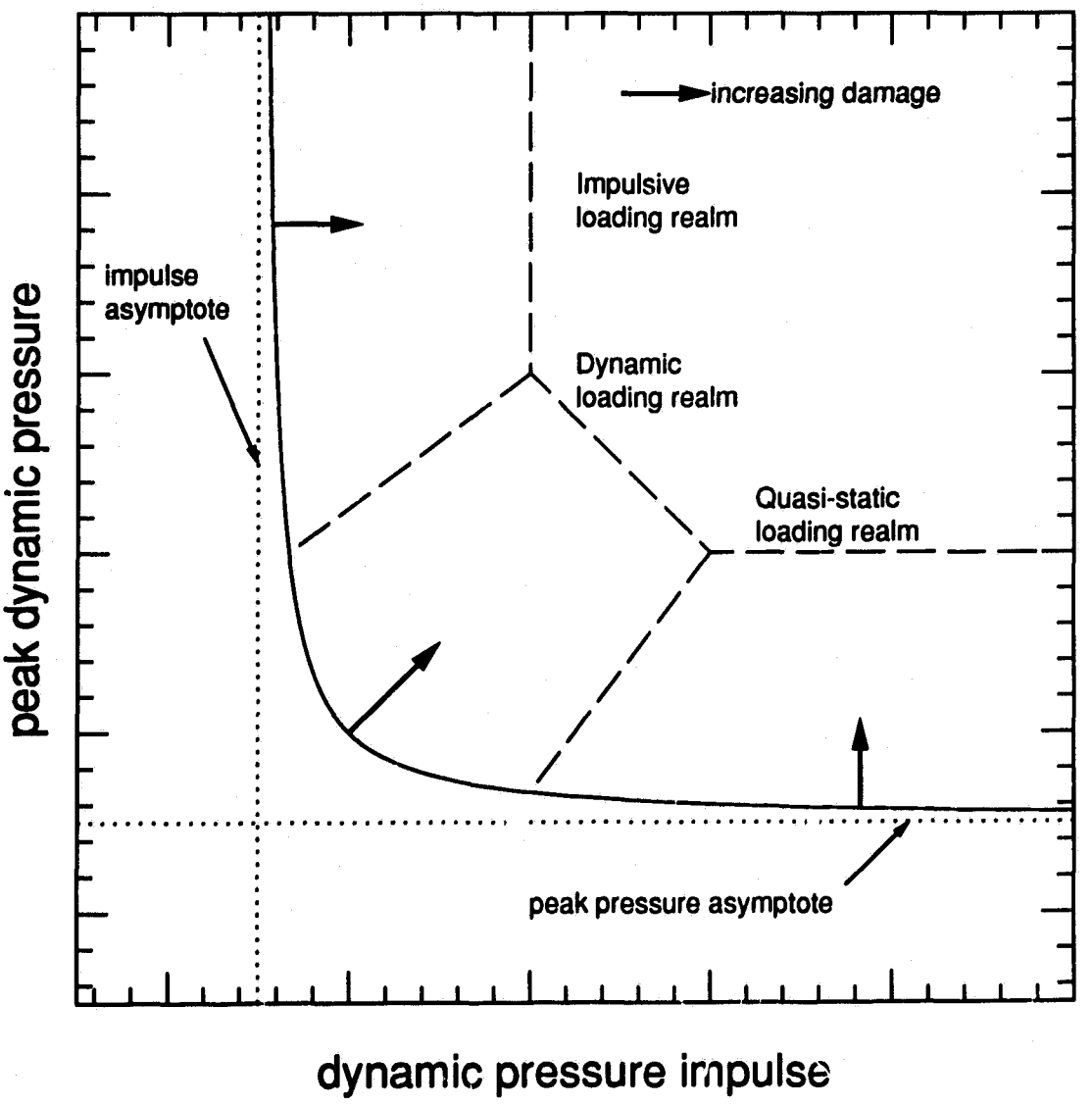

Figure 3.2: A pressure-impulse diagram for a structure subjected to a blast load. The solid line is an isodamage curve, such that if the pressure-impulse combination lies below the curve, less damage is expected, and if above the curve more damage is expected.

impulse and peak pressure at which a specified type of damage occurs. For example, in the case of a ductile cantilever the angle of deformation would be considered a value of specified damage. For that degree of bending to be produced by the blast wave from a small explosive charge, the cantilever would need to be relatively close to the charge where the peak pressure was large. The same degree of bending could be achieved with a larger charge at a distance where the peak pressure was less but the impulse larger. The P-I curve is the locus of all those values at which the specified angle of bending would occur. If the point defined by the peak pressure and impulse of the blast wave lie above and to the right of a specific curve the damage will be greater than that specified by the curve. If it lies lower and to the left, the damage will be less than that specified. This type of plot also shows the conditions that the blast wave must have for the structure to be impulse sensitive or peak pressure sensitive. Each arm of the hyperbola converges to an asymptote. The horizontal asymptote is the peak pressure for infinitely large impulses, namely the minimum dynamic pressure required to produce the damage. The vertical asymptote is the minimum impulse needed to produce the damage, even with extremely large peak pressures.

The P-I diagram for a specific final angle of bend for a specific cantilever subjected to blast loading could theoretically be created by performing many experiments using a wide range of charge sizes. Such an experimental approach is clearly not feasible due to the large number of experiments that would be needed, the alternative is to numerically model the deformation of cantilevers under blast loading, and use the results to generate the P-I diagrams. A numerical model will also provide information on the dynamics of the deformation process.

3.3 Loading function

For the response of a cantilever to be theoretically calculated a knowledge of the loading function is required. The loading function depends on the time history of

the dynamic pressure in a shock or blast wave, and on the drag coefficient which may itself be a function of the Mach number and/or the Reynolds number of the flow. To describe the loading function on cantilevers placed in a shock tube flow an inviscid one dimensional explicit Flux corrected transport(FCT) simulation was written. For the large scale explosions the flow properties were obtained from two programs, *AirBlast* (Dewey and McMillin, 1989) and ANFO.EXE (Needham *et al*, 1991). *AirBlast* is a database of experimentally-measured results, while ANFO.EXE is based on a pure hydrodynamic code.

3.3.1 Shock tube simulation

The shock tube produces a flow in which the hydrodynamic flow properties vary in only one coordinate direction. To obtain the solution to this problem the conservation laws of mass, momentum and energy are solved. The set of equations are called the Euler equations and are given below in their one dimensional form:

$$\text{mass} \qquad \frac{\partial \rho}{\partial t} + \frac{\partial(\rho u)}{\partial x} = 0, \tag{3.1}$$

$$\text{momentum} \qquad \frac{\partial(\rho u)}{\partial t} + \frac{\partial(p + \rho u^2)}{\partial x} = 0, \text{ and} \tag{3.2}$$

$$\text{energy} \qquad \frac{\partial e}{\partial t} + \frac{\partial(u(e+p))}{\partial x} = 0, \tag{3.3}$$

where ρ is the density, t the time, u the velocity in the x direction, p the pressure, and e is the sum of the internal and kinetic energies per unit volume. The value for e is given by

$$e = \frac{p}{\gamma - 1} + \frac{1}{2}\rho u^2, \tag{3.4}$$

where γ is the ratio of specific heats and for air, equal to 1.4. For shock waves up to moderate strengths(M less than $\approx$ 3) the ideal gas equation of state may be used

viz.

$$p = \rho RT, \tag{3.5}$$

where R, the gas constant for air, is 287 J/(kg K) and T is the temperature of the gas in Kelvin.

There are some solutions to this set of conservation equations for certain boundary and initial conditions but a general analytical solution does not exist and hence they must be solved numerically. A finite difference scheme using an explicit flux corrected two step Lax-Wendroff technique was chosen to solve these equations. A thorough description of the flux corrected transport(FCT) algorithm is given by Book and Boris (1975). Basically, the FCT technique is a procedure specifically designed to propagate steep gradients such as shocks without smearing them over many grid points. The conventional Eulerian methods when treating such situations introduce large numerical diffusion to damp out the numerical instabilities. This has a tendency to disperse any areas with large gradients and it does not distinguish between the gradients caused by numerical ripples and shocks. The FCT algorithm is based on a corrective diffusion scheme and localizes this diffusion in just those areas where the non-physical ripples tend to form. It carries out this diffusion in a conservative way so that what ever it takes away from one grid point it puts back somewhere else. The amount of diffusion can be adjusted but in most cases the diffusion factor is set to a value near 0.125. The algorithm is fully second order accurate in both time and space.

The University of Victoria's shock tube is 8.06 m long and for the numerical model was divided into 806 grid points so that the size of each grid element corresponded to one centimeter. The diaphragm was positioned between grid points 105 and 106. The boundary condition at the back wall of the compression chamber was set as reflective by using a set of mirror positions in the wall and assigning the momentum as the negative of the momentum outside the wall. The other end of the shock tube is open to the atmosphere and the boundary conditions at this position were set to

the same values as that in the expansion chamber, that is the atmospheric conditions for the day. The hydrodynamic values of the compression chamber were set to the required conditions to duplicate the experimental value of the Mach number for the particular experiment. This is important since if the experimental value for the pressure in the compression section was used as the input the Mach number produced by the numerical simulation would be higher than that found experimentally. This is due to dissipative effects such as non-ideal rupturing of the diaphragm etc.

Figure 3.3 shows a comparison of the various flow property distributions obtained by the numerical calculation and that calculated analytically for the shock tube with the following initial conditions. The gas temperature in both sections was 300 K, the pressure ratio across the diaphragm was set at 4.96 and the expansion pressure was at one atmosphere. These initial conditions produce a shock of Mach number 1.4. The shock wave in these plots is at a shock tube position of 206 cm. As can be seen the agreement is excellent; the incident shock is confined to 2 zones, and there is very little numerical noise.

The analytic solution was not used to provide the data for the loading of the cantilevers since this solution can only be made up to the time until the rearward traveling expansion wave strikes the back wall of the compression chamber.

Figure 3.4 gives a comparison between the experimental measurements of a particle trajectory and that simulated by the numerical model. The initial position of the particle was 3.28 m from the diaphragm and was struck by a shock wave of Mach number 1.375. The experimental trajectory was obtained from the calibration of the shock tube performed by Whitten (1969) using "massless" smoke particles. The match is excellent up to a particle displacement of about 1.6 m after which the experimental displacement of the particle exceeds the numerical values. The important region in these curves for the loading of the cantilevers is the first part where the velocity is highest. The difference in the upper part of the curve can be most likely attributed to the delay of the arrival of the rarefaction wave. The rarefaction wave

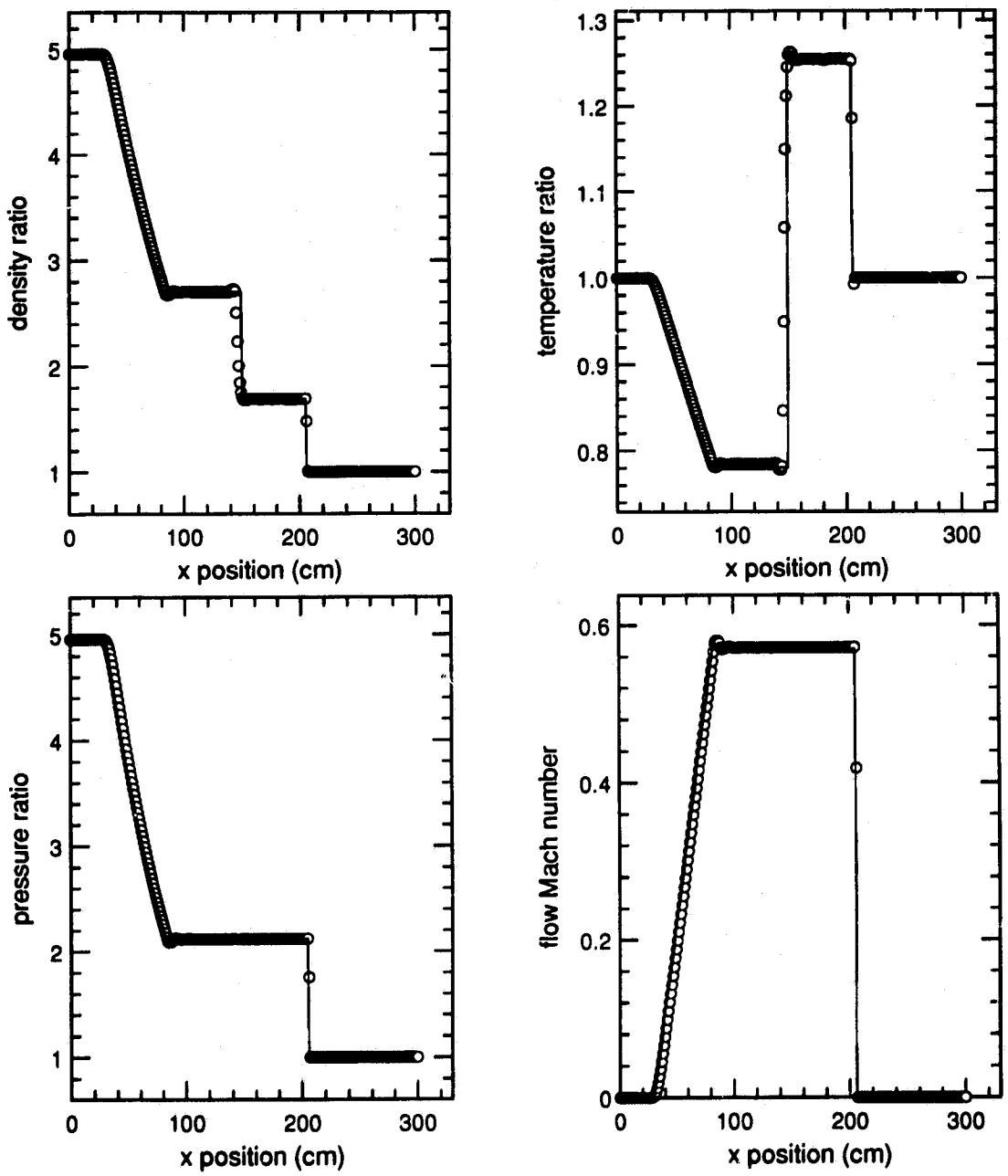

Figure 3.3: Comparison of the various flow properties, as ratios with the ambient values, simulated by the FCT shock tube simulation(circles) and the analytic solution(solid), as a function of the distance along the shock tube at a fixed time. Diaphragm position at x= 106 cm.

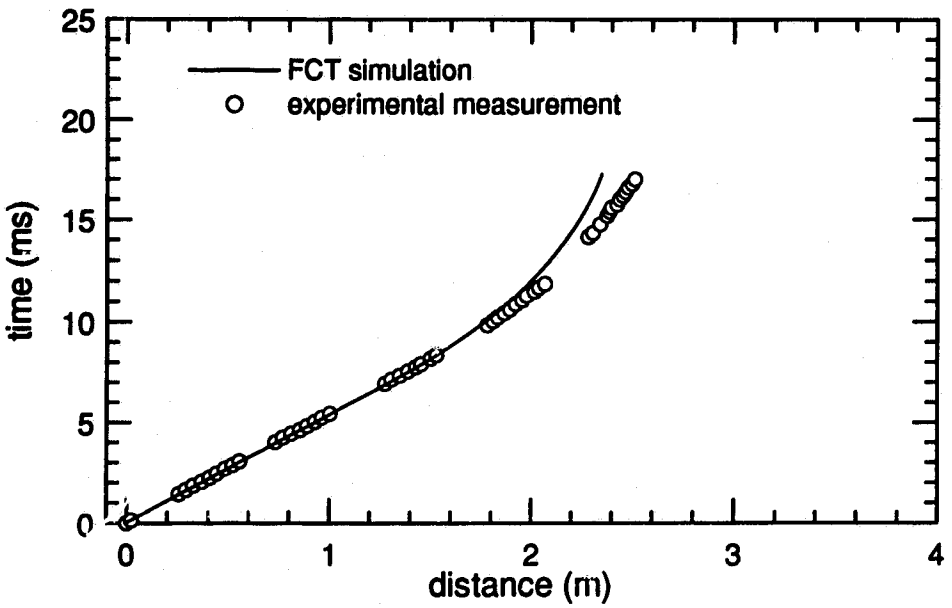

Figure 3.4: Comparison between the observed particle displacement measured within the shock tube by Whitten (1969) and that simulated by the FCT numerical model. The particle started 3.28 meters from the diaphragm and was hit by a shock wave of Mach number 1.375.

propagates at the speed of the air particles plus the local speed of sound and because of various effects such as the growth of the boundary layer, non-ideal reflection of the rarefaction wave from the back wall and diaphragm material in the contact surface region, the rarefaction wave propagates at a somewhat slower velocity. This causes the attenuation of the flow properties behind the shock to occur somewhat later in the real shock tube.

For all the shock tube experiments the cantilevers were positioned 3.15 m from the diaphragm which corresponded to grid point number 420. As the FCT model executed it produced a data file which contained the required values to calculate the dynamic pressure as well as the temperature time histories at grid point 420. These values were subsequently read in by the numerical deformation program which used this information to calculate the simulated drag loading for the cantilever.

3.3.2 Airblast simulation

Two programs were used to provide the required dynamic pressure and temperature time histories for the experiments involving the large scale field experiments.

AirBlast is a commercially available program which provides accurate data for any specified explosion and initial conditions. The *AirBlast* program uses a database created by a numerical simulation which is forced to reproduce a large number of experimentally measured data. This simulation provides the blast wave properties to fill the gaps in the regions between experimental measurements. The *AirBlast* program scales this database in accordance with a specified charge mass and set of atmospheric conditions, and uses the results with the ideal gas equation of state to provide all the blast wave flow properties at a defined distance from an explosive event. The strength of this program is that it provides data known to agree exactly with experimentally measured quantities, principally time resolved particle trajectories measured by high speed photography of flow tracers and pressure time histories obtained from piezoelectric transducers. One drawback of this program, however, is that, up to now, it is not valid in regions where real gas effects are significant or where detonation products may be present. This generally occurs where hydrostatic overpressures are greater than approximately 690 kPa (100 psi or 6.8 atm).

The second numerical program, called ANFO.EXE produces a database generated entirely by a hydrodynamic code. Real gas effects are included as well as the chemical dynamics of the explosion itself. The database is generated only for the detonation of a hemispherical surface burst charge of ammonium nitrate fuel oil mixture(ANFO). However by appiying appropriate scaling factors it can be used to approximate other explosive mixtures. This program was used when data were required in regions where real gas effects played a role, namely close to the explosive charge.

A comparison of peak dynamic pressure versus range between these programs and that measured experimentally is given in figure 5.26. The agreement is excellent and it is therefore assumed that these programs provide realistic data for the loading

functions.

3.3.3 Drag coefficients

It was assumed that the loading on the cantilevers considered in this project was directly related to the dynamic pressure in the flow field. The equation relating the dynamic drag force,F_d, on a cantilever to the dynamic pressure is

$$F_d = C_{d(\alpha,R_e,M)}\frac{1}{2}\rho u^2 A, \tag{3.6}$$

where $C_{d(\alpha,R_e,M)}$ is the drag coefficient and A the frontal area exposed to the flow. The C_d of a circular cross-section cantilever is a function of the angle of orientation to the flow(α), the Reynolds number(R_e) and the local Mach number(M) of the flow.

The Reynolds number is the dimensionless ratio of the inertial and the viscous forces of the flow and is an important parameter in relating dynamically similar flows. The Reynolds number is defined as

$$R_e = \frac{ud}{\nu},$$

where u is the free-stream flow speed, d is a representative dimension of the structure, in this case the diameter of the cantilever, and ν is the kinematic viscosity. The local Mach number is defined as the ratio of the velocity of the air particles to the local speed of sound at the given position and time. The loading of constrained structures by blast waves is an unsteady event and, since both the Reynolds and Mach numbers are functions of the time varying flow conditions, the drag coefficient is also time varying.

There has been some limited work to determine the drag coefficients of cylinders in flows which are unsteady, including Kim et al (1971_b), Martin et al (1967) and Mellsen et al (1969). Kim et al (1971_a) and also Mellsen (1971) both experimented with cylindrical structures in blast waves and their results indicated that there were

some differences between the unsteady and steady drag coefficients however these were small and hence the steady results could be used as a good approximation.

The drag coefficient vs Reynolds number for steady flow is shown in figure 3.5 and versus Mach number in figure 3.6. These data were obtained from Schlicting (1960) and Hoerner (1965) respectively. The region of interest for the Reynolds number is approximately between R_e of 1.0×10^4 and 1.0×10^6. In this region there is a dramatic decrease in the drag coefficient from about 1.2 to 0.3 at about $R_e = 4.0 \times 10^5$. The Reynolds number at which this occurs is called the critical Reynolds number and it signifies the conditions when the boundary layer over the cylinder undergoes transition from laminar to turbulent.

Figure 3.6 shows the drag coefficient vs Mach number for both the laminar and turbulent boundary layer flows. At a Mach number of about 0.4, the critical Mach number, both curves above and below boundary layer transition coalesce and form a single curve. Under these conditions the drag coefficient is purely a function of Mach number. Above this critical Mach number the drag coefficient increases from about 0.3 to 2.2 at a Mach number of just under 1.0. With a further increase in Mach number the drag coefficient decreases to a constant value of about 1.2.

The data from these curves was digitized and stored in a file which is subsequently read during the numerical simulation of the blast loaded response of the cantilever. The drag coefficient is determined by calculating both the Reynolds and Mach numbers for the given conditions. The Reynolds number is used to identify if the flow is laminar or turbulent. If the result is laminar the upper curve of figure 3.6 is used and if turbulent the lower curve is used.

The drag coefficient is also a function of the angle of inclination of the cantilever. The experimental results obtained from Hoerner (1965) for skewed cylinders in a steady flow show that the drag coefficient can be estimated by the following equation:

$$C_d = C_{d(\alpha=0)} cos^3(\alpha), \tag{3.7}$$

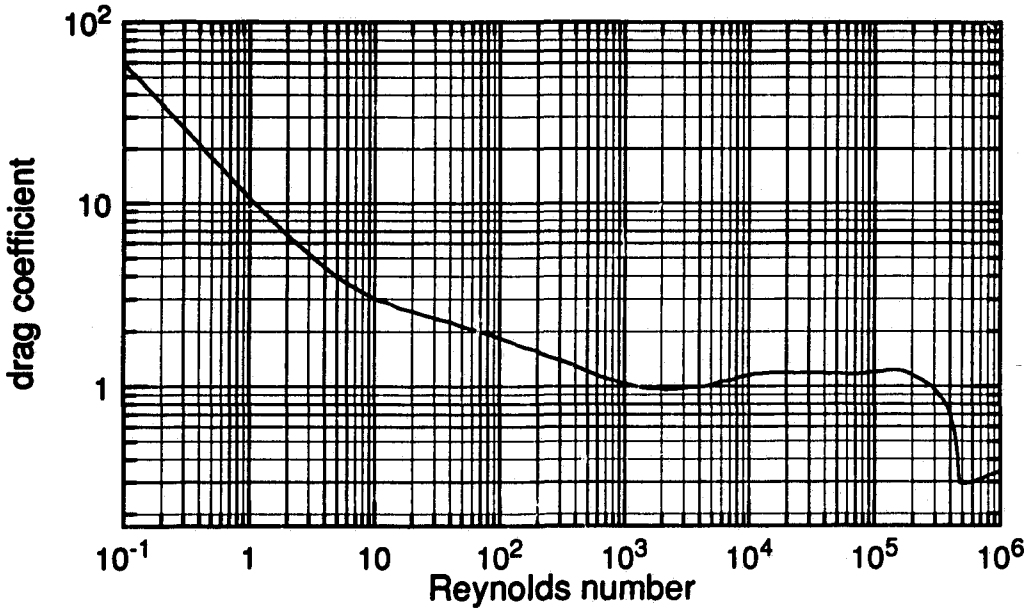

Figure 3.5: Drag coefficient for a circular cylinder as a function of Reynolds number (Schlicting, 1960).

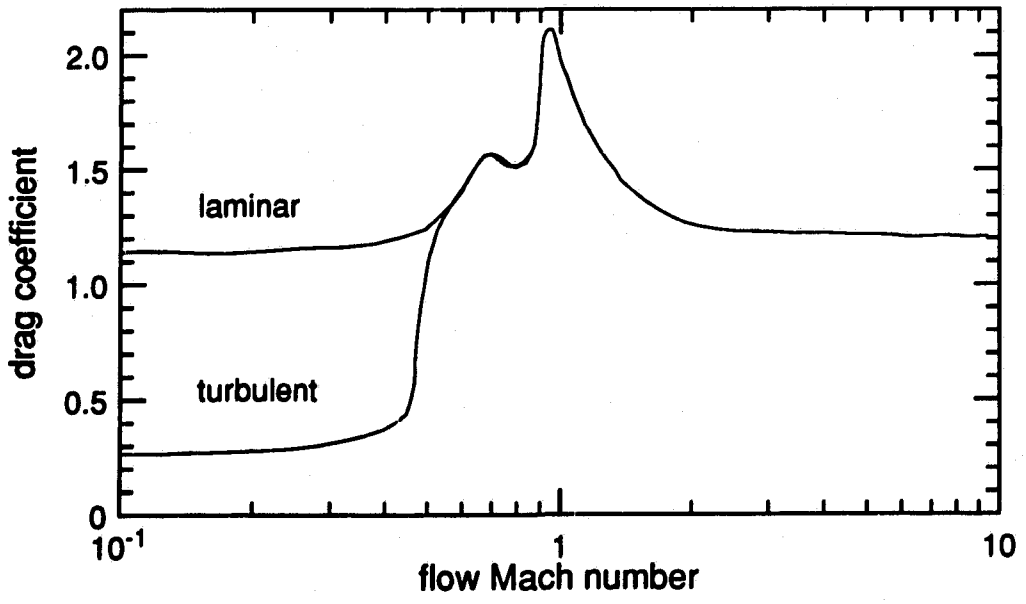

Figure 3.6: Drag coefficient for a circular cylinder as a function of Mach number (Hoerner, 1965).

where α is the angle through which the cantilever has deformed and $C_{d(\alpha=0)}$ is the drag coefficient for a zero angle of attack. A value for the drag coefficient was determined using the above criteria at every timestep during the calculation of the response of the blast loaded cantilever.

3.4 Cantilever response

3.4.1 Introduction

The purpose of this section is to present the various mathematical models and the underlying assumptions used to predict the response of the cantilevers in both the shock tube and HE tests. These predictions serve as a basis for deciding which cantilevers will be located at which positions. This is particularly useful for cantilevers made of materials not previously used at HE events. These models can also be used to provide information about the size and position of accidental explosions by reverse engineering the observed damage to cantilever type structures.

3.4.2 Ductile cantilevers:Rigid-plastic

The rigid-plastic model is the most elementary assumed response of a blast loaded cantilever. This response is based on the premise that the cantilever does not deform until the moment produced by the drag force about the clamped end exceeds the maximum resisting moment of the material. When this condition arises a plastic hinge is created close to the clamped end and the cantilever begins to rotate about this position as a rigid body until all the energy is dissipated in plasticity. The equation of motion is described below:

$$I\frac{d^2\alpha}{dt^2} = M_l - M_r, \tag{3.8}$$

where α is the angle through which the cantilever is bent, I is the moment of inertia of a rod rotating about its end($\frac{1}{3}mL^3$), m is the mass of the cantilever, L is the

length of the cantilever, M_l is the drag induced moment on the cantilever, and M_r is the maximum resisting moment that the material can produce. This equation shows that the angular acceleration of the cantilever is produced by the difference between the torque exerted by the flow(M_l) and the resisting moment(M_r) of the material.

M_l is the bending moment produced by the dynamic pressure of the flow and can be calculated by

$$M_l = \int_0^L q(t)xcos(\alpha)dx = \frac{1}{2}q(t)L^2cos(\alpha), \tag{3.9}$$

where $q(t)$ is the force per unit length on the cantilever, x is the distance from the fixed end and α is the angle of deformation of the cantilever. The value for $q(t)$ can be determined from the dynamic pressure and the drag coefficient, namely

$$q(t) = C_d\frac{1}{2}\rho u^2 A/L, \tag{3.10}$$

where A is the frontal area of the cantilever. $q(t)$ is a function of time since C_d, ρ and u are all time varying quantities.

The resisting moment of a cantilever with a circular cross-section of radius a is given by

$$M_r = 4\int_0^a \int_0^{\sqrt{a^2-x^2}} \sigma_y y dy dx, \tag{3.11}$$

where σ_y is the yielding stress of the material and x and y are the cross sectional area coordinates as shown in figure 3.7. If the material is assumed to be perfectly plastic throughout its entire cross section with a constant σ_y then σ_y can be taken out of the integral. Evaluating this integral and substituting $\frac{d}{2}$ for the radius a yields

$$M_r = \frac{4}{3}\sigma_y\left(\frac{d}{2}\right)^3. \tag{3.12}$$

Combining equations 3.8, 3.10, 3.9 and 3.12 provides the equation of motion of the

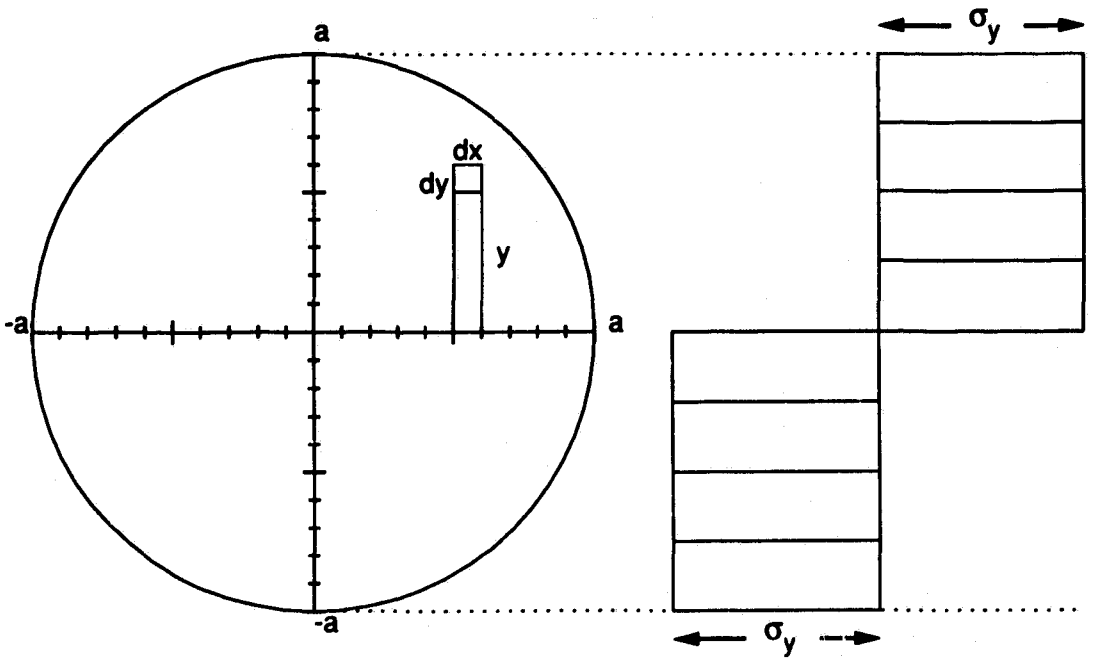

Figure 3.7: Cross-section of a circular cantilever of radius **a**. The right hand side shows the stress distribution within the material at the time of yielding.

cantilever:

$$\frac{d^2\alpha}{dt^2} = \frac{1}{I}\left[\frac{1}{4}\rho_a dL^2u^2C_d cos(\alpha) - \frac{4}{3}\sigma_y(d/2)^3\right]. \tag{3.13}$$

A fourth order Runga-Kutta scheme was used in conjunction with the required flow property data and the drag coefficient data to integrate this equation over a large number of timesteps and obtain the final angle of bend. This equation shows that the angular acceleration of the cantilever is produced by the difference between the imposed load and the strength of the material. If the material is strong enough to withstand the load, no motion will occur, but if the load is larger the cantilever will begin to accelerate and the rate of the acceleration is proportional to the moment of inertia of the cantilever. A graphical representation of the solution for a cantilever subjected to a shock tube flow is given in figure 3.8.

Although this model is limited by the assumptions, it provides a first order approximation to the response of the cantilever. A more realistic description of the

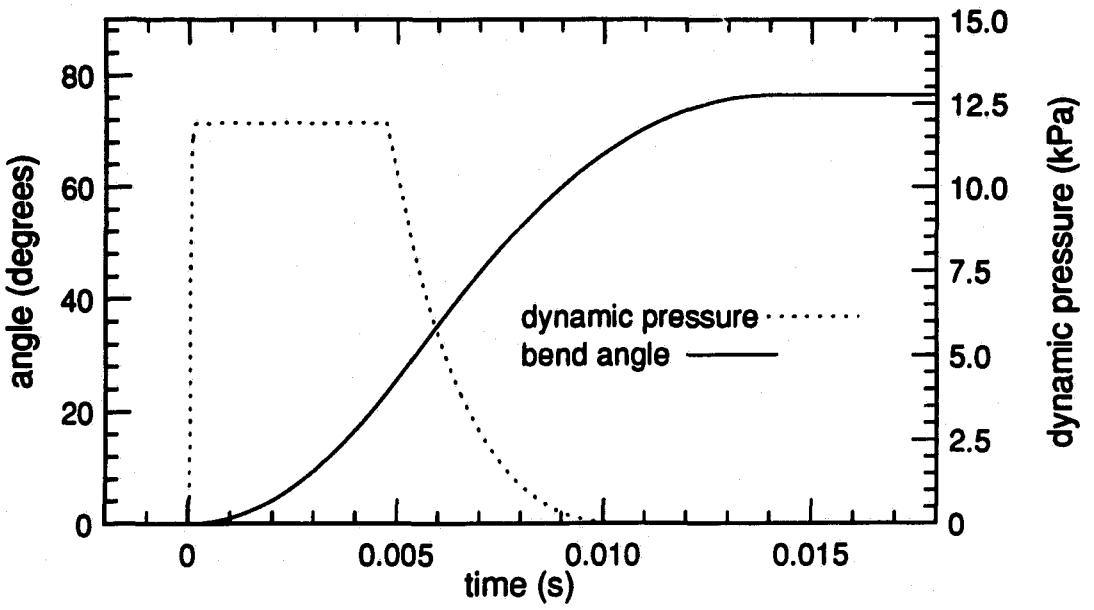

Figure 3.8: The deformation of a cantilever as a function of time based on equation 3.13 for a 0.05 cm long solder cantilever subjected to a shock tube flow produced by a M=1.23 incident shock wave.

response would include such effects as elasticity, strain hardening and strain-rate hardening in the equation of motion. Elasticity would produce a curvature in the rod, which for the longer cantilevers would be significant. This curvature reduces the torque exerted by exposing less area to the flow and it also shortens the lever arm. With this and the strain hardening effects the deformation angles produced by a elastic-plastic model should be less than that calculated by the rigid-plastic model. This was observed during this work and also in the work of others(Baker et al,1983). The following section describes the development of an elastic-plastic model with strain effects.

3.4.3 Ductile cantilevers:Elastic-plastic

A cantilever initially responds by deforming elastically until the deformation produces a bending moment which exceeds the maximum allowed by the material. This

occurs first in the outer fibres of the cantilever while the center remains elastic. At the position where this maximum occurs the cantilever permanently deforms while still undergoing its elastic deformation in other regions where the maximum has not yet been exceeded. For the cantilevers used here this maximum occurred at the base of the cantilever and therefore this is the only position where plasticity was considered in this elastic-plastic model.

As a cantilever is blast loaded it deforms elastically throughout until at some point the curvature of the rod exceeds the maximum allowed curvature. This maximum elastic curvature can be determined by the moment curvature relationship given below (Gere et al, 1984)

$$\frac{\frac{d^2y}{dx^2}}{\left[1+(\frac{dy}{dx})^2\right]^{3/2}} = \frac{M}{EI}, \tag{3.14}$$

where M is the maximum bending moment allowed within the rod, E is the Young's modulus, I is the area moment for the cross section of the rod($\pi d^4/64$ for a circular rod of diameter d), x is the distance measured from the clamped end and y is the displacement of the rod from the equilibrium position. The shape of the elastic deflection curve as obtained from this equation is called the elastica. At the clamped end or base of the cantilever the slope($\frac{dy}{dx}$) is equal to zero and the equation can be simplified to

$$\frac{d^2y}{dx^2} = \frac{M}{EI}. \tag{3.15}$$

The algorithm for this elastic-plastic model is based on the condition that the elastic curvature cannot exceed a maximum value and that this maximum is determined by 3.15 and the maximum allowed bending moment for the cantilever. If the curvature does exceed this value the material will deform in such a way as to keep the curvature constant and equal to the value determined by equation 3.15. When this occurs the material is assumed to become fully plastic throughout its

entire cross-section at the base while remaining elastic throughout the rest of the cantilever. The curvature is kept at the maximum allowed curvature by a plastic rotation of the cantilever about the clamped end of the required amount to keep the curvature equal to the maximum. A proof of the apparent reduction of curvature with a rotation of the cantilever about the clamped end is given below.

Assuming that the deflection of the deformed beam can be described by an arbitrary function $y = f(x)$ intersecting the origin, the curvature of the beam would equal $f''(x)$ by the application of 3.15. To obtain the curvature in a reference frame rotated about the origin by a angle θ, $f(x)$ must be first rotated. The rotated coordinates denoted as x_r and y_r, would equal

$$x_r = xcos(\theta) - f(x)sin(\theta), \tag{3.16}$$

and

$$y_r = xsin(\theta) + f(x)cos(\theta). \tag{3.17}$$

The slope in the rotated frame can be found by using the chain rule

$$\frac{\partial y_r}{\partial x_r} = \frac{\partial y_r}{\partial x}\frac{\partial x}{\partial x_r}. \tag{3.18}$$

The right hand side of 3.18 can be found by taking the partial derivatives with respect to x of 3.17 and 3.16

$$\frac{\partial y_r}{\partial x} = sin(\theta) + f'(x)cos(\theta). \tag{3.19}$$

and

$$\frac{\partial x_r}{\partial x} = cos(\theta) - f'(x)sin(\theta). \tag{3.20}$$

Substituting these into 3.18 yields the slope of the beam in the rotated reference frame and is given below,

$$\frac{\partial y_r}{\partial x_r} = V = \frac{sin(\theta) + f'(x)cos(\theta)}{cos(\theta) - f'(x)sin(\theta)}. \tag{3.21}$$

To obtain the curvature in the rotated reference frame, the second derivative of y_r with respect to x_r is needed(recall equation 3.15). This can be found by another application of the chain rule

$$\frac{\partial V}{\partial x_r} = \frac{\partial V}{\partial x}\frac{\partial x}{\partial x_r}. \tag{3.22}$$

The first partial derivative on the right hand side of 3.22 is

$$\frac{\partial V}{\partial x} = \frac{f''(x)cos(\theta)}{cos(\theta) - f'(x)sin(\theta)} + \frac{[sin(\theta) + f'(x)cos(\theta)]f''(x)sin(\theta)}{[cos(\theta) - f'(x)sin(\theta)]^2}. \tag{3.23}$$

Dividing 3.23 by 3.20 we obtain

$$\frac{\partial V}{\partial x_r} = \frac{f''(x)}{[cos(\theta) - f'(x)sin(\theta)]^2}\left[cos(\theta) + \frac{sin^2(\theta) + f'(x)cos(\theta)sin(\theta)}{cos(\theta) - f'(x)sin(\theta)}\right]. \tag{3.24}$$

This can be reduced to

$$\frac{\partial V}{\partial x_r} = \frac{f''(x)}{[cos(\theta) - f'(x)sin(\theta)]^3} = \frac{\partial^2 y_r}{\partial x_r^2}. \tag{3.25}$$

This equation gives the curvature of the beam in the rotated reference frame.

We wish to determine the angle θ at which equation 3.25 has a minimum. This can be found by taking the derivative of 3.25 with respect to θ and solving for the angle which makes the resulting function equal to 0, i.e.

$$\frac{d}{d\theta}\left[\frac{\partial^2 y_r}{\partial x_r^2}\right] = \frac{3f''(x)[sin(\theta) + f'(x)cos(\theta)]}{[cos(\theta) - f'(x)sin(\theta)]^4} = 0. \tag{3.26}$$

This can only be true if either $f''(x)$ or $sin(\theta) + f'(x)cos(\theta)$ is equal to zero. If $f''(x)$ is equal to zero implies that the beam has no change in slope, in otherwords it has no curvature. The condition where $sin(\theta) + f'(x)cos(\theta)$ equals zero implies that

$$f'(x) = -tan(\theta). \tag{3.27}$$

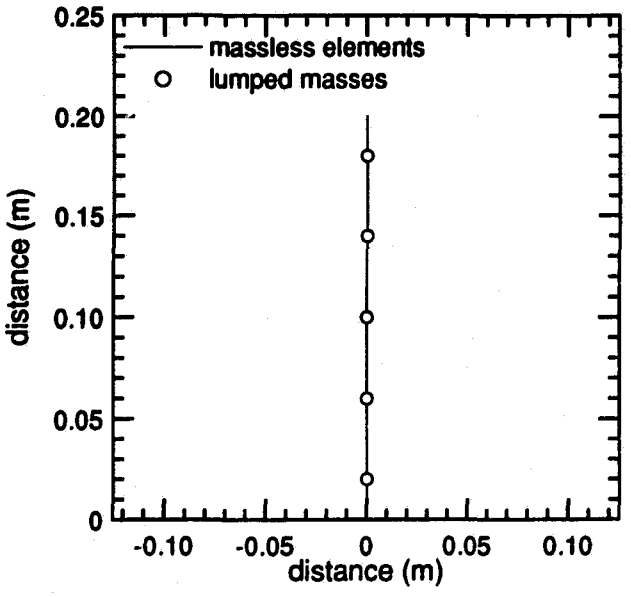

Figure 3.9: Discretization of a 0.2 m cantilever into five elements.

So if a function has a finite small slope at a point, say the origin, and it is rotated about that point by the angle which satisfies 3.27, the curvature will be a minimum in the rotated reference frame.

A multi-degree of freedom method was used to simulate the elastic response using an updated stiffness matrix at each timestep. This method assumes that a cantilever with a continuous mass distribution can be approximated by a finite set of lumped masses joined together by flexible, weightless structural members. The rod was considered to be made of n elements with equal lengths and masses. Figure 3.9 shows the distribution of masses for a cantilever which has been simulated with 5 elements. Under dynamic loading the motion of each one of these masses is different, however, due to continuity of the rod the motions of the masses interact with one another. If the rotary inertia of each element is neglected the equation of motion of the i^{th} element at a given time is determined by

$$m_i \frac{d^2 y_i}{dt^2} = F_{l_i} - F_{r_i}, \tag{3.28}$$

where $\frac{d^2 y_i}{dt^2}$ is the acceleration of the element, F_{l_i} is the dynamic force exerted on the element, m_i is the mass of the element and F_{r_i} is the resisting force of the element. The dynamic force on the i^{th} element is calculated by using an identical procedure as that used for the rigid-plastic cantilever but applied to each individual element.

The resisting force is not only a function of the displacement of the i^{th} element but also function of the displacements of the other elements. It is calculated by summing up all the forces caused by all elements. Each one of these forces can be arranged in a matrix called the stiffness matrix. The individual coefficients of the matrix are calculated by determining the force required at a given point to move any other point a unit distance. These were found by using the moment-area method (Thomson, 1972). Equation 3.28 implies that the motion of each element is in one coordinate direction, and for small deflections this approximation does not lead to a significant error however for some combinations of cantilevers and values of dynamic loading this approximation is not suitable. For larger deflections the above model would increase the distances between adjacent elements and introduce larger errors. To reduce these errors the distances between adjacent nodal points were forced to remain constant and this in turn required the stiffness matrix to be updated at each timestep. For cantilevers which have large elastic deflections before the onset of plastic deformation a proper two-dimensional simulation would be needed to more accurately describe the motion of the cantilever.

To obtain a solution to the motion of a cantilever, this set of equations (equations 3.28) must be numerically integrated over time using many small timesteps. These timesteps cannot be arbitrary however. If the timesteps are too large the program will become unstable and if too small the execution time of the program will be large. A safe criterion for the stability this numerical model is based on the condition that a

sound signal propagating within the material from one node to the next must not be able to reach the next node within one timestep. The timestep chosen must therefore be some fraction of the transit time and for this program the fraction was set at $\frac{1}{2}$. The velocity of sound(or the velocity of a longitudinal elastic wave) in the solids used here can be approximated as being $\sqrt{E/\rho_m}$(Stephens et al, 1966), so that the timestep can be defined as

$$dt = \frac{1}{2}\frac{dx}{\sqrt{E/\rho_m}}, \tag{3.29}$$

where dx is the length of the smallest element and ρ_m is the density of the material.

The above elastic program was used to drive the plastic deformation portion of the program by using the criterion that the curvature of the cantilever could not exceed a certain maximum.

Two reference frames were used for the calculation. The first was the elastic reference frame which rotates with the plastic deformation of the hinge and is where the elastic response of the cantilever is calculated. The second reference frame was the laboratory frame. The origins of both reference frames were coincident. A fourth order polynomial of the form

$$y(x) = a_2x^2 + a_3x^3 + a_4x^4 \tag{3.30}$$

was used to fit the first three nodal positions in the elastic reference frame. The first two coefficients were set to zero because of the boundary conditions at the clamped end of the cantilever, namely $a_0 = 0$ since the cantilever is hinged at the origin and $a_1 = 0$ because in this frame the slope at the origin must be zero.

The second derivative with respect to x of the above function was taken and evaluated at the origin, yielding a value of $2a_2$. Substituting this into equation 3.15 gives

$$a_2 = \frac{M}{2EI} \tag{3.31}$$

and is the condition for the onset of plastic deformation. The right hand side of 3.31 sets a maximum to the size of a_2 since the material can only withstand a finite amount of curvature before plastic deformation ensues. At every timestep during the calculation a fit was done to the nodal points in the elastic frame to determine the value of a_2. If the loading is sufficiently large then at some time a_2 will exceed the above limit and a plastic deformation will begin.

To determine the amount of plastic deformation a second fit was done which was of the form

$$y(x) = a_1 x + \frac{M}{2EI} x^2 + a_3 x^3 + a_4 x^4. \tag{3.32}$$

According to 3.27 a minimum in curvature exists at the origin when $y(x)$ is rotated by an angle of $-atan(a_1)$. The cantilever seeks out this minimum and deforms the required amount since its curvature cannot exceed this amount for a given material. In the numerical solution this angle is the amount of plastic deformation that occurred for the particular timestep. All the nodal points in the elastic reference frame were then rotated back by this same angle to be ready for the next timestep. This algorithm keeps the bending moment at the hinge in the elastic reference frame equal to the maximum bending moment allowed by the material.

Figure 3.10 shows the deformation time history obtained by using a five element numerical simulation of a 0.2 m long cantilever made of aluminum 4043 with a diameter of 1.55 mm that has been loaded within the shock tube. Also plotted in this figure are the bending moment at the hinge and the maximum that can exist within the material. The two curves are almost indistinguishable, however the moment after the rotation is slightly less, which is required by the material. The maximum bending moment is not a horizontal line, as it would be if no strain hardening effects were included in the solution. The bend angle time history shows various oscillations at periodic intervals which are due to the existence of higher modes within the cantilever. These higher modes create a variation in curvature at

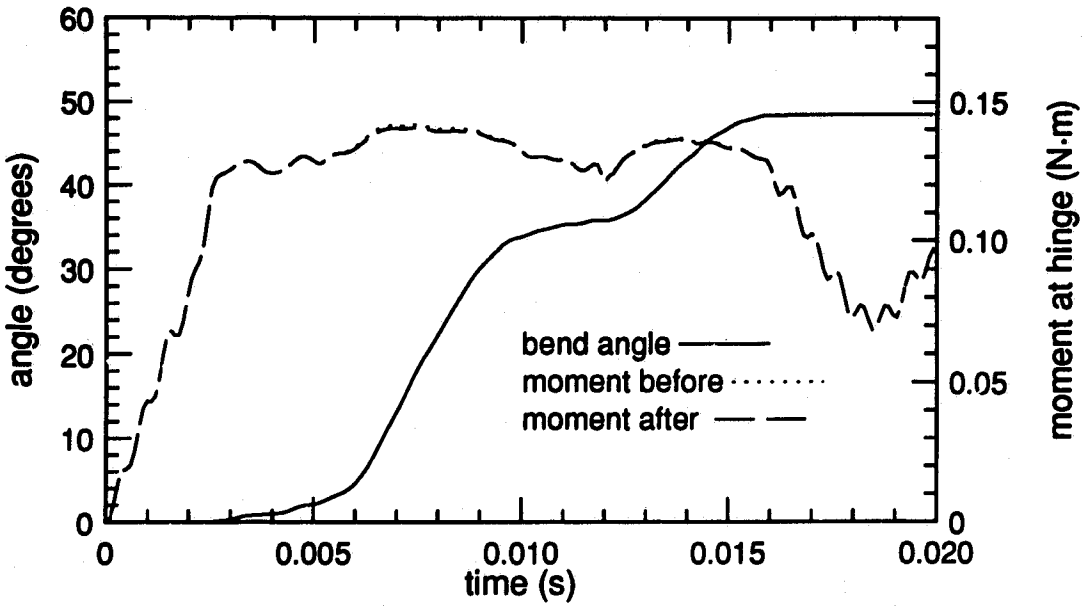

Figure 3.10: The deformation and hinge-moment time histories of a 0.2 m long, 1.55 mm diameter cantilever made from al4043 subjected to a shock tube flow produced by a M=1.23 shock wave. Two moments are shown, one before rotation of the cantilever and one after rotation.

the hinge which in turn causes a nonuniform deformation rate.

To test the consistency and stability of the algorithm several runs of the program were performed using the same initial conditions but varying the number of elements and hence timesteps. The results of this test using 3, 5, 20, and 35 elements are given in figure 3.11 and it is seen that there was a rapid convergence to a stable solution. All of the final deformation angles were within one degree of one another for this particular test. A 35 element run takes approximately 28 min on a 66 MHz 486DX2 computer while a 5 element run takes 9 seconds on the same computer(see figure 3.12). For most calculations performed for this dissertation either a 5 or 10 element run was used since the small gain in accuracy by using a larger number elements did not justify the increased calculation time.

Some materials when being plastically deformed under dynamic loads can with-

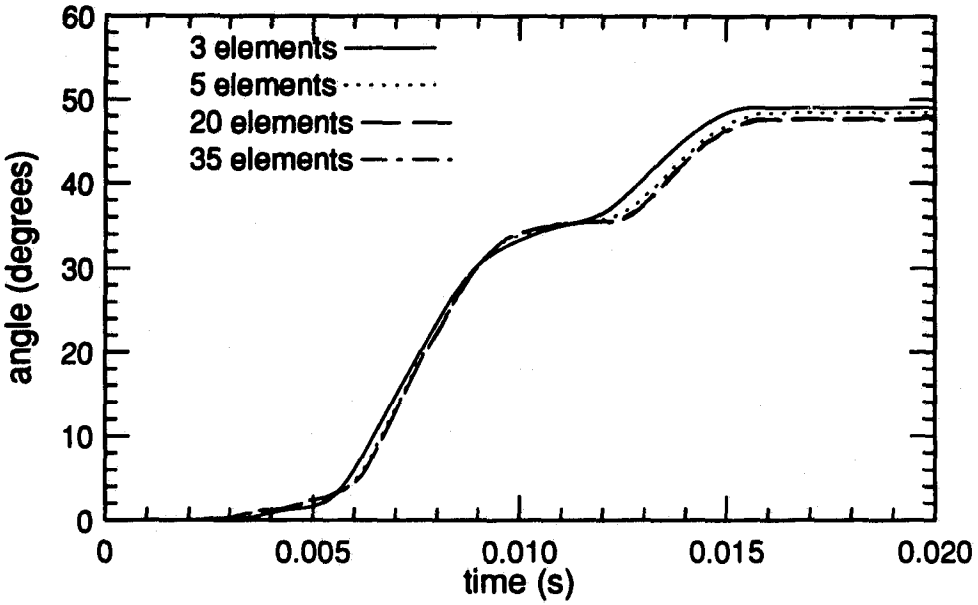

Figure 3.11: Deformation time histories of a 0.2 m long, 1.55 mm diameter aluminum cantilever using different numbers of elements.

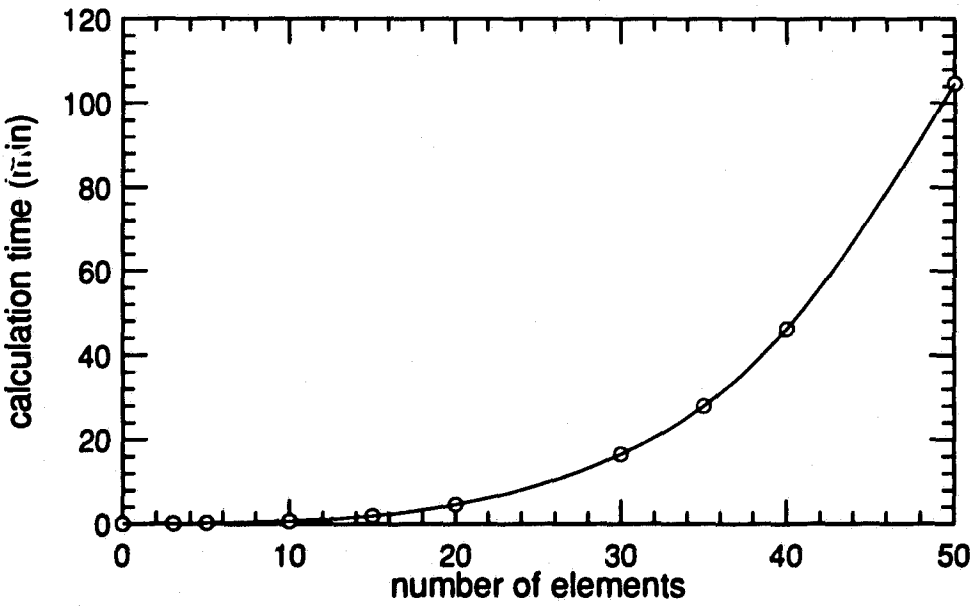

Figure 3.12: Calculation time for the cantilever described in figure 3.11 versus the number of elements.

stand larger strains than when the loads are applied slowly. The increase in the amount of strain can be 1.5 times or more depending on the material. Two types of material "strengthening" can take place, strain hardening and strain-rate hardening. Strain hardening is the amount of strengthening that occurs when a material has already undergone a permanent deformation. It was introduced in the above solution by assuming a linear relationship between stress and strain after first yielding. The equation used was obtained from Mendelson (1968) and is

$$\sigma_y = \sigma_{yu} + k\frac{\delta L}{L}, \tag{3.33}$$

where σ_y is the static maximum yielding stress, σ_{yu} is the unstrained yielding stress, k is the slope of the stress-strain curve after yielding(see figure 4.1) and $\frac{\delta L}{L}$ is the strain. This equation is valid for rigid-plastic work hardening which is the assumed response for the hinge.

Strain-rate hardening is the increase in material strength that occurs when high rates of strain occur within the material. It was introduced by using the Cowper-Symonds law(Ting and Symonds, 1962) which gives a relationship between the effective dynamic yielding stress of the material and the strain-rate viz.

$$\sigma_{yd} = \sigma_y(1 + (\frac{\dot{\epsilon}}{F})^{\frac{1}{p}}), \tag{3.34}$$

where σ_{yd} is the maximum dynamic yielding stress, $\dot{\epsilon}$ is the strain rate and p and F are constants for the various materials and are determined by experiment. The values used here were obtained from Parkes (1958) and Manjoine (1944).

The model used to calculate the elastic response of the cantilever is one-dimensional and as such does not include in its response calculations the cross-section of the cantilever. To include these strain hardening effects a gauge length as well as a cross section for the region of plastic bending is needed. Measurements of many plastically deformed cantilevers have shown that the majority of plastic deformation was

generally confined to a region which began at the clamped end and extended approximately $\frac{\pi}{2}d$ up the rod, where d is the diameter of the rod. This corresponds to a bending radius that is equal to the diameter of the rod. With the above assumptions strain rates of approximately $80s^{-1}$ have been calculated for the outer filaments of cantilevers loaded in the shock tube.

3.4.4 Brittle cantilevers:Rigid-brittle

Some materials such as graphite and glass break rather than bend when rapidly loaded and as a consequence are called brittle. In theory, a brittle cantilever breaks when the imparted load produces a stress in the material which exceeds the maximum yield stress of that material. In the rigid-brittle model it is assumed that, since the response time of the cantilever is significantly smaller than the duration of the positive phase of dynamic pressure, the cantilever will essentially respond to peak dynamic pressure. This model also assumes that the load is instantly transmitted to the base and that the elastic motion is negligible. The force on the rod due to blast loading and the resistance the rod gives before failure are determined in the same way as that for the bending cantilevers. For the cantilever to fail the loading force must be greater than the resisting force. This is shown in the equation

$$C_d P_{kd} L d > \frac{4}{3}\sigma_y (\frac{d}{2})^3 \tag{3.35}$$

where C_d is the drag coefficient, P_{kd} the peak dynamic pressure ($\frac{1}{2}\rho u^2$), L and d the length and diameter of the rod respectively and σ_y the stress required to break the cantilever. Under this condition the cantilever breaks and gives a lower limit to the peak dynamic pressure. If however, the cantilever does not fail an upper limit is determined. To enhance results one can position a series of rods with different lengths and expose them to a blast wave with the objective of having the longer rods fail and the shorter rods not fail. In this way the peak dynamic pressure value is

bracketed with a resolution depending on the increment in length between rods in the series.

Chapter 4

Experimentation

4.1 Material properties

Cantilevers constructed of different materials were tested in both the shock tube and HE events. Each cantilever was made from one of the following materials: aluminum 4043; aluminum 5056; aluminum 6061; steel 1018; solder(50/50 lead/tin), or graphite. The pertinent mechanical properties of the materials such as the Young's modulus, the yield moment, and the strain-hardening coefficients were needed if a model was to be created. These values were obtained from the literature or a tension or bending test.

The tension test involved the use of a machine at the University of Victoria's Mechanical Engineering department which applied a tension load to a cylindrical sample of material. The sample was machined so that the center of the rod was a smaller diameter than the outer ends. This central portion was uniform in its cross-section while the outer ends were enlarged to fit the jaws of the machine. This is done to force a failure of the specimen in the central region and not in a region where the stresses would not be so easily calculated. An extensometer was used to measure the amount of elongation of the specimen while under load so that a stress-strain diagram could be made. These diagrams provide the Young's modulus, the yield stress and the values of strain hardening. Two samples were tested on this machine, one made of aluminum 6061-T6 and another made of steel 1018. The

resulting stress-strain diagrams are given in figure 4.1.

This machine could not be used for all materials since its lower load limit produced stresses in some materials which exceeded the yielding stresses. These samples were either made from wires or welding rods whose diameters were no larger than 1.55 mm and therefore needed smaller loads to produce plastic deformation. To obtain approximate values of yielding stresses for these materials two types of tests were performed. One was a simple tension test which was accomplished by placing longitudinal loads on a small sample and determining the minimum load required to produce a plastic deformation. The second test was a bending test which was more applicable to the type of failure that occurs in the dynamic loading of a cantilever. This method involved determining the minimum moment about the base required to produce a plastic deformation at the base. The results from these tests were compared to the values obtained by reviewing the specification sheets obtained for the materials and in most cases were consistent. The relevant material properties are given below in table 4.1.

The strain rate hardening data were obtained from the experimental and theoretical work of both Manjoine (1944) and Parkes (1958) and are reproduced in figure 4.2. The results of Parkes were for various aluminum alloys and were based on the limited available literature. Bodner and Symonds (1962) used the results of Parkes to describe the rate-sensitivity characteristics of aluminum 6061-T6 and obtained reasonable agreement with experiments involving the deformation of impulsively loaded cantilevers. However it should be noted that the results for the aluminum alloys can only be considered a rough approximation to the characteristics of 6061-T6. The results of Manjoine for mild steel were used to describe the rate-sensitivity characteristics for the 1018 steel, and this is also a rough approximation.

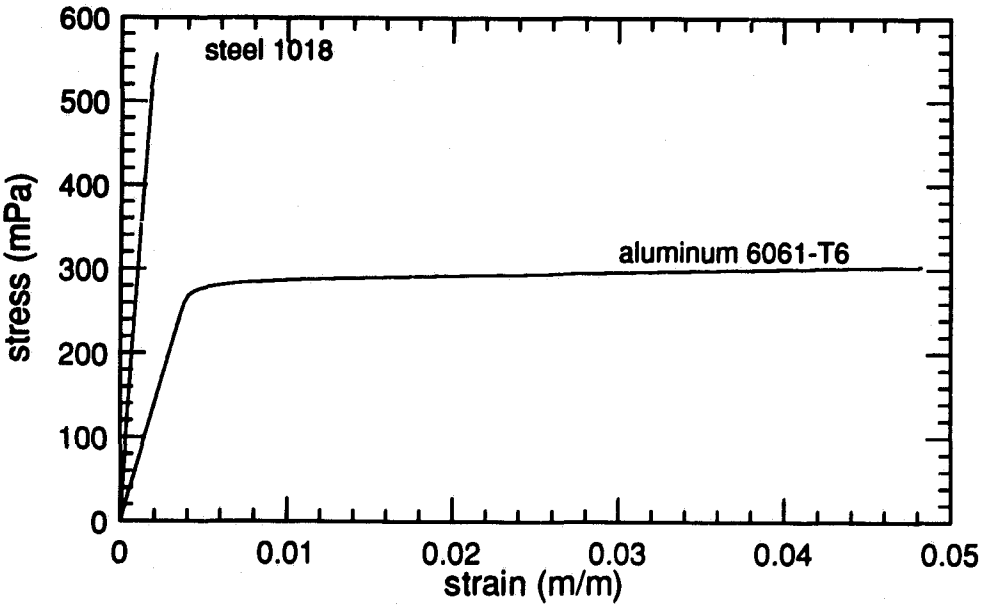

Figure 4.1: The stress-strain diagram for aluminum 6061-T6 and steel 1018.

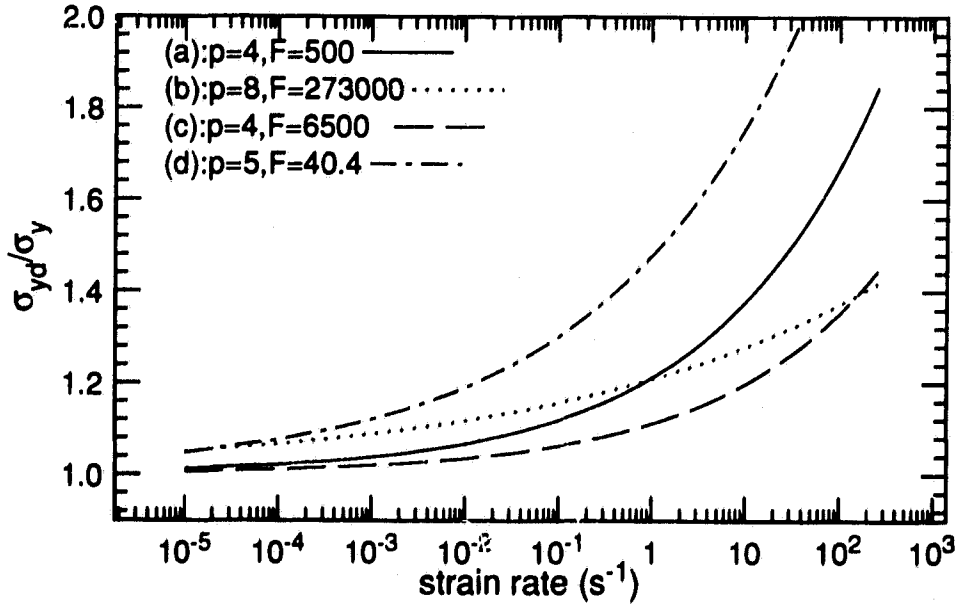

Figure 4.2: Effect of strain-rate on the yield stress of various aluminums not specified(a,b,c) and mild steel(d), refer to equation 3.22. These data are obtained from Parkes (1958) and Manjoine (1944).

Table 4.1: Material properties.

Material	Yield Stress (σ_y) (Pa)	Young's modulus(E) (Pa)	Density (kg/m^3)	Testing method
al 6061-t6	2.8×10^8	8.6×10^{10}	2.699×10^3	tension
al 4043	1.8×10^8	7.0×10^{10}	2.699×10^3	bending
al 5056	2.7×10^8	7.0×10^{10}	2.699×10^3	bending
solder 50/50	3.3×10^7	9.3×10^{10}	9.439×10^3	bending
steel 1018	5.6×10^8	2.8×10^{11}	7.870×10^3	tension
HB graphite	2.2×10^8 †	1.1×10^{11}	1.793×10^3	bending

†stress required for breaking.

4.2 Shock tube

The shock tube experiments were carried out using ductile cantilevers made of aluminum 4043, aluminum 5056 or 50/50 solid solder wire. Experiments were also done using brittle cantilevers made from HB graphite pencil leads. Experiments were performed using cantilevers whose lengths varied from 0.25 m to 0.03 m to test the various numerical models and to see which cantilevers would have the correct characteristics to be used as a gauge.

In all experiments the cantilevers were positioned in the expansion chamber of the shock tube 3.15 metres from the diaphragm. This position was chosen to minimize any effects on the deformation process due to nonuniformity of the shock wave close to the diaphragm and reflections from the end of the tube. A shock tube section which contained an access port and a window was made and positioned 3.15 m from the diaphragm. Along the center line of both the ceiling and the floor of this section a series of holes were made at 0.10 m intervals. Specially machined bolts were placed in these holes so that their ends would be flush with the inside surface of the shock tube to minimize any effects on the shock tube flow. These bolts were used to hold the

cantilevers firmly in place by drilling holes along their central axis to accommodate the different diameters of cantilevers. A small set screw was used to press against the portion of the cantilever in the bolt to stop any motion of the cantilever within the bolt.

Two types of experiments were performed on the ductile cantilevers. The first involved the measurement of the final deformation angles of the cantilevers after the passage of a shock wave. A second set of experiments was performed using a HI-CAM high speed camera operating at framing rates from 1000 to 5000 frames/sec to observe the dynamics of the deformation processes.

4.2.1 Final deflection measurements

Many experiments were performed within the shock tube on ductile cantilevers constructed of aluminum 4043, aluminum 5056 or solder wire (50/50 lead/tin) to determine the final angle of deformations. The aluminum and solder cantilevers had diameters of 0.15 cm and 0.10 cm respectively. The incident shock Mach numbers were varied between 1.20 and 1.45, providing deflection angles between 0° and 90°. The angular deflections of the cantilevers were measured with a standard protractor. The results of these experiments along with the theoretical values obtained by the various models are presented in chapter 5.

4.2.2 High speed photography

The film used for the high speed photography was 16 mm Kodak RAR 2479 in 125 foot rolls which provided records for approximately 1.5 seconds at 5000 frames/sec and about 6.0 seconds for 1000 frames/sec. At these framing rates diffused front lighting was insufficient to illuminate the cantilevers and obtain a proper exposure. A shadow photographic system was therefore used in conjunction with a retro-reflective background, as shown in figure 4.3. The retro-reflective material was recessed 1/4

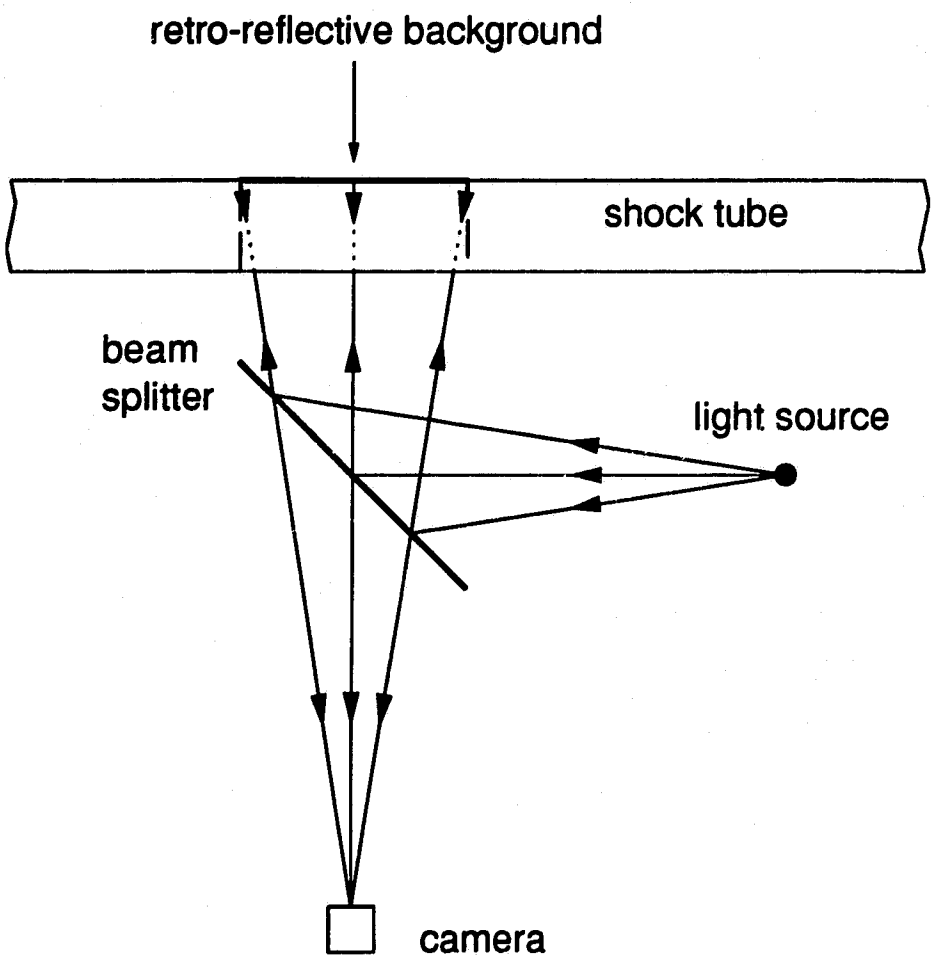

Figure 4.3: Optical arrangement for illuminating the window section of the shock tube during high speed photography.

inch in the back wall of the window section and covered by a 1/4 inch plexi-glass sheet on which a centimeter scale grid was etched. The camera was placed perpendicular to the window section and a 1000 Watt bulb was placed at 90 degrees to the camera-window line. A large sheet of 2.5 mm thick glass was used as a beam splitter to reflect the light towards the window section. The distance from the camera to the window section was made equal to the distance the light travels from the bulb to the window section via the splitter in order to optimize the effect of the retro-reflector. The light from the bulb reflected from the beam splitter and struck the retro-reflective background which reflected the light back along its original path. Some of this light reflected off of the splitter back to the light source while the rest propagated through the splitter towards the camera where it formed an image of the light source. This configuration produced a bright background with a dark cantilever superimposed when viewed from the camera position and gave ample light for photography. Four high speed films were taken of various cantilevers made from aluminum 4043 under shock tube loading.

The framing rate of the camera was measured in each experiment by flashing an LED onto the edge of the film at 1000 Hz. This produced a series of small circular dots spaced at $1/1000^{th}$ of a second. A time for each frame was calculated by measuring the relative position of each frame with respect to these dots. The time versus frame number is given in figure 4.4 for each of the four experiments. The zero frame was defined as the last frame before the cantilever was observed to move. The conditions of each experiment are given in table 4.2.

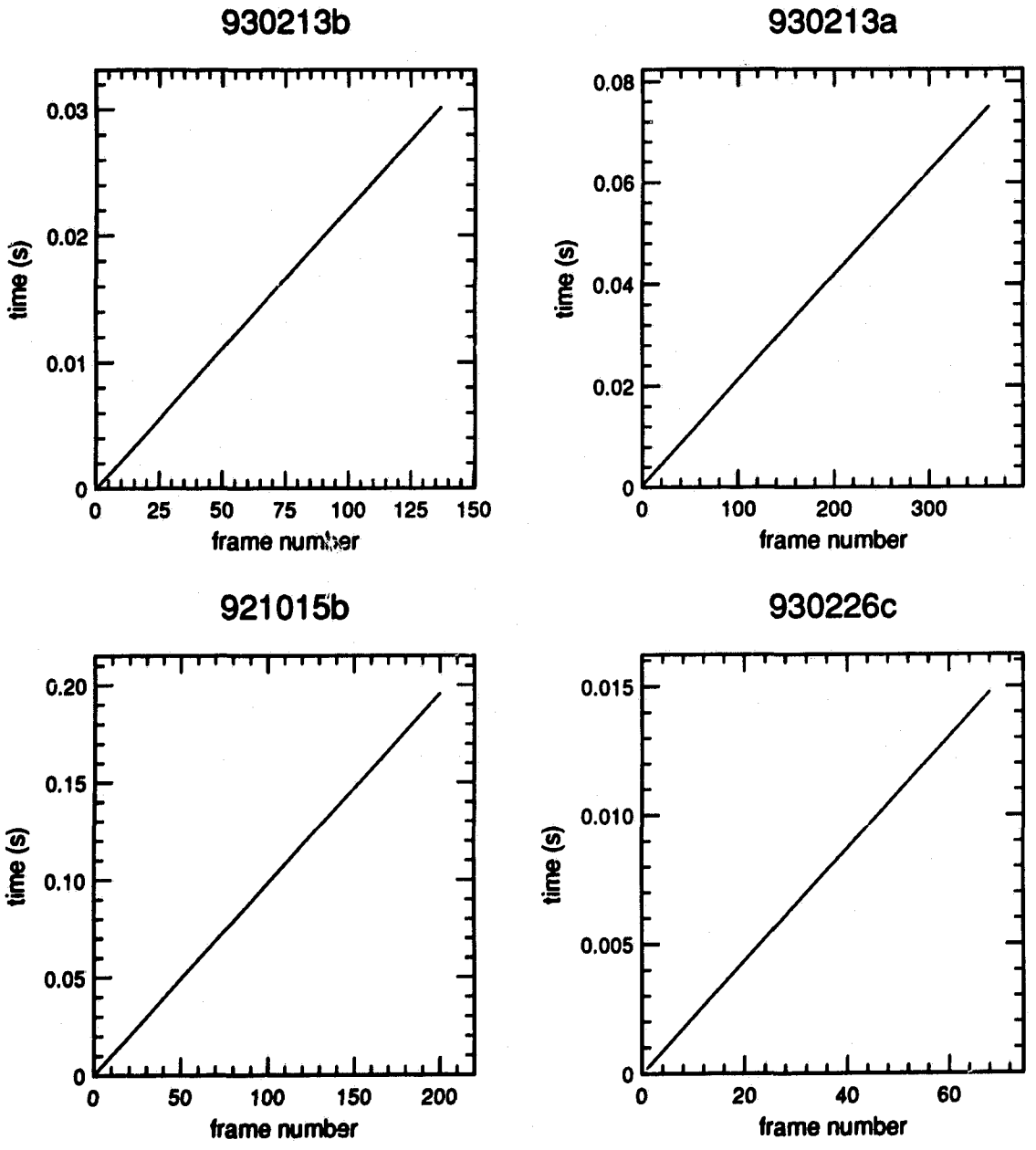

Figure 4.4: Timing versus frame number for the high speed photography experiments. Zero time was assigned to the last frame before the cantilever was seen to move.

Table 4.2: High speed photography experiments.

Experiment #	Framing rate (Hz)	Incident shock Mach number	Cantilever length (m)
921015b	1020	1.23	0.20
930213a	4530	1.32	0.10
930213b	4570	1.24	0.15
930226c	4560	1.40	0.06

4.2.3 Brittle cantilevers

The brittle cantilevers were constructed mainly of ITOYA 0.5 mm HB graphite pencil leads. These cantilevers were designed to break at certain values of peak dynamic pressure depending on their lengths, the longer ones breaking at lower dynamic pressures than the shorter ones. Experiments were performed in the shock tube to test the applicability of equation 3.35 and to calibrate the cantilevers that were used at MINOR UNCLE.

The calibration process used cantilevers that had the same length as the two cantilevers in the field which bracketed the peak dynamic pressure. In most instances the difference in the lengths of the two cantilevers was approximately 2.5 mm. Repeated experiments were done on each pair of cantilevers until it was found that the longer one broke but the shorter one did not. Under this condition the peak dynamic pressure was bracketed since it was insufficient to break the shorter cantilever but large enough to break the longer of the two. The peak dynamic pressure was determined in the following way. First the the Mach number of the incident shock is obtained by measuring the incident shock velocity and ambient sound speed. The Mach number was then used in the shock front equations to obtain the hydrostatic pressure ratio and the density ratio. With the hydrostatic pressure ratio the induced flow velocity can be calculated by equation 2.6. The peak dynamic pressure can

then be determined by equation 2.20. This was done for cantilevers whose lengths varied from 3.25 cm to 7.5 cm and the results of length of cantilever vs peak dynamic pressure are plotted in figure 4.5.

4.3 High explosive tests

4.3.1 Introduction

The primary objective of participating in the high explosive tests was to evaluate the ability of the numerical modelling technique to predict the deformation of a variety of cantilevers when exposed to blast waves whose physical properties were well known.

The cantilevers were exposed to the blast waves from two high explosive detonations of ANFO at White Sands Missile Range, New Mexico. The code names were DISTANT IMAGE and MINOR UNCLE and are high explosive tests sponsored by the Defence Nuclear Agency of the United States and made available to scientists of many countries.

The DISTANT IMAGE test was carried out in 1991, at which time only the rigid-plastic model had been developed. The test showed that the model gave good predictions only for the solder cantilevers. The MINOR UNCLE test was carried out in 1993 by which time the elastic-plastic model was being developed, and improved predictions of the deformations of the aluminum and steel were obtained. The two tests provided a large body of data over a wide range of peak dynamic pressures that could be used to evaluate the models finally developed and also future models.

Each explosive charge was contained within a hemispherical fiberglass dome of radius 9.75 m and placed on the ground surface. The charge sizes for DISTANT IMAGE and MINOR UNCLE were 2,650 and 2,431 tons respectively and both were initiated by a 275 lb. Octal booster. The ambient conditions at the time of the tests are given in table 4.3 below.

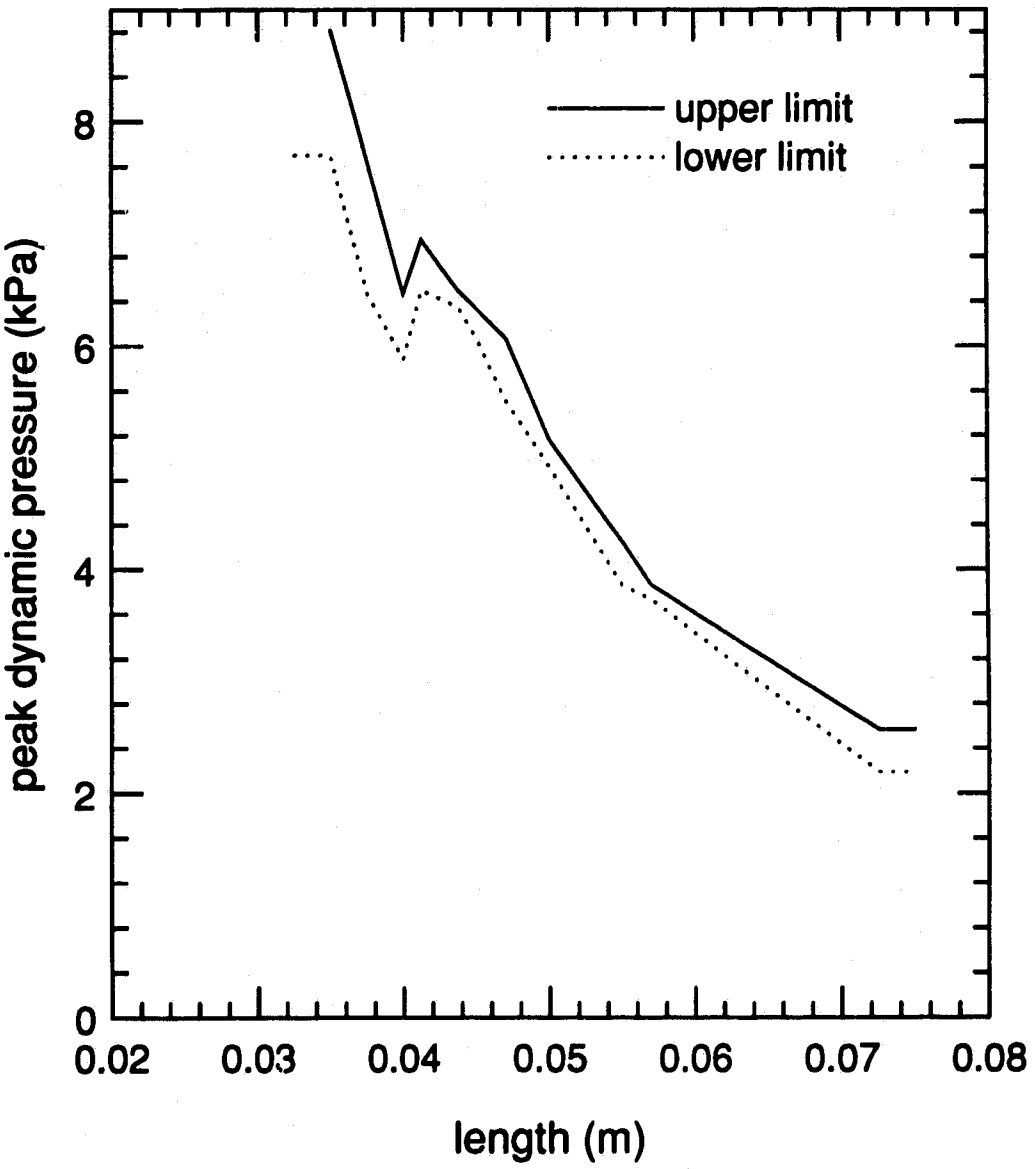

Figure 4.5: The peak dynamic pressure required to break 0.5 mm diameter graphite cantilevers of different length within the shock tube.

Table 4.3: Test ambient conditions.

Event name	Date detonated	Pressure (kPa)	Temperature (° C)	Humidity (%)
DISTANT IMAGE	June 20/1991	85.29	24.7	27
MINOR UNCLE	June 10/1993	85.29	20.7	38

4.3.2 Cantilever layouts

The cantilevers exposed at the HE test were made from materials that were either ductile, *i.e.* were permanently deformed after being strained beyond the elastic limit, or brittle, in which case they fractured if strained a small amount. Each cantilever consisted of a rod or wire which was clamped at its base. The larger rods were set into the ground with concrete, while the smaller wires were mounted on streamlined platforms bolted to posts which were set in concrete.

At DISTANT IMAGE 123 cantilever positions were established along arcs at 31 stations at different distances from the charge. At MINOR UNCLE there were 121 cantilever positions along arcs at 45 different distances. The surveyed positions of the cantilevers are given in Appendix B for DISTANT IMAGE and in Appendix A for MINOR UNCLE. The arcs of cantilevers were distributed between the predicted hydrostatic overpressure levels of 1379 kPa (200 psi) and 21 kPa (3 psi) which correspond to a distance range of 118 m (386 ft) to 939 m (3080 ft). On each arc there was between 2 to 15 cantilevers separated by about 0.6 m (2 ft). The positions of the cantilever stations for the two events are given in figures 4.6 and figures 4.7.

With the exception of some of the vertical arrays of cantilevers discussed in 4.3.5, the cantilever stations were all on a radial through the charge center which had been graded, rolled and covered with dust suppressant. This provided for an unobstructed passage of the blast wave with a ground roughness in the order of 1 cm. At numerous positions along this radial there were electronic hydrostatic and dynamic pressure

gauges (Teel, 1992, 1995). The same radial was also used for smoke puff photodiagnostics (Dewey, et al 1992, 1995), so that the flow properties of the blast waves along the radial at which the cantilevers were placed, were well defined. A typical overview of a station at MINOR UNCLE is shown in figure 4.8.

4.3.3 Ductile cantilevers

The ductile cantilevers were constructed from readily available materials, *viz.* aluminum 6061-T6, aluminum 4043, aluminum 5056, cold rolled steel 1018, and solder (50/50 tin/lead). The cantilevers were circular in cross-section and varied in diameter from 2.54 cm (1.0 in) to 1 mm (0.04 in), and in length from 1.7 m (5.6 ft) to 2 cm (0.8in). The radial distances and specifications of each gauge is given in Appendices A and B.

The larger cantilevers, with diameters ranging from 3.2 mm (0.125 in) to 2.54 cm (1.0 in), were positioned in circular holes drilled into the ground 0.6 m (2.0 ft) deep and 15 cm (6.0 in) wide and filled with concrete. These cantilevers were constructed from aluminum 6061-T6 or cold rolled steel 1018, and were positioned at distances from GZ between 118 m (386 ft) and 939 m (3080 ft) for DISTANT IMAGE, and for MINOR UNCLE were positioned between 118 m (386 ft) and 664 m (2180 ft). Typical steel and aluminum cantilevers are shown in figure 4.9.

The smaller cantilevers had diameters which ranged from 1.5 mm (0.06 in) to 1.0 mm (0.04 in), and were supported on streamlined platforms which could each hold seven cantilevers as shown in figure 4.10. The platforms were mounted 0.6 m (2.0 ft) above the ground on stands which were concreted in position. The platform mounted cantilevers were made from aluminum 4043 or 5056 welding rod, or solder wire (50/50 tin/lead). The platforms at DISTANT IMAGE were positioned at radial distances from GZ which ranged from 451 m (1480 ft) to 939 m (3080 ft) and for MINOR UNCLE the range was from 519 m (1703 ft) to 939 m (3080 ft). The

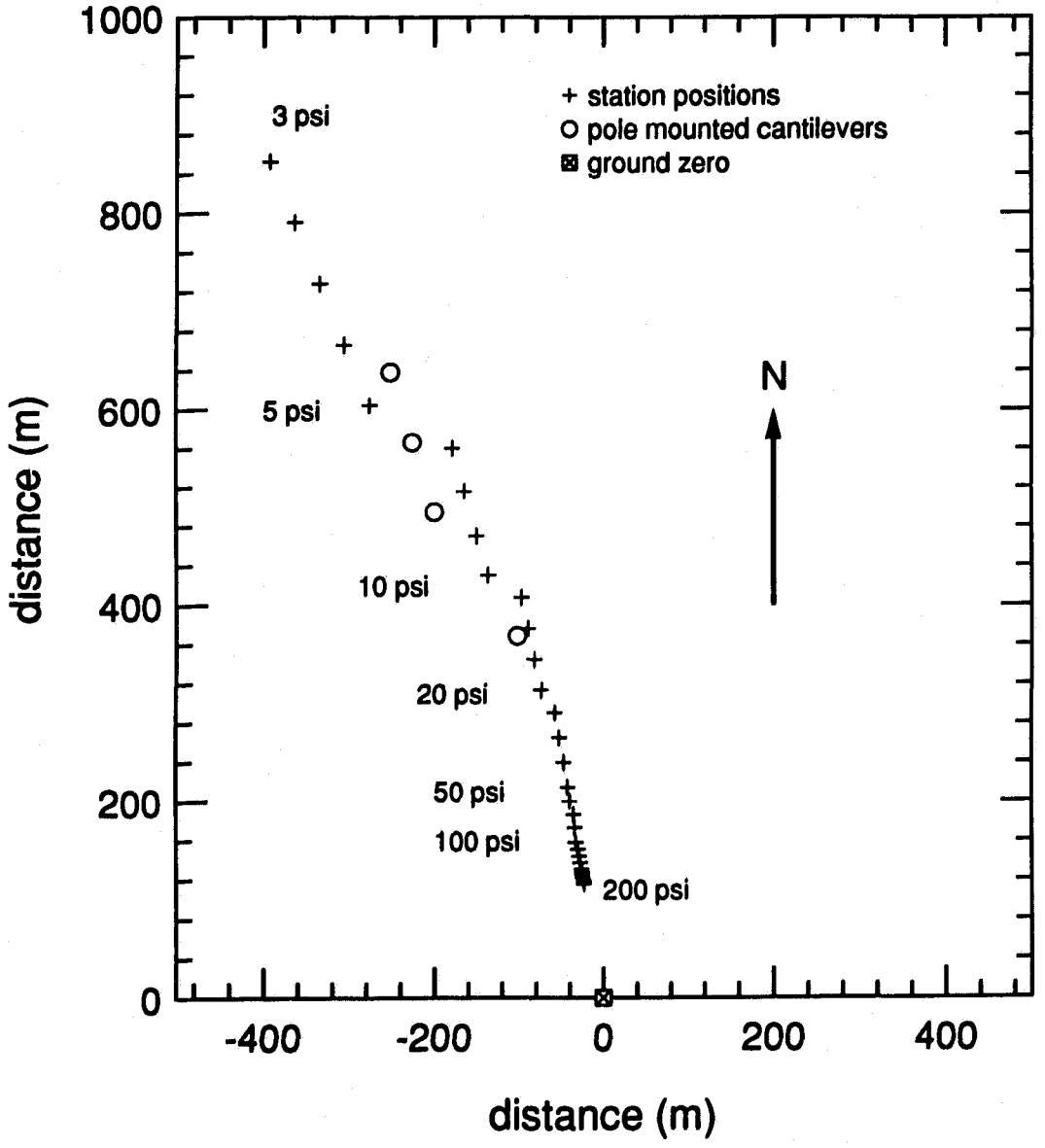

Figure 4.6: Positions of cantilever stations at DISTANT IMAGE.

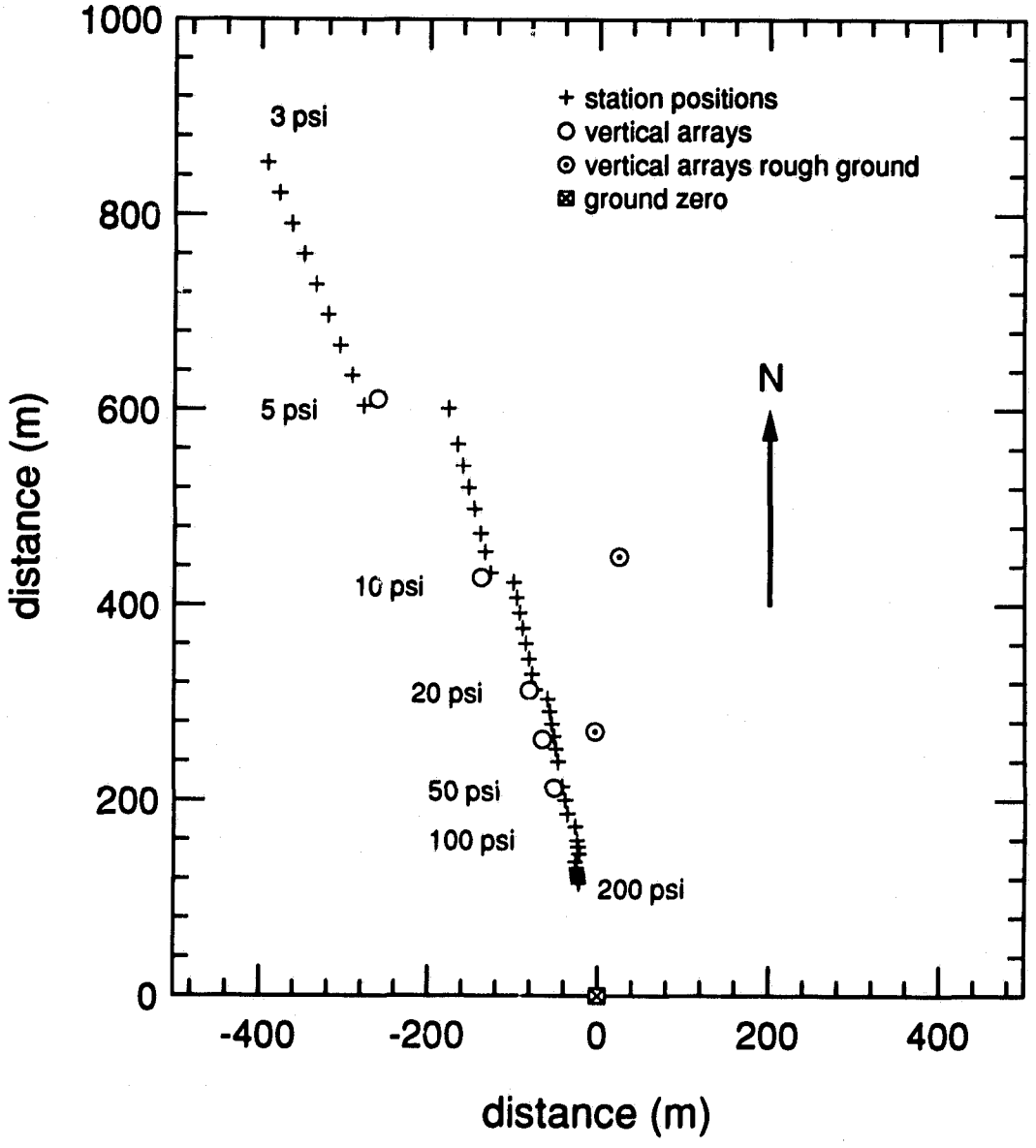

Figure 4.7: Positions of cantilever stations at MINOR UNCLE.

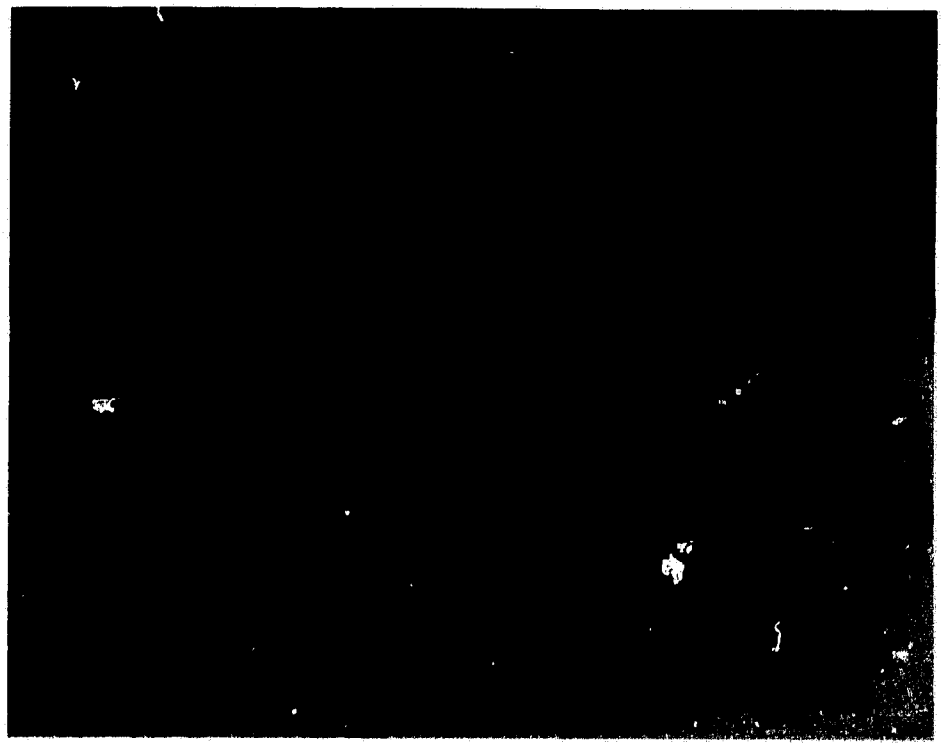

Figure 4.8: Photograph of station 321 m from the charge at MINOR UNCLE showing, from left to right, four cantilevers, four dynamic pressure impulse cantilevers, smoke puff launcher, vertical array of horizontally mounted cantilevers, displacement cubes and electronic pressure gauge.

angular deflections of the platform mounted cantilevers were measured with a standard protractor while the deflections of the larger cantilevers were measured with an instrument called a gunner's quadrant. The latter is a device which is generally used to measure the angle of tilt of a gun barrel.

4.3.4 Brittle cantilevers

The brittle cantilevers at DISTANT IMAGE were constructed from either ITOYA 0.5 mm HB or STAEDLER 2.0 mm H graphite pencil leads. Sets of cantilevers were positioned on streamlined platforms at distances from GZ of 451 m (1480 ft), 664 m (2180 ft), and 938 m (3080 ft). The platform at 451 m contained two sets of cantilevers: seven made of ITOYA graphite and seven made from the STAEDLER graphite. All the other stations seven of the ITOYA cantilevers only were used. The increment in length between adjacent cantilevers was 1.0 cm. DISTANT IMAGE was the first experiment on which the brittle cantilevers were used and to assure that over a wide range of peak dynamic pressures some of the cantilevers would fail and others would not a large length differential was used.

At MINOR UNCLE brittle cantilevers made only from ITOYA 0.5 mm HB were used. Based on the information learned at DISTANT IMAGE, they were positioned at distances from the charge center of 565 m (1854 ft), 626 m (2055 ft), 664 m (2180 ft), 699 m (2292 ft), 767 m (2517 ft), and 836 m (2742 ft). Each platform supported 15 cantilevers with increments in length of 2.5 mm which provided essentially 4 times the resolution that existed at DISTANT IMAGE.

The specifications of each platform for each event are given in Appendices A and B.

4.3.5 Vertical arrays of horizontally mounted cantilevers

Cantilevers respond to the dynamic pressure of a blast wave and thus are sensitive to variations in the particle velocity. It has been suggested therefore that vertical

Figure 4.9: Photograph of steel and aluminum cantilevers mounted in the ground at MINOR UNCLE 321 m from the charge(white dome in background). From left to right the cantilevers are: 1.0 m long, 1.27 cm diameter steel 1018; 0.6 m long, 1.27 cm diameter aluminum 6061; 1.0 m long, 1.27 cm diameter aluminum 6061; and 1.66 m long, 2.54 cm diameter aluminum.

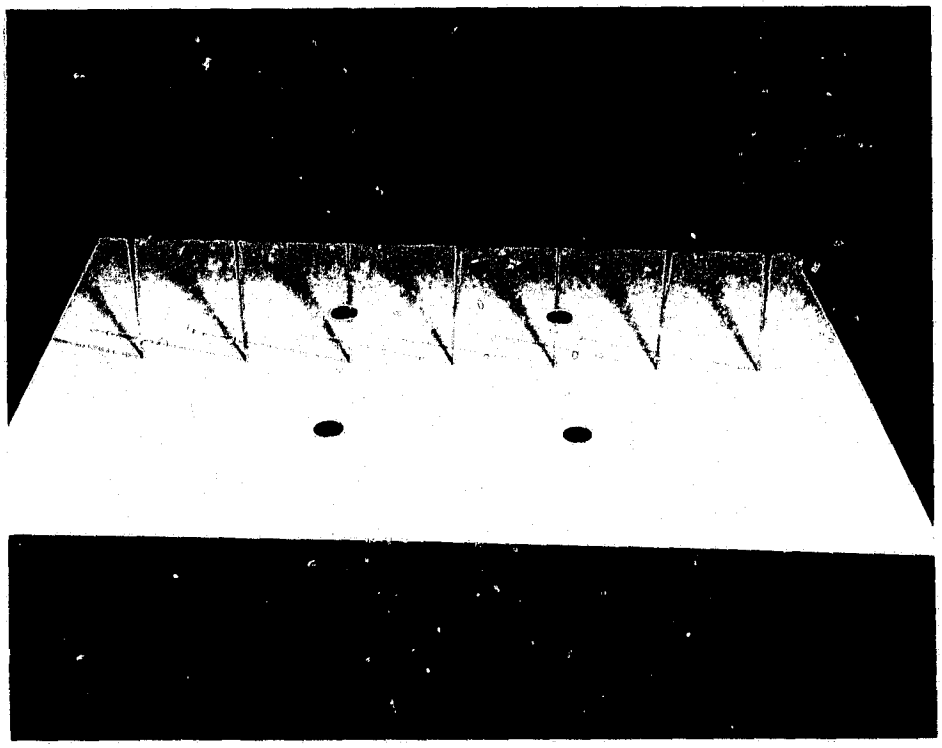

Figure 4.10: Photograph of platform mounted cantilevers at MINOR UNCLE.

arrays of horizontal cantilevers might be used to determine the height of the boundary layers produced by the blast wave travelling over the ground surface. Very little information is available about this phenomenon.

At DISTANT IMAGE advantage was taken of four wooden poles, 23 cm in diameter, which were used to support the cantilevers. The poles were positioned on graded ground at distances from GZ of 382 m (1254 ft), 534 m (1751 ft), 610 m (2000 ft) and 686 m (2250 ft). The cantilevers used on the poles were made from aluminum 4043 welding rods with diameters of either 0.32 cm (1/8 in) or 0.48 cm (3/16 in). 16 or 17 cantilevers were mounted perpendicular to the flow on both sides of each pole at heights from ground level to 3.75 m (12 ft). All cantilevers on one side of a pole were the same length, and a different length was used on the other side. This was done to increase the chance of obtaining useful angles of bend. Details of the cantilevers on each pole are given in Appendix B, and a photograph of one of the poles supporting the cantilevers is given in figure 4.11. The poles, which were already in place, were less than perfect mounts for the cantilevers as it could be expected that they would significantly alter some of the airblast characteristics from the free field values.

At MINOR UNCLE this problem was minimized by supporting the cantilevers on streamlined mounts 0.6 m (2 ft) in chord, 2.44 m (8 ft) long and .05 m (2 in) wide. The mounts were placed at distances from the charge of 218 m (718 ft), 270 m (887 ft), 321 m (1058 ft), 451 m (1478 ft), and 664 m (2181 ft) which correspond to predicted hydrostatic overpressure levels of 345, 207, 138, 69, and 34 kPa(50, 30, 20, 10, and 5 psi) respectively. Each mount was placed in a hole approximately 0.91 m (3 ft) deep and set in concrete, with the remaining 0.91 m (5 ft) above the ground used to support the horizontal cantilevers perpendicular to the blast. The streamlined mounts were carefully aligned on the charge center. Eight or fifteen cantilevers were mounted on both sides of each mount at heights above the ground from 3.0 cm (1.18

in) to 1.43 m (4.7 ft) separated by distances of 10 cm (3.9 in) or 20 cm (7.9 in). The cantilevers were made of steel 1018, aluminum 6061 or aluminum 4043, with diameters and lengths that ranged from 1.27 cm (0.5 in) to 0.155 cm (1/16 in), and 0.7 m (2.3 ft) to 0.2 m (7.9 in) respectively. All cantilevers on one side of the mount were of the same length, and in some cases a different length was used on the other side. Details of each mount configuration are given in Appendix A and a photograph is shown in figure 4.12.

The cantilever measurements of the boundary layer over graded ground were coordinated with two other projects. One of these was an attempt to measure the boundary layer growth by high speed photography of particle tracers injected in the air prior to the explosion (McMillin, 1995). This measurement was made at the 34 kPa (5 psi) overpressure.

Computations were performed by Ekler et al (1995) using a two dimensional hydrodynamic simulation called the SHARC code to calculate the time-resolved physical properties of the blast wave as functions of height at the same stations where the horizontal cantilever arrays were positioned. The SHARC code run assumed that the roughness of the graded ground was approximately 6 mm. The results of the above experimental and computational methods will be compared in the next chapter.

Vertical arrays of cantilevers were also used at MINOR UNCLE to measure the boundary layer above ungraded ground. The desert floor at the experiment site was covered with brush to a height of about 0.6 m (2 ft), with approximately 50 % coverage. The ground itself also had an average roughness of several centimeters. The dynamic pressure was therefore expected to significantly less near the the ground than that measured over the graded surface. The cantilevers were mounted on concrete structures already in place from a previous experiment, which were approximately 3.2 m (10.5 ft) long, 1.8 m (5.9 ft) high, and 30 cm (0.98 ft) thick with a blunt leading edge. These structures were used to support a series of horizontal cantilevers

at the hydrostatic overpressure levels of approximately 207 kPa (30 psi) and 69 kPa (10 psi). The cantilevers were vertically spaced at 20 cm (7.9 in) intervals starting at about 3.0 cm (1.18 in) above the ground to about 1.43 m (4.7 ft). Details of these cantilevers are given in Appendix A.

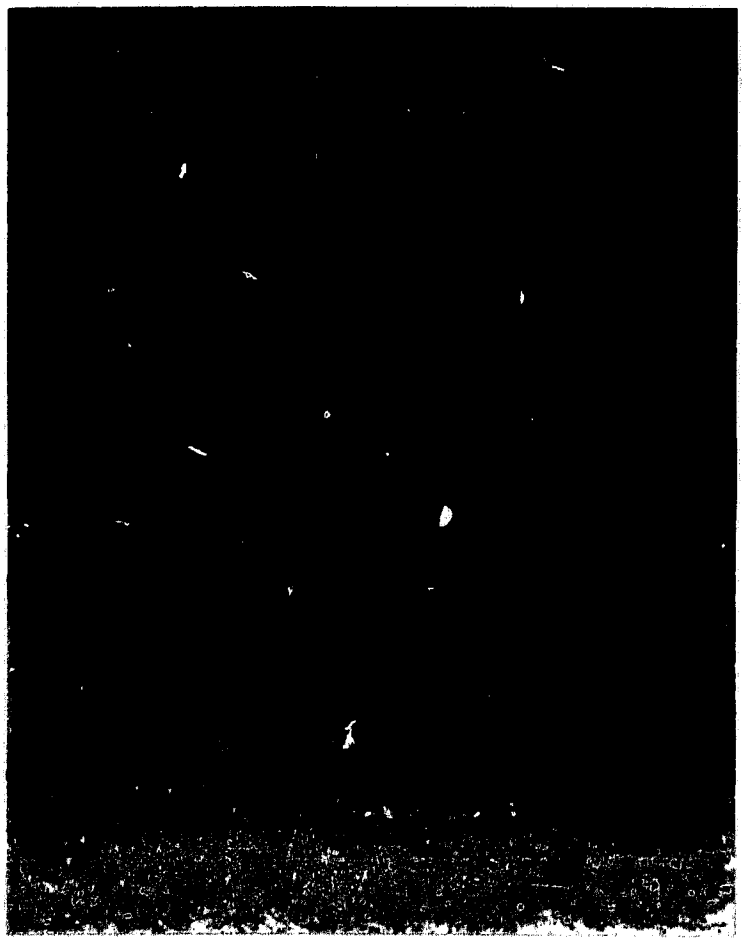

Figure 4.11: Photograph of a vertical array of horizontally mounted cantilevers at DISTANT IMAGE, 658 m from the charge.

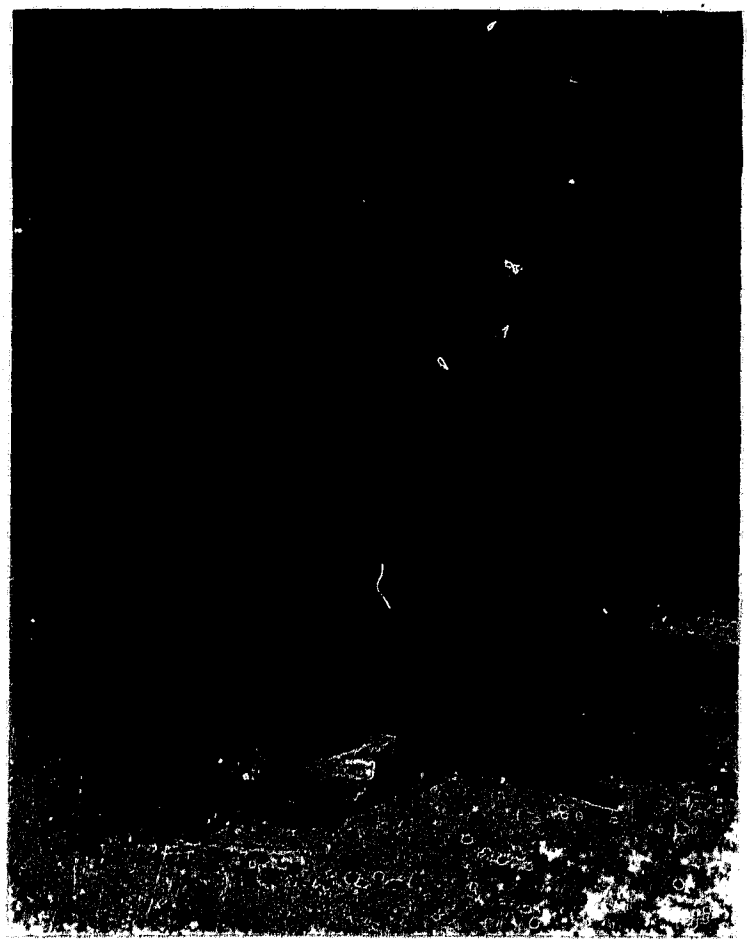

Figure 4.12: Photograph of a vertical array of horizontally mounted cantilevers at MINOR UNCLE, 270 m from the charge.

Chapter 5

Analysis of results

5.1 Shock tube experiments

5.1.1 Evaluation of the rigid-plastic model

The first set of experiments in the shock tube was performed on cantilevers made from solder wire. The length, diameter and composition of the cantilevers were 5.1 cm (2.0 in), 1.0 mm (.040 in) and 50/50 lead/tin respectively, and were similar to the cantilevers used by Dewey (1962). These cantilevers were exposed in the shock tube to shock waves in the Mach number range from 1.1 to 1.27. The angles of plastic deformation of the cantilevers were measured and are plotted against incident shock Mach number in figure 5.1. The repeatability of the final angles for nominally identical experiments was approximately $\pm 5°$. This variability may have been due to inconsistencies in material properties as well other effects such as diaphragm material striking the cantilever.

A single degree of freedom(SDOF) rigid-plastic model as developed in 3.4.2 was used to predict the angle of rotation of the cantilevers. These cantilevers were constructed of solder and therefore experienced very little elastic motion before the onset of plastic deformation. It was therefore hypothesized that a SDOF rigid-plastic model might produce a good approximation of the motion of the impulsively loaded cantilevers. The SDOF equation describes the angular deformation of the cantilever

as a function of time and it is the most elementary of assumed responses of a blast loaded cantilever. This equation was integrated by using a fourth order Runga-Kutta scheme, and updating all the variables such as air velocity, air density, drag coefficient etc at each time increment. The results are plotted in figure 5.1 with the experimental results. The agreement is good for the entire range of Mach numbers used, but this may in part be due to canceling of opposing effects. For example, effects such as strain hardening may be taking place but because of the actual drag coefficient being possibly larger than the theoretical values the two errors may cancel. The rigid-plastic model should overestimate the deformation because it assumes that all the strains are concentrated at one point, the plastic hinge at the base, and are not distributed throughout a region near the base, as in the case of the actual cantilever.

Cantilevers made of aluminum 4043 and 5056 with lengths of 99.2 mm (3.9 in) and diameters of 1.55 mm (0.06 in) were also tested in the shock tube. These experiments were to determine if the SDOF rigid-plastic model could be used to predict the final angles of the shock wave loaded cantilevers made of materials which have a more extensive elastic response than solder. Figure 5.2 is a plot of the final angles of rotation for cantilevers made of aluminum 5056 and of 4043 as a function of shock wave Mach number. This figure also shows the theoretical permanent rotation angles obtained by using the rigid-plastic SDOF model. The observed permanent deformations for both types of aluminum were significantly less than the predicted responses obtained from the solution of equation 3.13.

Although the simplified rigid-plastic model overestimates the amount of deformation that occurs when the aluminum cantilevers are dynamically loaded it does provide a first order approximation to the deformation. This solution may be used when it is necessary to identify if a given cantilever type structure will survive when blast loaded because if the model predicts survival then there is a high probability that it will.

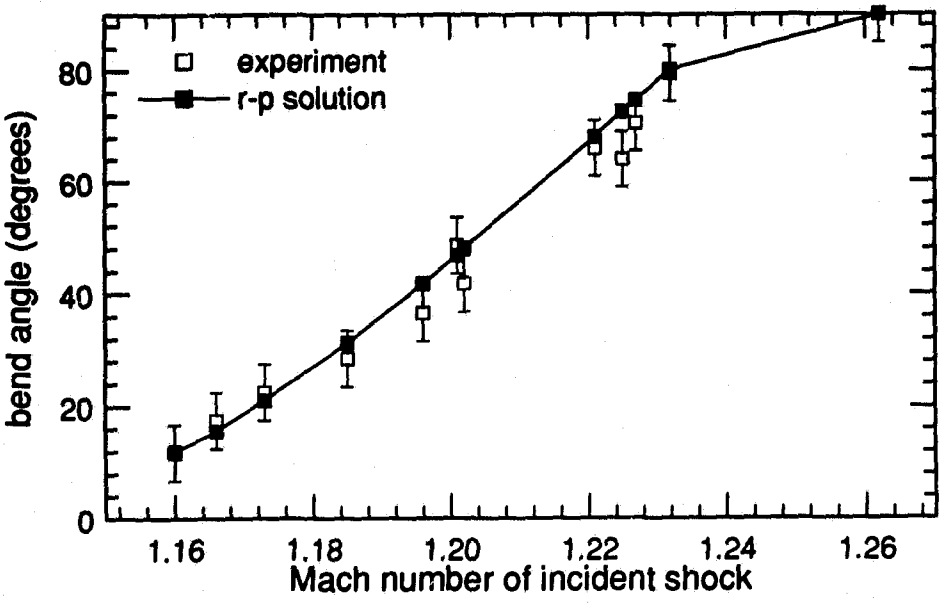

Figure 5.1: Comparison between the rigid-plastic solution and experimental results for 5.08 cm long, 1 mm diameter solder wires subjected to shock tube flows.

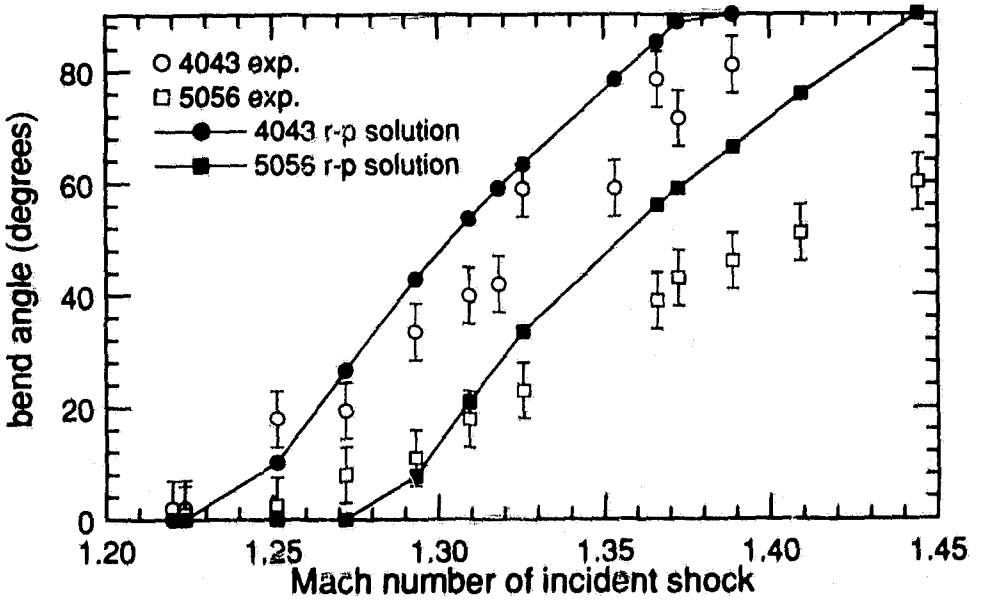

Figure 5.2: Comparison between the rigid-plastic solution and experimental results for aluminum 4043 and 5056 cantilevers 10 cm long, 1.55 mm diameter subjected to a shock tube flow.

A typical time resolved solution of equation 3.13 for a 5.1 cm (2.0 in) solder cantilever is given in figure 5.3. This figure shows plots of the deformation angle and dynamic pressure of the blast wave as a function of time. The wire begins to bend immediately after the passage of the shock and continues to bend until all the kinetic energy gained in the early stages of the loading process has been dissipated.

5.1.2 Evaluation of the elastic-plastic model

The elastic-plastic approach described in section 3.4.3 attempts to improve the predictions of the final deflection angle of cantilevers made of metals other than solder by introducing elasticity, strain hardening and strain-rate hardening in the deformation process.

Figure 5.4 displays plots of bend angle vs shock wave Mach number for cantilevers whose lengths were 99.2 mm (3.9 in) made of both types of aluminum. For a given Mach number it can be seen that the cantilevers constructed from aluminum 4043 deform appreciably more then those constructed from aluminum 5056, showing a significant difference in the material properties for the two aluminums. The solid lines show deformation angles predicted by the elastic-plastic model. This run of the model discretized the cantilever into 5 elements of equal length, each approximated by a point mass at the center of the element. The model predicts the response of these cantilevers very well. The solution however is sensitive to the strain-rate and strain hardening terms which were based on the values given by Manjoine(1944) and Parkes(1958).

Figure 5.5 shows the final deflection angles for cantilevers with different lengths made of aluminum 4043 and exposed to the loading of shock waves with the same Mach number of 1.22. The model predicts slightly larger deformation angles than the angles measured in the experiment for this particular Mach number, however the curves are parallel with a mean difference of 3°. It is concluded that the elastic-plastic model developed in 3.4.3 predicts the final angles of deformation of the aluminum

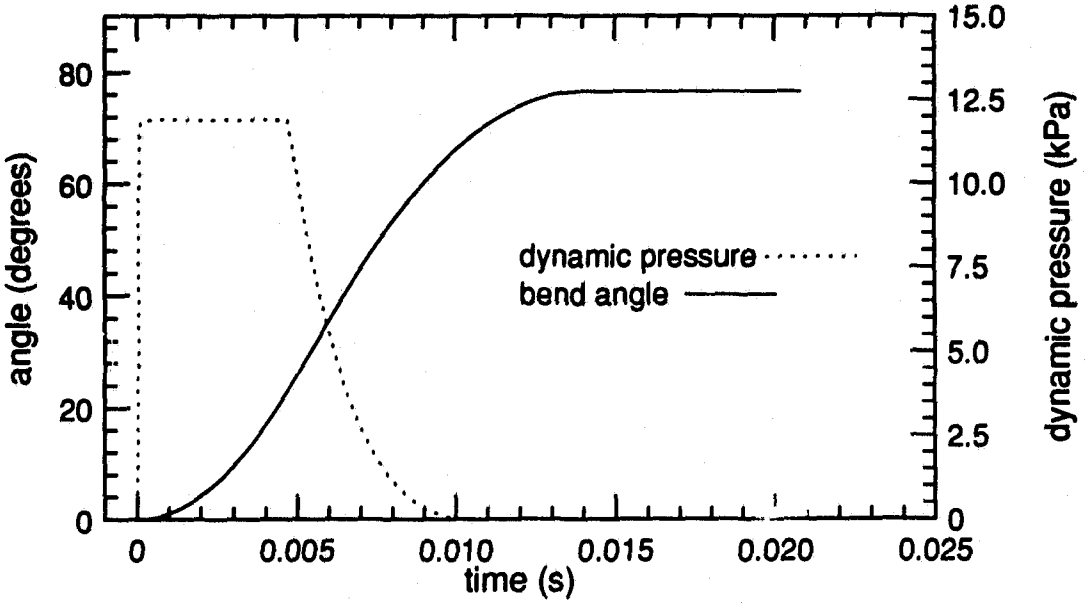

Figure 5.3: The deformation(equation 3.3) and dynamic pressure time histories for a 5.08 cm long, 1 mm diameter solder cantilever subjected to a shock tube flow.

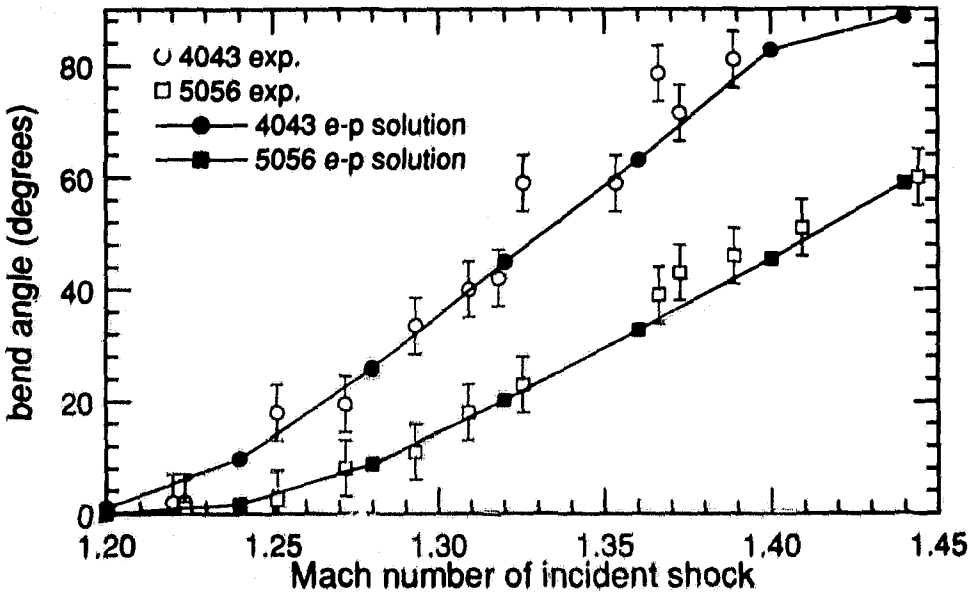

Figure 5.4: Comparison between the elastic-plastic solution and experimental results for aluminum 4043 and 5056 cantilevers 10.0 cm long and 1.55 mm diameter subjected to shock tube flows.

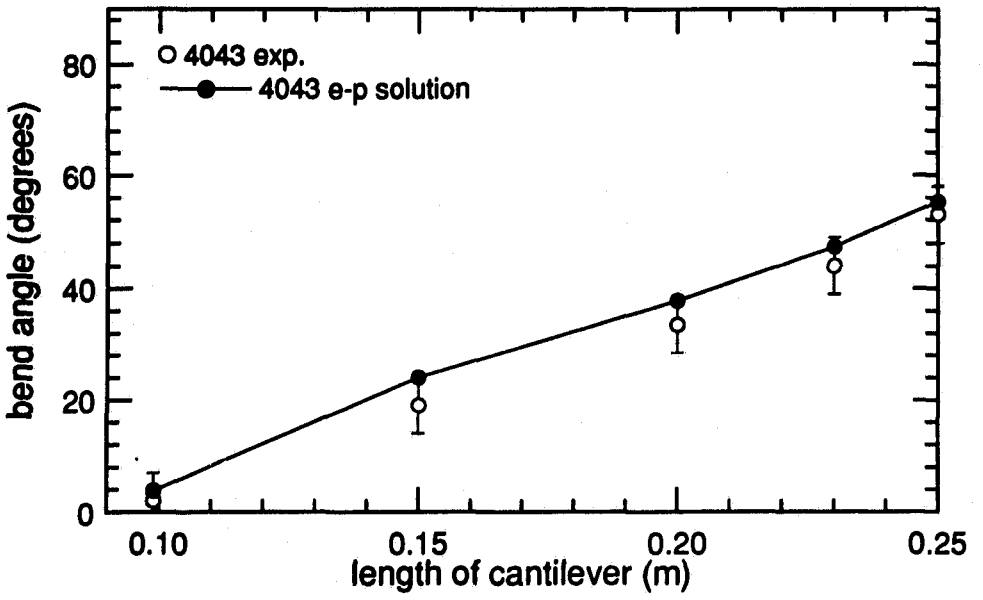

Figure 5.5: The variation of deformation angle with cantilever length for an incident shock Mach number of 1.22. The line is generated by the elastic-plastic model and the clear circles are the experimental results.

cantilevers to a much higher degree of accuracy then the simple rigid-plastic model.

5.1.3 High speed photographic measurements

Further experiments were carried out to provide information about the dynamic deformation of the cantilevers during the shock wave loading process. High speed photography was used to record the motion of cantilevers of four different lengths made from aluminum 4043. The relevant experimental conditions are given in table 4.2 and the experimental procedures are described in 4.2.2.

A 1 cm rectangular grid was seen in each frame of the high speed film and provided a scale in the field of view so that the image in each frame could be accurately digitized using an x-y digitizer. It was estimated that the average error in digitizing a specific position in the field of view was approximately 1.0 mm. Figures 5.6 to 5.9 show the digitized images of the cantilevers in the four experiments and the

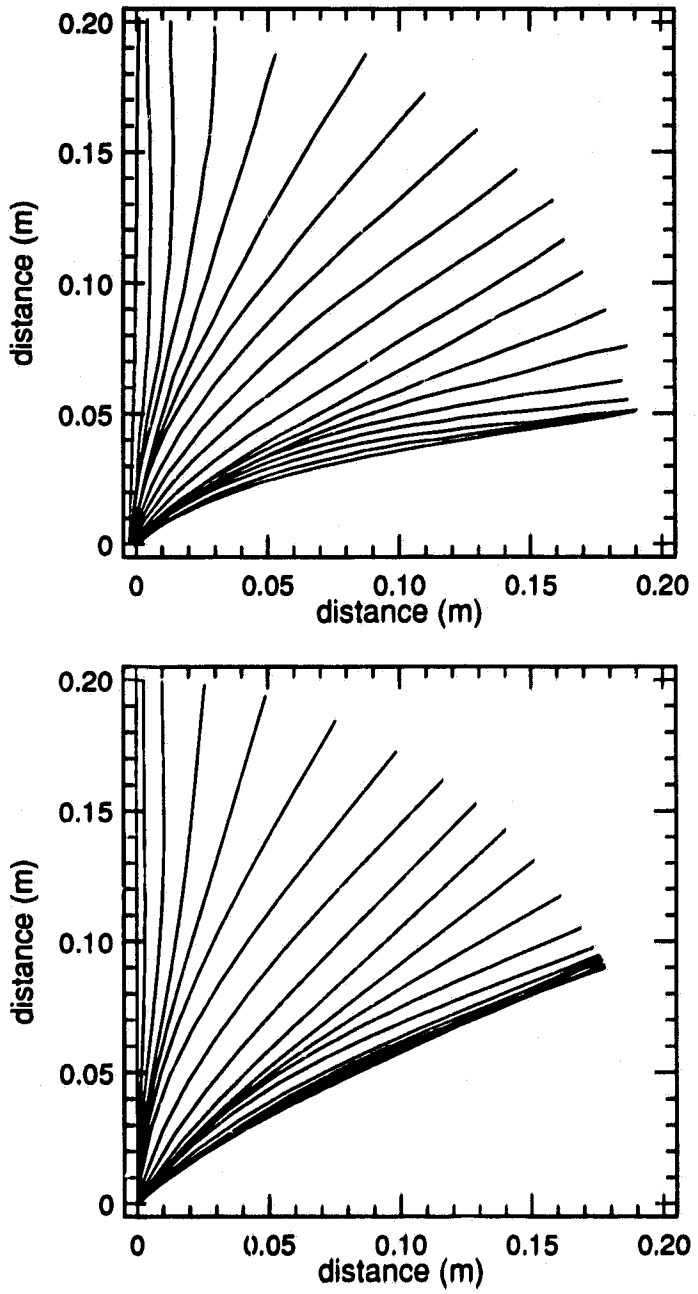

Figure 5.6: Experimental(top) and theoretical(bottom) deformation of a 0.2 m long, 1.55 mm diameter aluminum cantilever in a shock tube flow induced by a incident shock wave of Mach number 1.23. The theoretical deformation was generated by the elastic-plastic model. The time between adjacent images is approximately 1 ms.

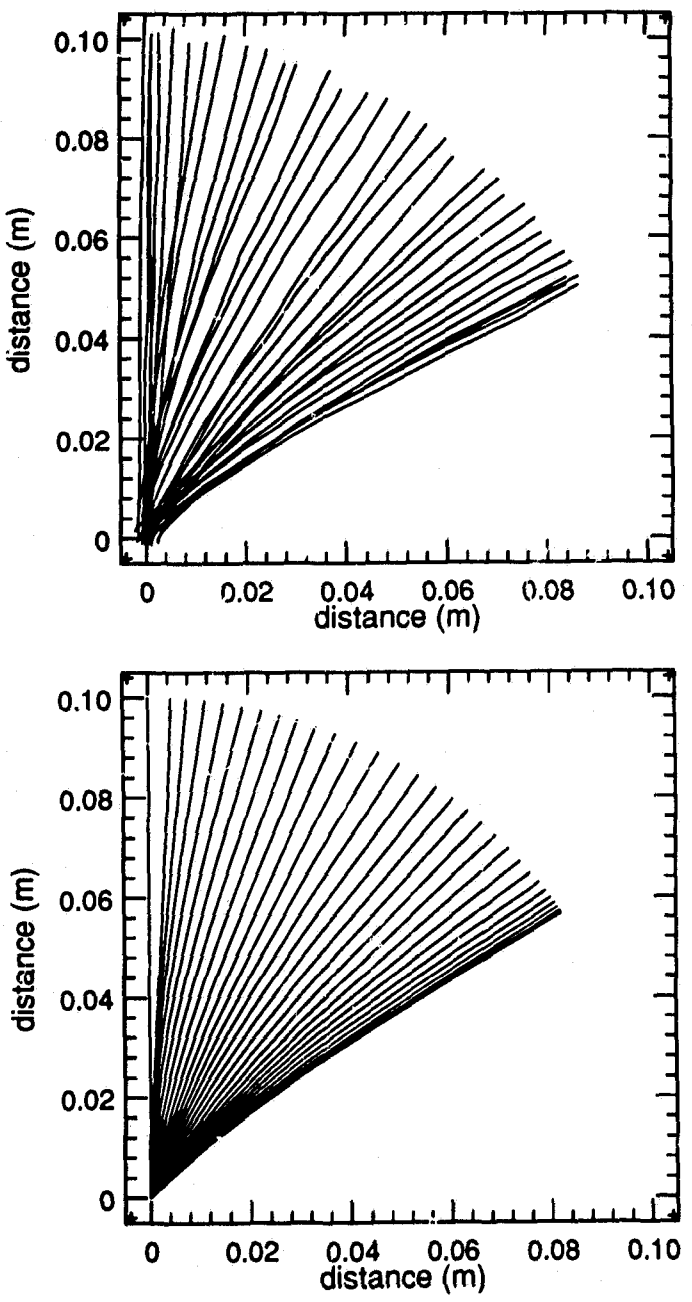

Figure 5.7: Experimental(top) and theoretical(bottom) deformation of a 0.1 m long, 1.55 mm diameter aluminum cantilever in a shock tube flow induced by a incident shock wave of Mach number 1.32. The theoretical deformation was generated by the elastic-plastic model. The time between adjacent images is approximately 0.2 ms.

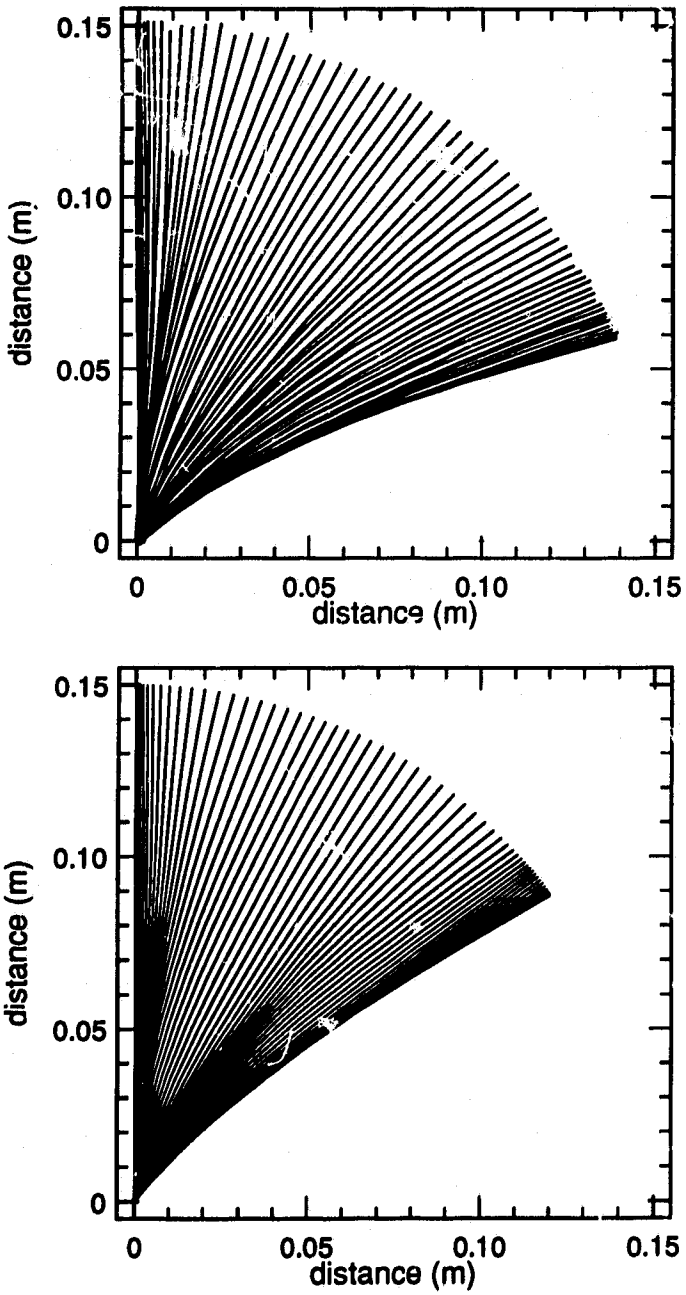

Figure 5.8: Experimental(top) and theoretical(bottom) deformation of a 0.15 m long, 1.55 mm diameter aluminum cantilever in a shock tube flow induced by a incident shock wave of Mach number 1.24. The theoretical deformation was generated by the elastic-plastic model. The time between adjacent images is approximately 0.2 ms.

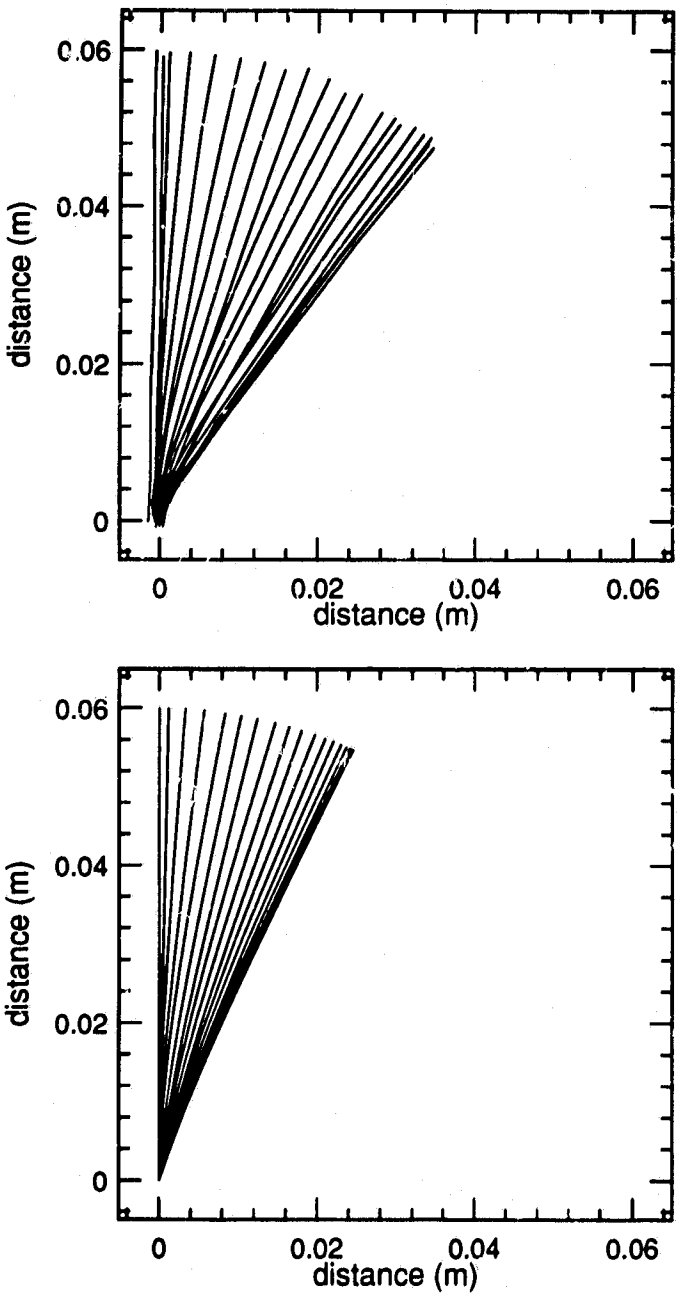

Figure 5.9: Experimental(top) and theoretical(bottom) deformation of a 0.06 m long, 1.55 mm diameter aluminum cantilever in a shock tube flow induced by a incident shock wave of Mach number 1.40. The theoretical deformation was generated by the elastic-plastic model. The time between adjacent images is approximately 0.2 ms.

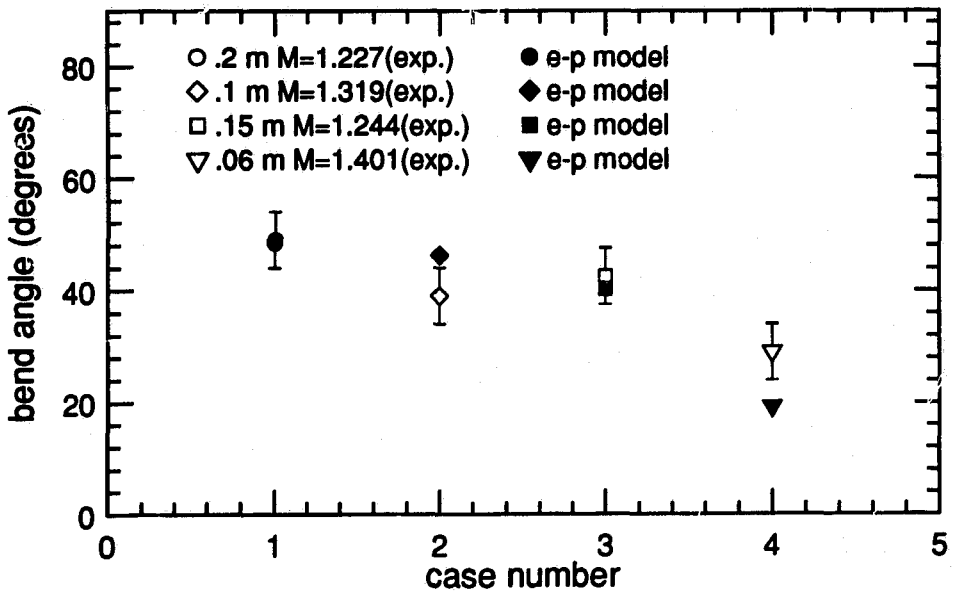

Figure 5.10: Final angle comparisons between that predicted by the e-p model and experiment for the high speed film experiments.

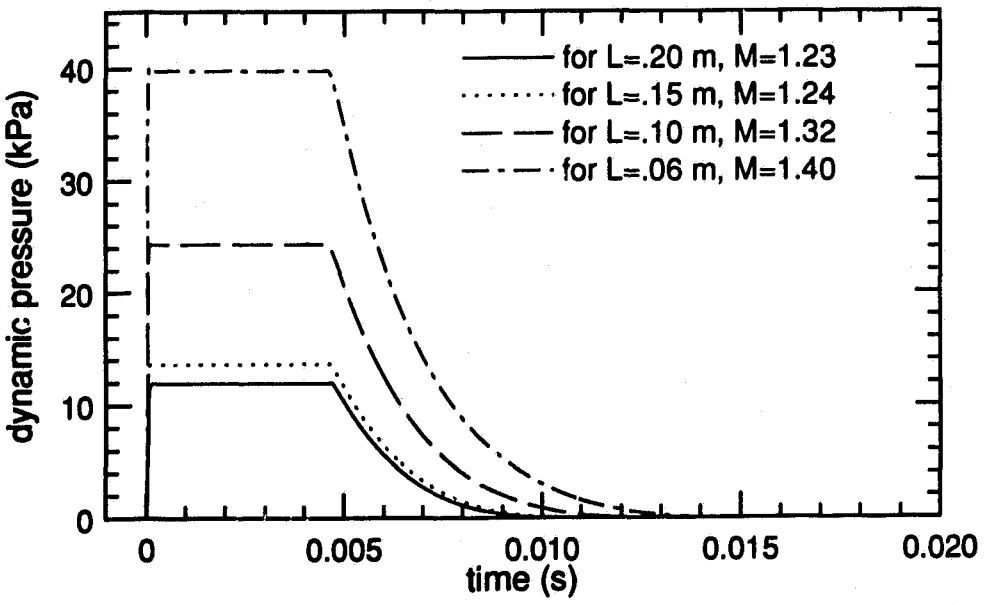

Figure 5.11: The dynamic pressure time histories for the high speed film experiments of the four different length(L) cantilevers generated by the FCT shock tube model.

shapes predicted by the elastic-plastic model described in 3.4.3 at the corresponding times. The images have been displayed up to the time when the maximum elastic and plastic displacement had occurred. After that time the cantilever began to reverse its motion and oscillate about the equilibrium plastic deformation angle. The permanent deformation angles as determined by experiment and by the numerical simulation for the four sets of conditions are plotted in figure 5.10. The dynamic pressure time histories used to load the four cantilevers generated by the FCT shock tube model are given in figure 5.11 for each high speed photographic experiment.

The bending profiles displayed in figures 5.6 to 5.9 show good qualitative agreement between the observed and calculated deformations but the numerical simulation appears to slightly underestimate the elastic displacement. This is probably due to the algorithm which updates the stiffness matrix, since this matrix is generated by forcing the distance to each node to remain constant in a non-conservative fashion. This effectively shortens the lever arm as the displacement of each node is increased, causing the cantilever to appear "stiffer". This effect would be significantly reduced if a two-dimensional large-deflection elastic simulation had been used to drive the plastic deformation portion of the simulation.

Figures 5.12 to 5.15 show the plastic deformation angle and angular velocity of the four cantilevers as functions of time. The numerical model predicts a non-constant deformation rate which oscillates. A similar plot of of angular deformation with time could not be derived from the photographic records of the cantilevers because it was very difficult to determine the plastic deformation angle at the base of the cantilever from the digitized data. Experimental oscillations in the deforming rates can be seen however by viewing the spacing between adjacent profiles, and is most easily seen in the time varying bending profiles plotted in figure 5.8. In this figure the distance which separates the adjacent cantilever profiles in both the experimental and theoretical plots changes with time, especially near the base. These higher modes are generated by the elastic vibrations induced during the loading of the cantilever.

The magnitude of the higher mode elastic vibrations decreases when the cantilever length is reduced. It is clear that the amount of plastic deformation is also a function of the elastic properties of the material and not just of the yield stress.

After being loaded by the shock waves, all the cantilevers in these experiments were straight except in the region close to the base where plastic deformation occurred. The high speed film showed that the cantilever is not straight during the deformation process but is curved due to its elastic nature. In some cases cantilevers were also observed to have plastic deformations in regions other than the base. This occurred when the length of the cantilever was increased to a length where the induced elastic vibrations were of such magnitude as to produce bending moments larger than the material could withstand. For cantilevers where this effect occurs a model based on a premise that a single plastic hinge exists at the fixed end would be insufficient to describe the response during dynamic loading. An example of this effect is shown in figure 5.16. The model can be used to predict the length of the cantilever for which this mode of failure is possible, and thus the limiting length for a cantilever with a specific cross-section and material properties.

5.1.4 Brittle cantilevers

Brittle cantilever were exposed in the shock tube to calibrate the cantilever gauges that were used at the MINOR UNCLE experiment. This was required since it was determined that equation 3.35 overestimated the peak dynamic pressure in most cases when a drag coefficient of 1.2 was used. The resulting calibration curve of peak dynamic pressure vs length of cantilever is given in figure 4.5. The upper line indicates, for a given length, the lowest peak dynamic pressure required to break a 0.5 mm graphite cantilever and the lower line indicates the highest peak dynamic pressure that does not break the cantilever. In other words the actual peak dynamic pressure required to break a given cantilever lies somewhere between these two curves.

The most significant feature of this curve is the slight increase in the required

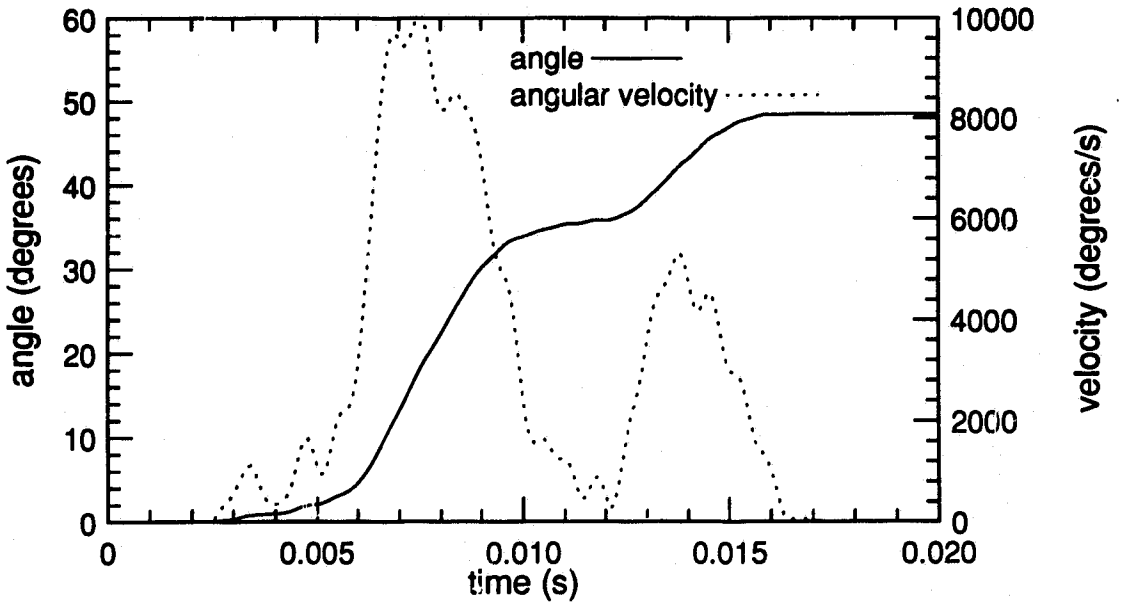

Figure 5.12: Bending and angular velocity time histories for the 0.2 m long, 1.55 mm diameter aluminum cantilever subjected to the flow shown in figure 5.11.

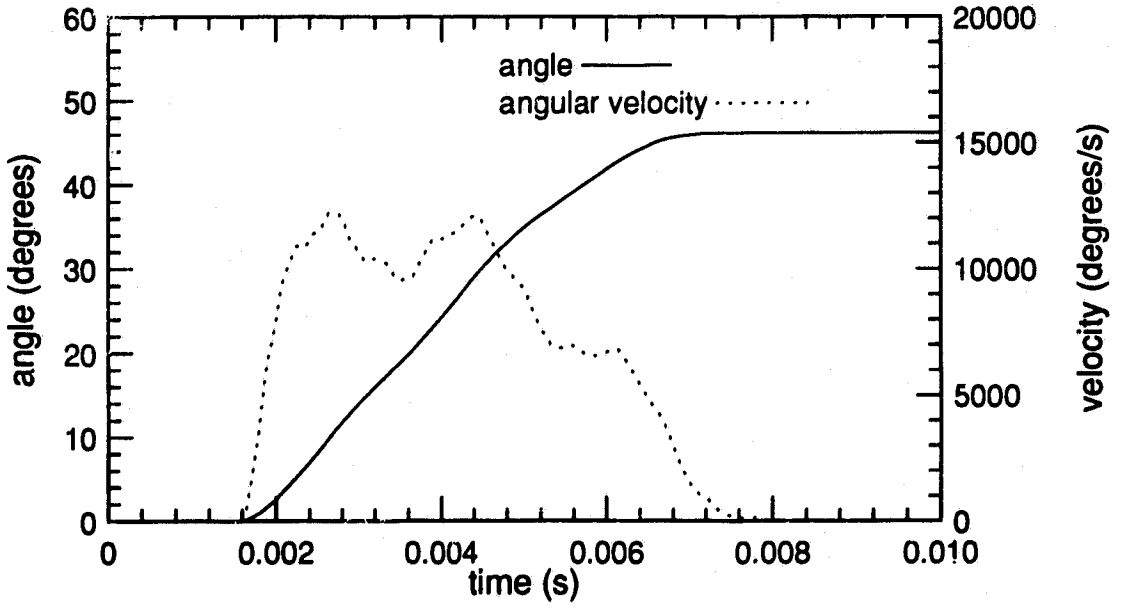

Figure 5.13: Bending and angular velocity time histories for the 0.1 m long, 1.55 mm diameter aluminum cantilever subjected to the flow shown in figure 5.11.

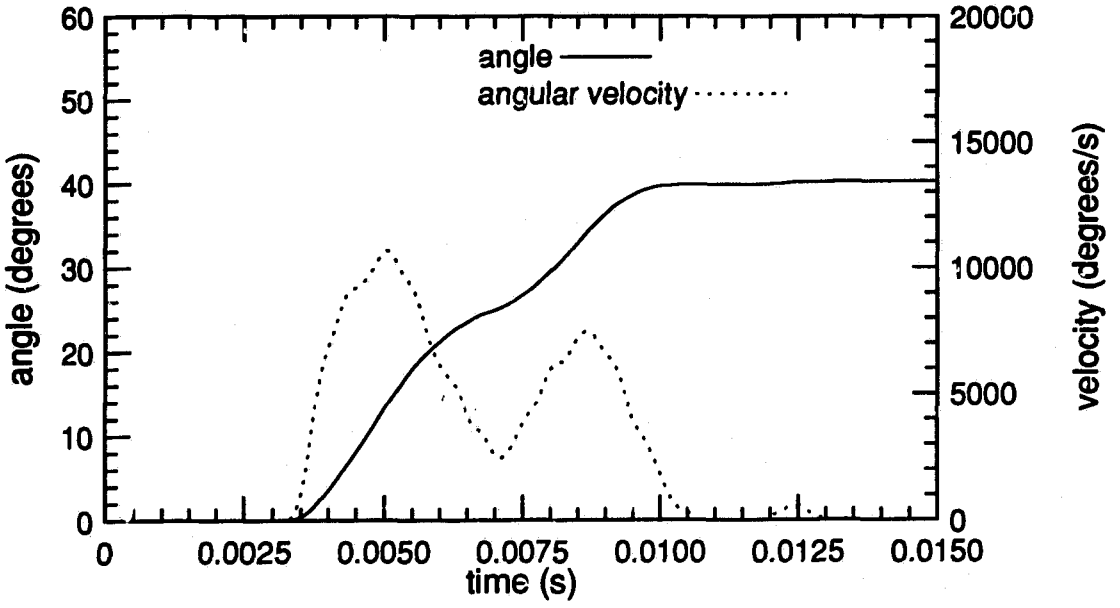

Figure 5.14: Bending and angular velocity time histories for the 0.15 m long, 1.55 mm diameter aluminum cantilever subjected to the flow shown in figure 5.11.

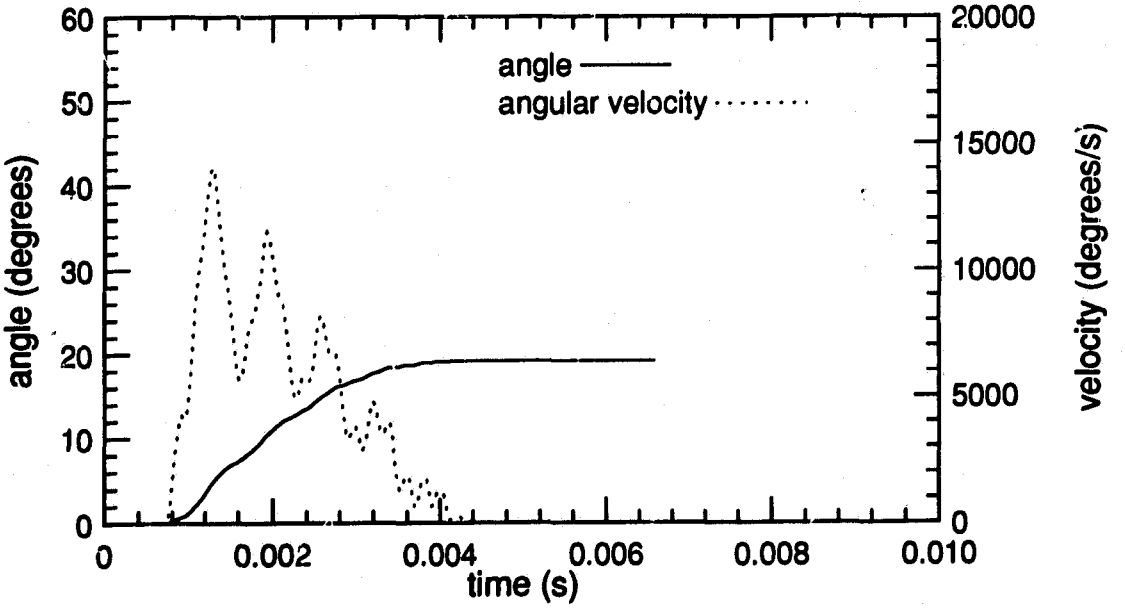

Figure 5.15: Bending and angular velocity time histories for the 0.06 m long, 1.55 mm diameter aluminum cantilever subjected to the flow shown in figure 5.11.

Figure 5.16: Photographs of deformed aluminum 4043 cantilevers of diameter 1.55 mm subjected to a shock tube flow, incident shock Mach number 1.2. left: length 0.2 m, right: length 0.25 m. A straight line is drawn from the plastic hinge at an the plastic deformed angle to show the curvature of the rods. The 0.2 m cantilever is essentially straight throughout and the 0.25 m cantilever is not.

pressure to break the cantilever when the cantilever length is increased at around the length of 0.04 m. Repeated experiments have shown that graphite cantilevers slightly longer then 0.04 m have in most cases a higher or equal peak dynamic pressure breaking threshold than cantilevers slightly shorter. This goes against intuition since in most cases a longer cantilever made of the same material and same diameter will have a lower peak dynamic pressure breaking threshold than a shorter cantilever because the lever arm is longer. This contradiction most likely arises because the physics of the situation changes with an increase in length from 0.04 to 0.046. Table 5.1 below shows the natural periods of these two cantilevers.

Table 5.1: Natural periods of graphite rods.

Length (m)	Period (ms)	1/4 period (ms)	Positive phase (ms)
0.040	29.3	7.3	9.2
0.046	38.7	9.7	9.1

The 0.04 m long cantilever has a 1/4 natural period that is less than the positive phase duration of the shock tube flow while for the 0.046 m cantilever the 1/4 natural period is greater than the positive phase of the shock tube flow. The conclusion is that if 1/4 of the natural period of the structure is less than the length of time of the applied force then the structural damage can be assumed to be peak dynamic pressure sensitive and when it is greater it becomes impulse sensitive.

The results of this calibration were also used to obtain the effective drag coefficients for the various cantilevers, using equation 3.35. The results are plotted in figure 5.17 as effective drag coefficient vs length of cantilever. A cantilever with a length less than about 0.04 m has an effective C_d that is approximately 1.72 and for a cantilever longer than 0.04 it is about 1.34. If the steady state drag coefficient data are used with the Reynolds number and Mach number of the flow, the drag coefficient should be about 1.2 for all these cantilevers. The jump in C_d from 1.34 to

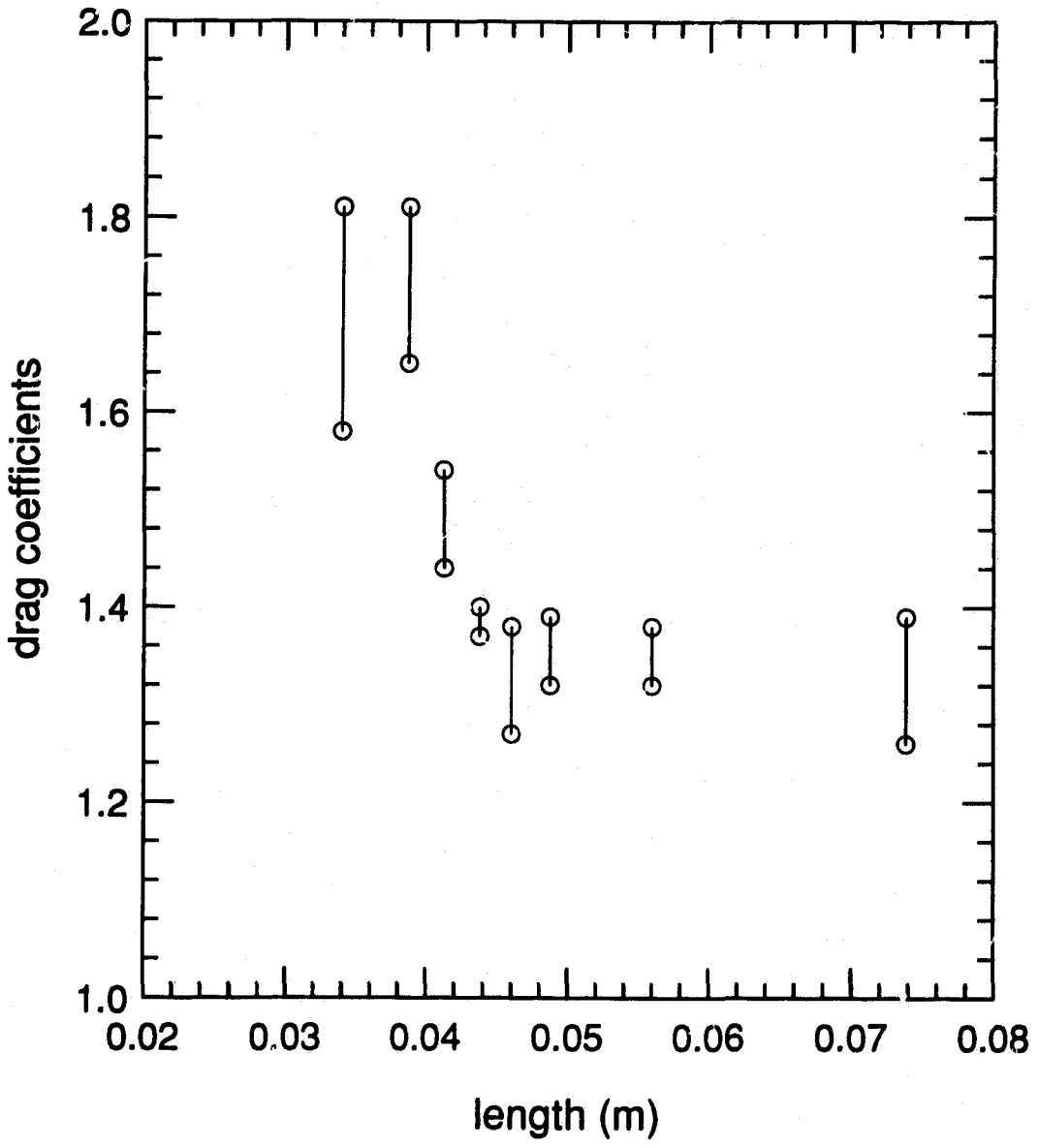

Figure 5.17: Effective drag coefficient versus length for brittle cantilevers, calculated using shock tube experimental data.

1.72 is mainly caused by the effect described above where the shorter cantilever are more sensitive to the peak dynamic pressure and the longer cantilevers are more to the impulse. The difference between both of these C_d values and the steady values is most likely because equation 3.35 is only an approximate equation which does not include such effects as elasticity. Another explanation for the apparent increase in C_d above the steady state value may be the contribution of the diffraction phase. It takes the incident shock wave approximately 1.5 μs to travel a distance equal to the diameter of the cantilever. During that time, and for some time after, the force can much as 10 times greater than that which occurs in drag loading regime. This effect, although short in duration, will increase the effective drag coefficient for cantilevers whose response times are very short. Because of this uncertainty about the drag coefficient and simplifying assumption in the model, equation 3.35 is of limited value for predicting the response of brittle cantilevers to shock wave loading. On the other hand, it is a relatively simple procedure to calibrate these cantilevers in a shock tube, as described above.

5.2 High explosive tests

DISTANT IMAGE was the first of two experiments used to evaluate the effectiveness of the numerical models in predicting the response of cantilevers to blast wave loading. 404 cantilevers were used at this event, and 437 cantilevers were used in the second experiment, code named MINOR UNCLE two years later. The results obtained from these experiments are given in the following sections.

The final deformation angles of all ductile cantilevers at both DISTANT IMAGE and MINOR UNCLE are given in appendices A and B. A post-test photograph of a deformed 1.6 m long cantilever at a distance of 283 m from the MINOR UNCLE explosion is shown in figure 5.18.

5.2.1 Solder cantilevers

As shown in section 5.1.1 the rigid-plastic(R-P) model gave a reasonable prediction of the response of solder cantilevers subjected to a shock tube f[illegible]. The R-P model was also used to predict the response of the solder cantilevers at both HE events. Figures 5.19 and 5.20 show the experimental and predicted final angles of deformation for two types of the solder cantilevers. The lengths of these cantilevers were 0.04 m and 0.07 m. The agreement between the theoretical response derived from the rigid-plastic model and the experiment is relatively good.

The DISTANT IMAGE explosion was slightly larger than MINOR UNCLE, the ratio of charge weights was 1.09, which corresponds to a scaled difference in distance of about 3 %. The rigid-plastic model predicts a difference in angle, for the solder cantilevers, between DISTANT IMAGE and MINOR UNCLE of about 5° to 10° with this ratio of charge weights. The uncertainty of each measurement is ± 5° and is within the expected theoretical difference. It is perhaps unreasonable to expect significantly better agreement than this, taking into consideration local variations in the blast wave, and particularly the effects of such phenomena as dust pickup.

5.2.2 Aluminum and steel cantilevers

Figure 5.21 shows the deformation angle versus distance from the MINOR UNCLE explosion for 0.15 m long cantilevers constructed of aluminum 4043. The results of all the other ductile cantilevers that were at multiple distances from GZ for both DISTANT IMAGE and MINOR UNCLE are given in in figures C.1 to C.19. The theoretical deflections predicted by the elastic-plastic(e-p) model are plotted as the solid line and the experimental data are plotted as the squares. In some cases the theory overestimates the final angles of deformation and in other instances it underestimates the final angles. The best agreement occurs with the cantilevers made of the same materials that were used in the shock tube experiments those being

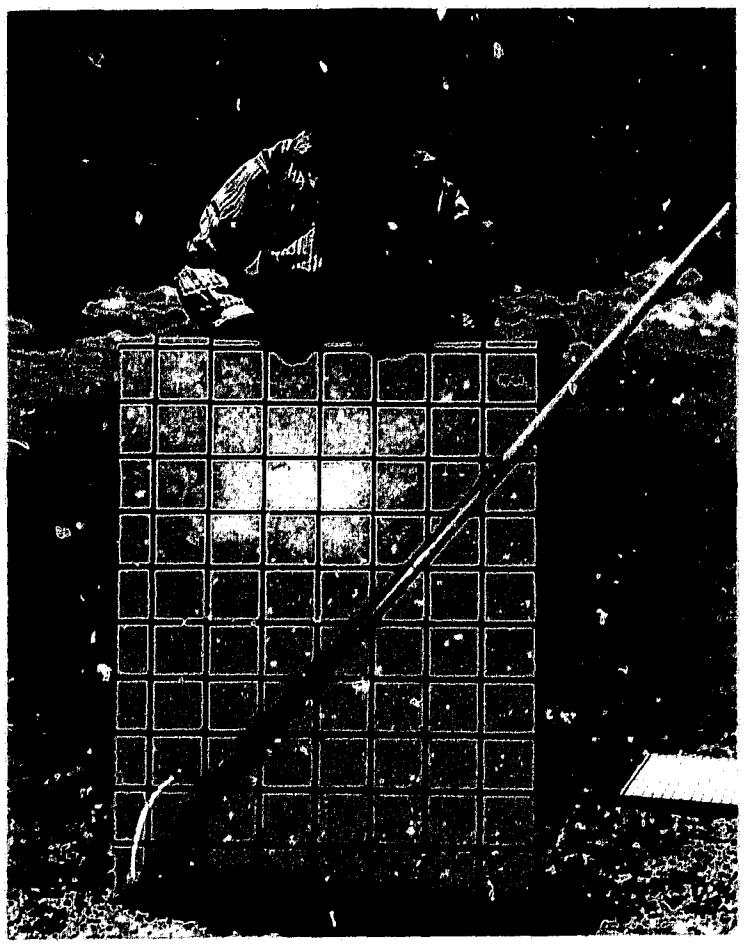

Figure 5.18: Deformed 1.6 m long, 2.54 cm diameter aluminum 6061 cantilever at a distance of 283 m from the MINOR UNCLE explosion, showing that the majority of the bending occured at the base.

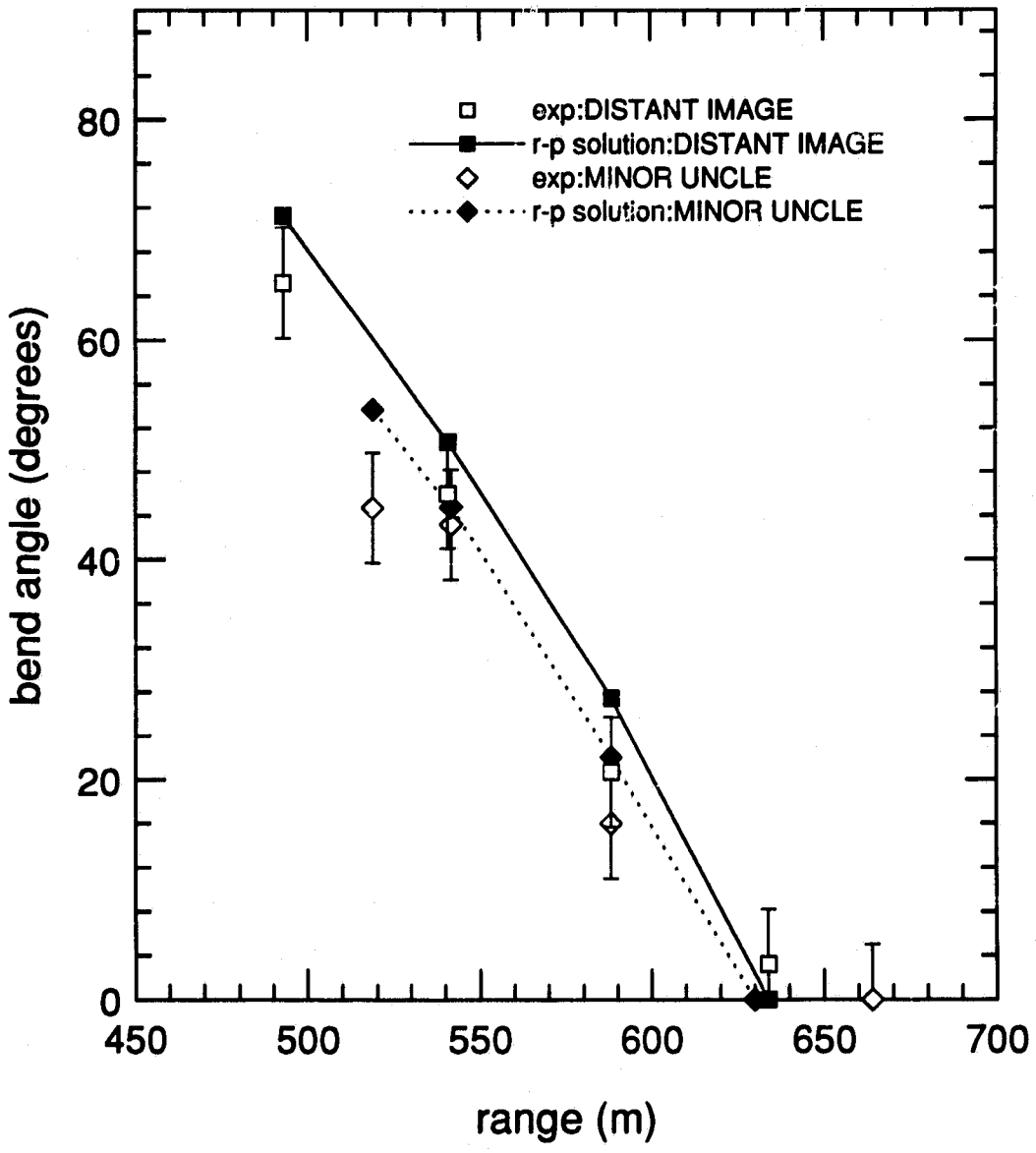

Figure 5.19: The deformation versus range for 0.04 m long, 1 mm diameter solder cantilevers at DISTANT IMAGE and MINOR UNCLE. The theoretical values were generated by the rigid-plastic model.

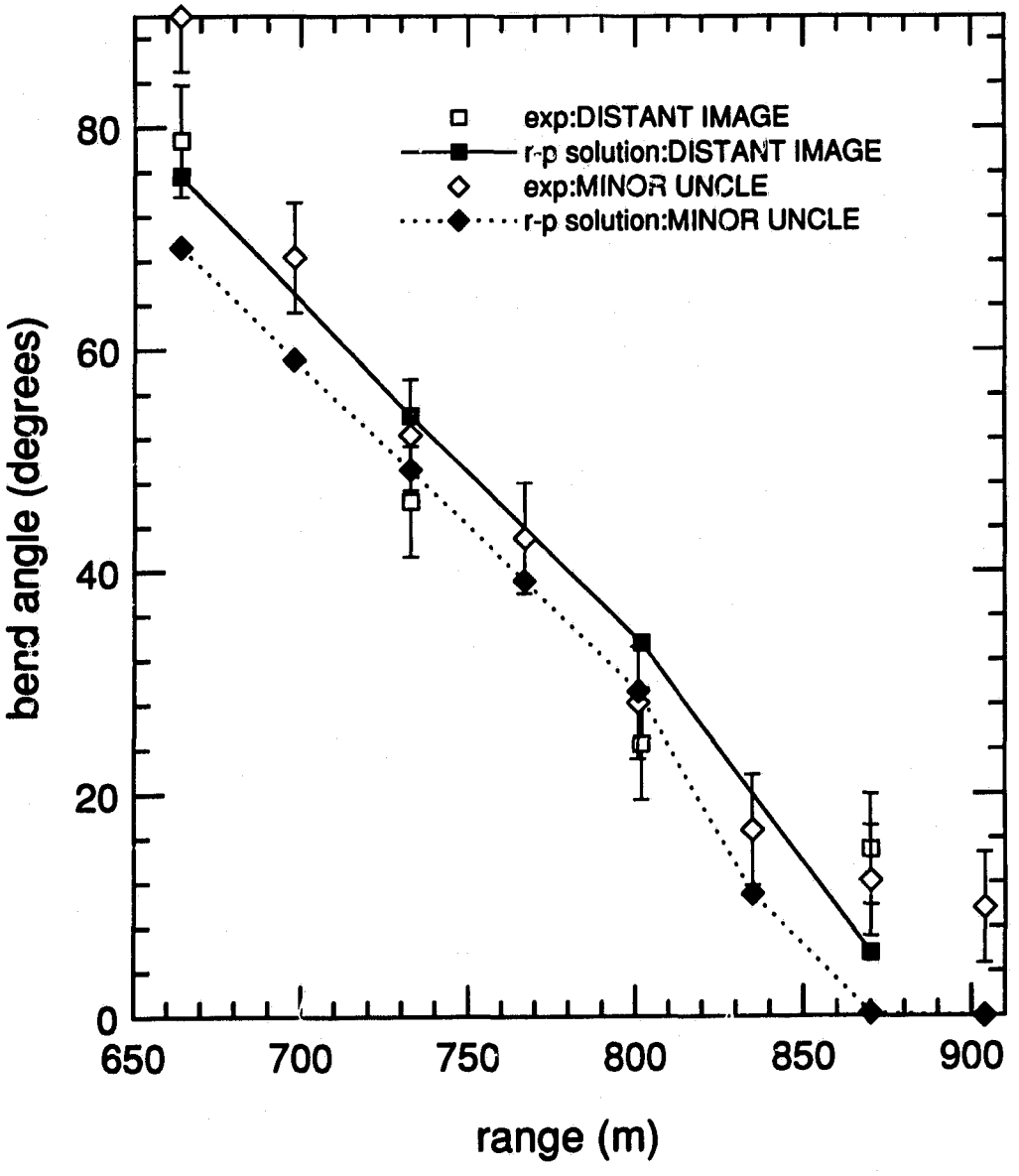

Figure 5.20: The deformation versus range for 0.07 m long, 1 mm diameter solder cantilevers at DISTANT IMAGE and MINOR UNCLE. The theoretical values were generated by the rigid-plastic model.

aluminum 4043 and 5056.

5.2.3 Factors affecting the variability of deformation

At many locations on the field experiments several identical cantilevers were used in order to provide a measure of the variability to be expected when a structure is exposed in the chaotic environment of a blast wave. The differences in deflection between identical cantilevers at similar distances at DISTANT IMAGE and MINOR UNCLE are plotted in figure 5.22. The standard deviation about the mean difference of + 3.4° is 10°. Also plotted in this figure is the 95% confidence interval which extends from .4 degrees to 6.3 degrees. This interval implies that if there was an infinite number of identical cantilevers at DISTANT IMAGE and MINOR UNCLE there would be a 95% probability that the average angular deformation difference would lie within the given range. It can therefore concluded that DISTANT IMAGE produced a slightly stronger blast wave then that which occurred at MINOR UNCLE.

It is suggested that most of the variability in the deformation of identical cantilevers at the same distances from the two explosions is due to local differences in blast wave properties, and the most likely cause for these differences is the amount of material entrained in the blast wave. This material is primarily dust and small stones. The mechanism for dust pick up and projection in a blast wave is not well known, and may be associated not only with the blast wave in the air but also the ground shock. Close to the charge the surface wave in the ground, which probably has the greatest effect on dust raising, lags behind the shockfront. As the shock front slows, due to its expansion in three dimensions, a point is reached where the speeds of the ground surface waves and the shock front are the same. At this time there is a maximum coupling between the two waves. The surface wave then outruns the shock and may be of sufficient amplitude to project dust into the air before the arrival of the shock.

The effect of the dust on dynamic pressure in a blast wave, and thus the loading

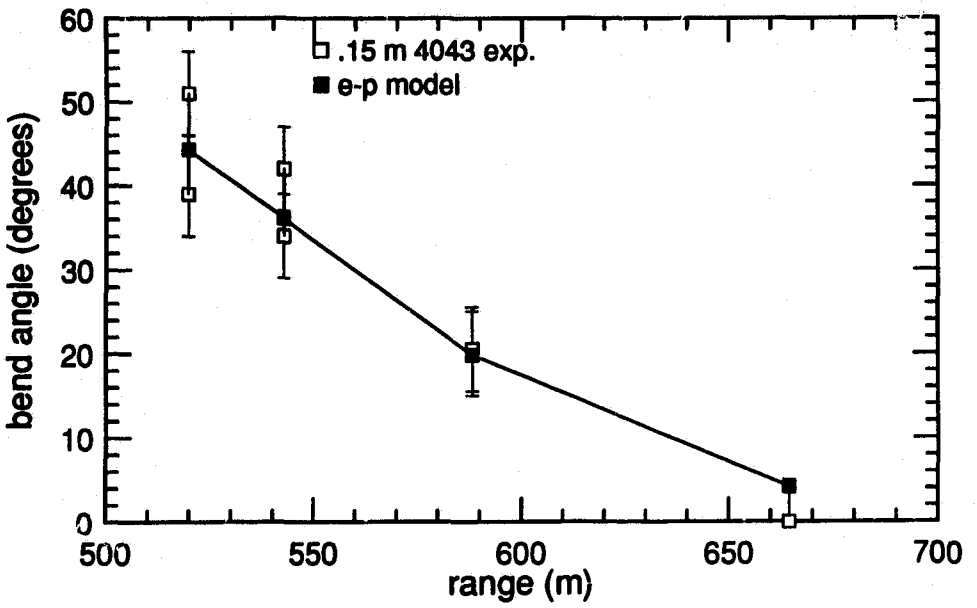

Figure 5.21: Experimental and theoretical deformation angle versus range for aluminum 4043 cantilevers .15 m long, 1.55 mm diameter at MINOR UNCLE.

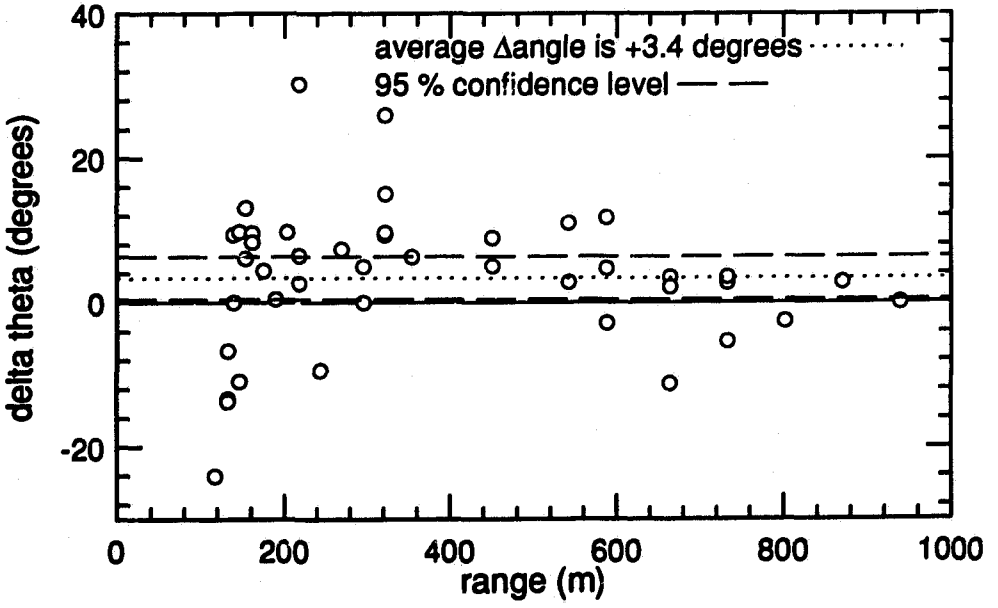

Figure 5.22: Cantilever deflection differences between identical cantilevers at similar distances from DISTANT IMAGE and MINOR UNCLE.

on a cantilever, is difficult to predict. When dust is first is first entrained energy is removed from the air and the dynamic pressure may decrease, and if a cantilever is primarily sensitive to peak dynamic pressure its deformation may be lower than predicted. Eventually the dust will reach the velocity of the air flow, increasing the dynamic pressure. As a result of its greater inertia the dust will maintain its momentum in a decaying blast wave and significantly increase the dynamic pressure. A cantilever with a slow response time which is sensitive to impulse rather than peak pressure will therefore experience a greater deformation. The magnitude of these effects changes rapidly with distance from the ground surface.

As a result of these factors, a standard deviation of 10° for the deformation of cantilevers is to be expected. The blast wave properties were obtained from ANFO.EXE and *AirBlast*, neither of which recognize any effects due to dust or other disturbances. Reviewing the results of the experimental measurements and the numerical predictions presented in appendix C the agreement between the predictions and the observations are reasonable for the cantilevers made of aluminum 4043 and 5056 and of steel 1018 throughout the range of sizes. The same order of agreement was not found for the cantilevers made of aluminum 6061.

5.2.4 Comparison of charge yields

At both DISTANT IMAGE and MINOR UNCLE there were also sets of identical cantilevers that were placed at a range of distances from the explosions but not necessarily at the same radial distances in the two experiments. The resulting angles of deformation for one of these sets are plotted vs distance in figure 5.23. These cantilevers were constructed from aluminum 4043 and were 1.55 mm (1/16 in) in diameter and 0.15 m (0.5 ft) long. It will be seen that the deflection angles at DISTANT IMAGE were larger than those at MINOR UNCLE, as expected. This particular type of cantilever responds in approximately 15 ms (based on the results from the elastic-plastic model and shown in figure 5.24), by which time the blast wave

has decayed by 5%. The positive phase of the blast wave at the range where the cantilevers were positioned was 446 ms. It is therefore assumed that peak dynamic pressure was the dominant factor in determining the final angle of deformation. The two explosions were very similar in size and hence have similar decay rates. The variation of peak dynamic pressure with distance at DISTANT IMAGE were obtained from *AirBlast* and were used with the data from figure 5.23 to develop the calibration curve shown in figure 5.25 of peak dynamic pressure versus angle of bend. A polynomial fit was made to the data and used to predict the peak dynamic pressure that had occurred at MINOR UNCLE based on the observed deformations. Eight other sets of similar cantilevers, for which this type of analysis could be applied, were used at both tests. The results of peak dynamic pressure versus range obtained for MINOR UNCLE from these cantilevers are plotted in figure 5.26, with the results from the electronic gauges, the MINOR UNCLE version of *AirBlast* and ANFO.EXE. The results based on the analysis of the cantilevers correlate well with those from the other techniques.

The variations of peak dynamic peak pressure as functions of distance, obtained from the cantilever measurements on the two experiments, were compared and used with the cube root scaling law (equation 2.14) to calculate the relative yields of the two explosives. This was done for a range of distances and the results are plotted in figure 5.27. The yield ratio is the ratio of energy yield of MINOR UNCLE to that of DISTANT IMAGE. In the region from 100 m to 400 m the fraction is less than one as expected however, from 400 m to 800 m the estimated yield appears to be approximately one. This effect is also observed in the results of the brittle cantilever gauges which will be discussed later. The average yield ratio based on the ductile cantilevers is 0.89 and the actual ratio of the charge masses was 0.92, probably an insignificant difference. The fact that the yield ratio appears to be a function of distance suggests that the DISTANT IMAGE explosion was not only larger than MINOR UNCLE, but also that the detonation was more "efficient". A

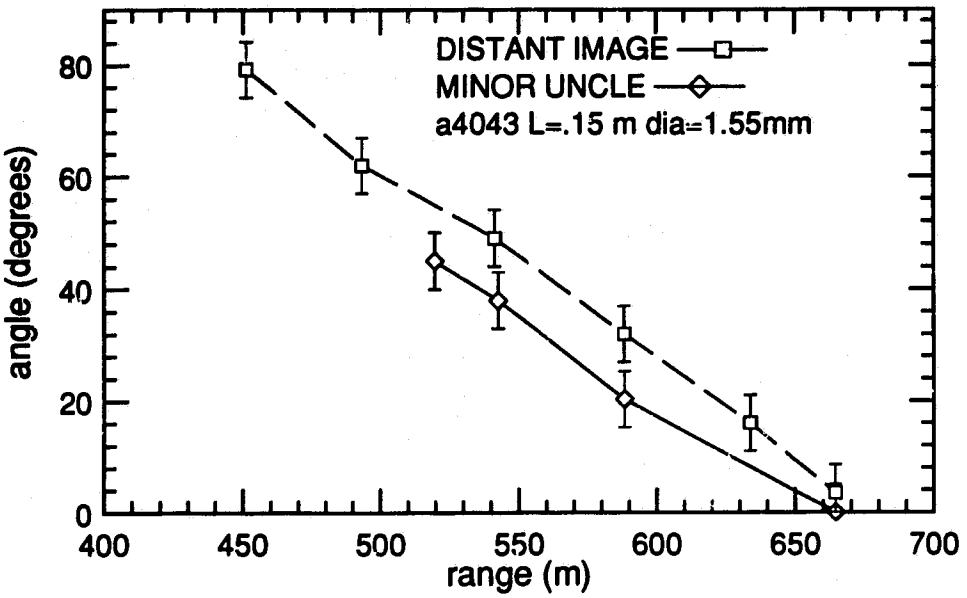

Figure 5.23: Comparison between deformation angles for 0.15 m long, 1.55 mm diameter aluminum 4043 cantilevers at both DISTANT IMAGE and MINOR UNCLE.

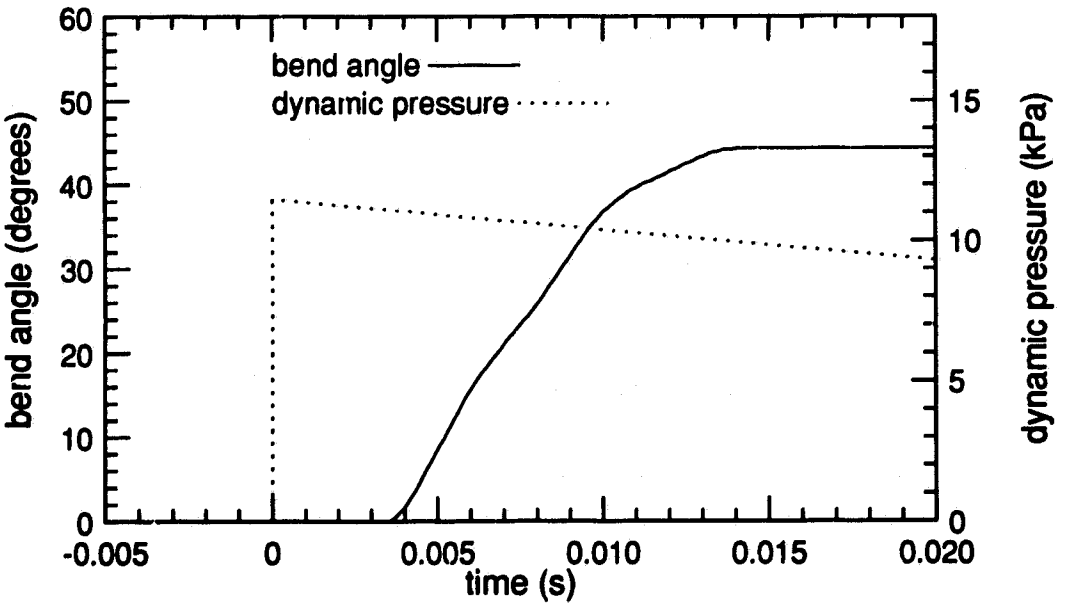

Figure 5.24: Deformation and dynamic pressure time histories for a 0.15 m long, 1.55 mm diameter aluminum 4043 cantilever 519.0 m from GZ at MINOR UNCLE.

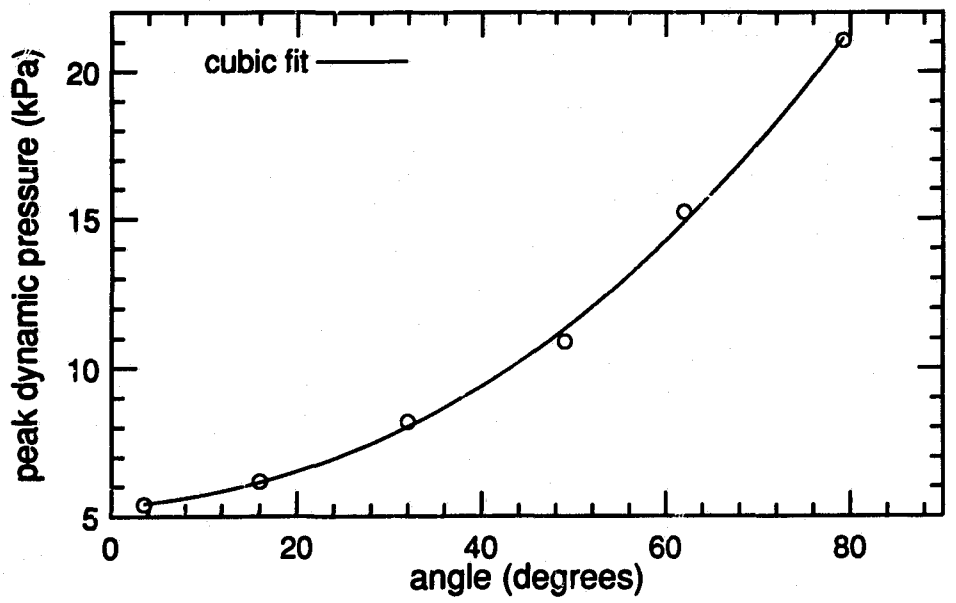

Figure 5.25: Calibration curve of peak dynamic pressure versus deformation angle for aluminum 4043 cantilevers .15 m long, 1.55 mm diameter

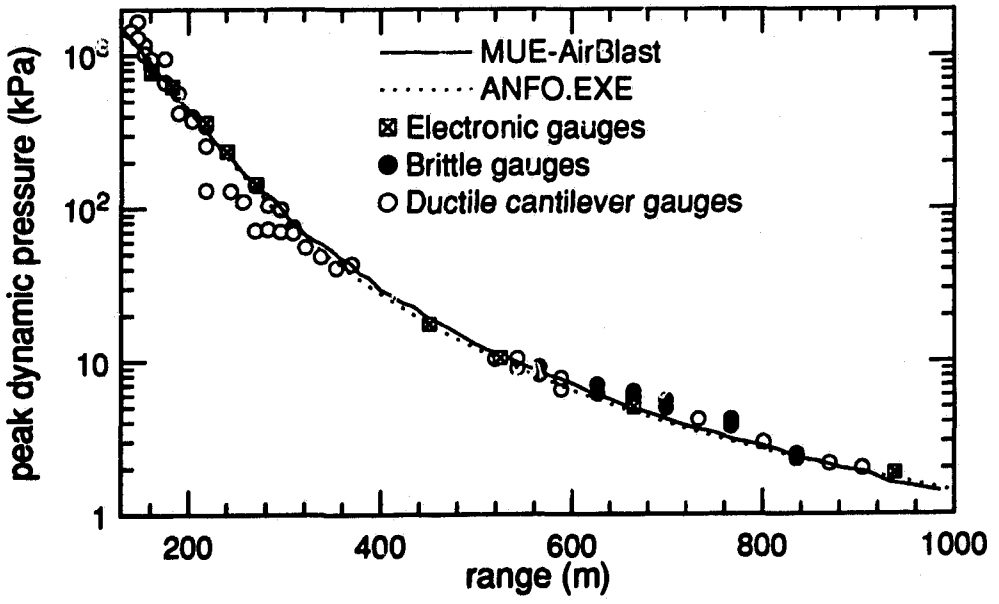

Figure 5.26: Peak dynamic pressure versus range for MINOR UNCLE obtained from the ductile and brittle cantilevers, electronic gauges *AirBlast* and ANFO.EXE.

more efficient detonation produces a relatively stronger shock closer to the charge, and thus for an equivalent energy release, a weaker shock front further from the charge. The cantilever measurements appear to have been sensitive enough to detect this difference between the two explosions. The detonation efficiency is dependent on such properties as packing of the explosive and the quality of the explosive.

5.2.5 Non-radial flow detection

By observing the relative angle between the plane of bending and the radial line extending from the cantilever to the charge center any non-radial flows can be detected. The orientation of all the cantilevers on DISTANT IMAGE and MINOR UNCLE was measured and no significant deviation from radial flow was detected.

5.2.6 Pressure-impulse diagrams

In section 3.2 the usefulness of a P-I diagram was discussed. Figure 5.28 shows a theoretical P-I diagram generated by the elastic-plastic model described in section 3.4.3. This diagram was created for a cantilever made from aluminum 4043 with a length of 0.15 m and diameter of 0.15 cm. The cantilever was theoretically loaded with blast waves with time resolved properties provided by *AirBlast*. This was done by creating hypothetical surface burst charges with sizes ranging from 0.2 kg to 1.0×10^8 kg TNT. For a given charge size distances were determined at which deformation angles of 0, 45, and 80 were produced by the elastic-plastic model. The peak dynamic pressures and impulses were determined at these distances. This was done for approximately 10 charge sizes. All the peak-pressure impulse combinations that produced a specific angle were subsequently joined to create the isodamge curve. Each of these lines give the required peak dynamic pressure impulse combinations that produce the specified damage, angle of deformation in this case. The similarity of these curves with those in the ideal P-I diagram given in figure 3.2 may be noted.

Also plotted in this figure is the experimental damage, for this cantilever, found

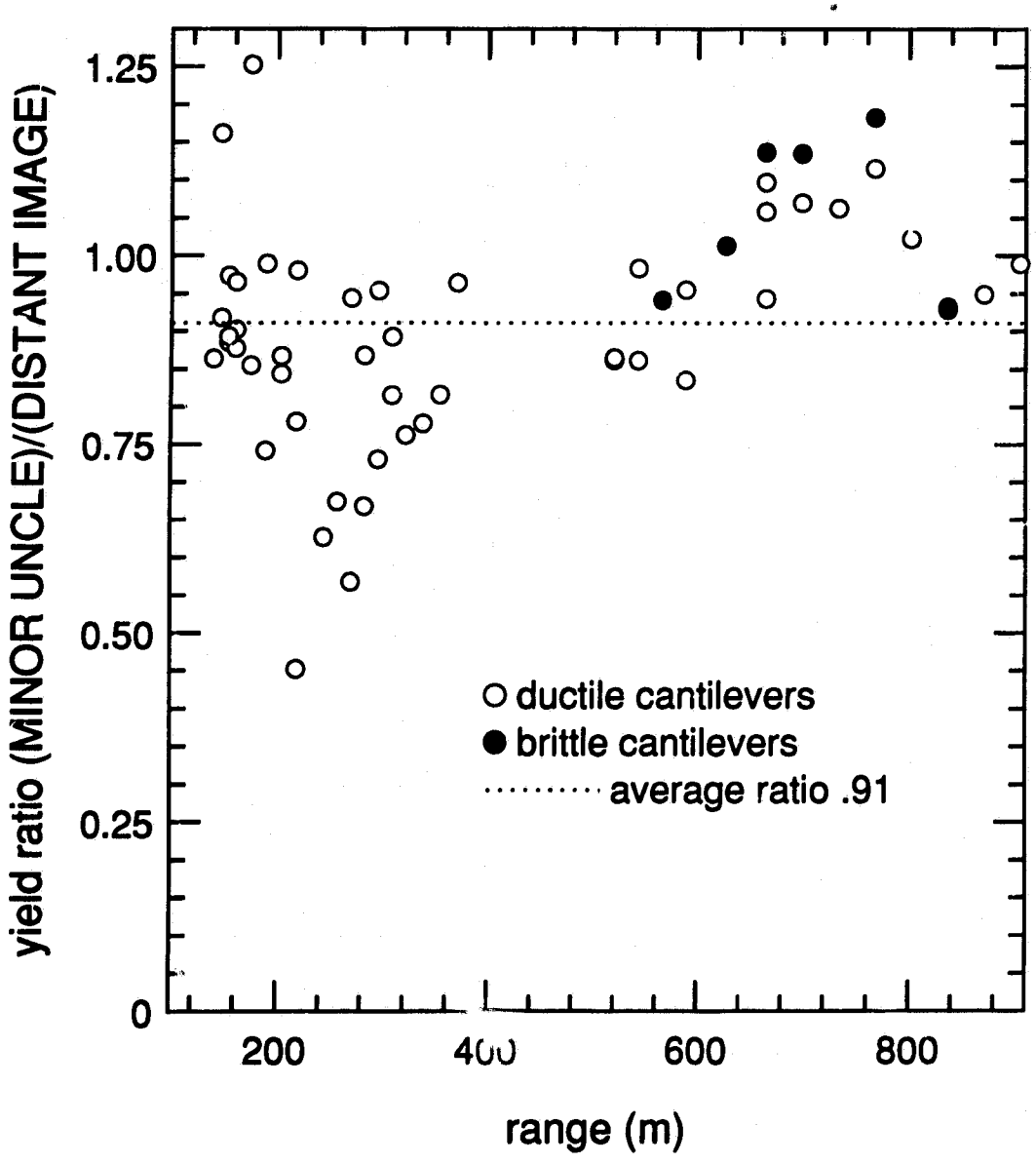

Figure 5.27: Ratio of the MINOR UNCLE to DISTANT IMAGE energy yields versus range obtained from the ductile and brittle cantilevers.

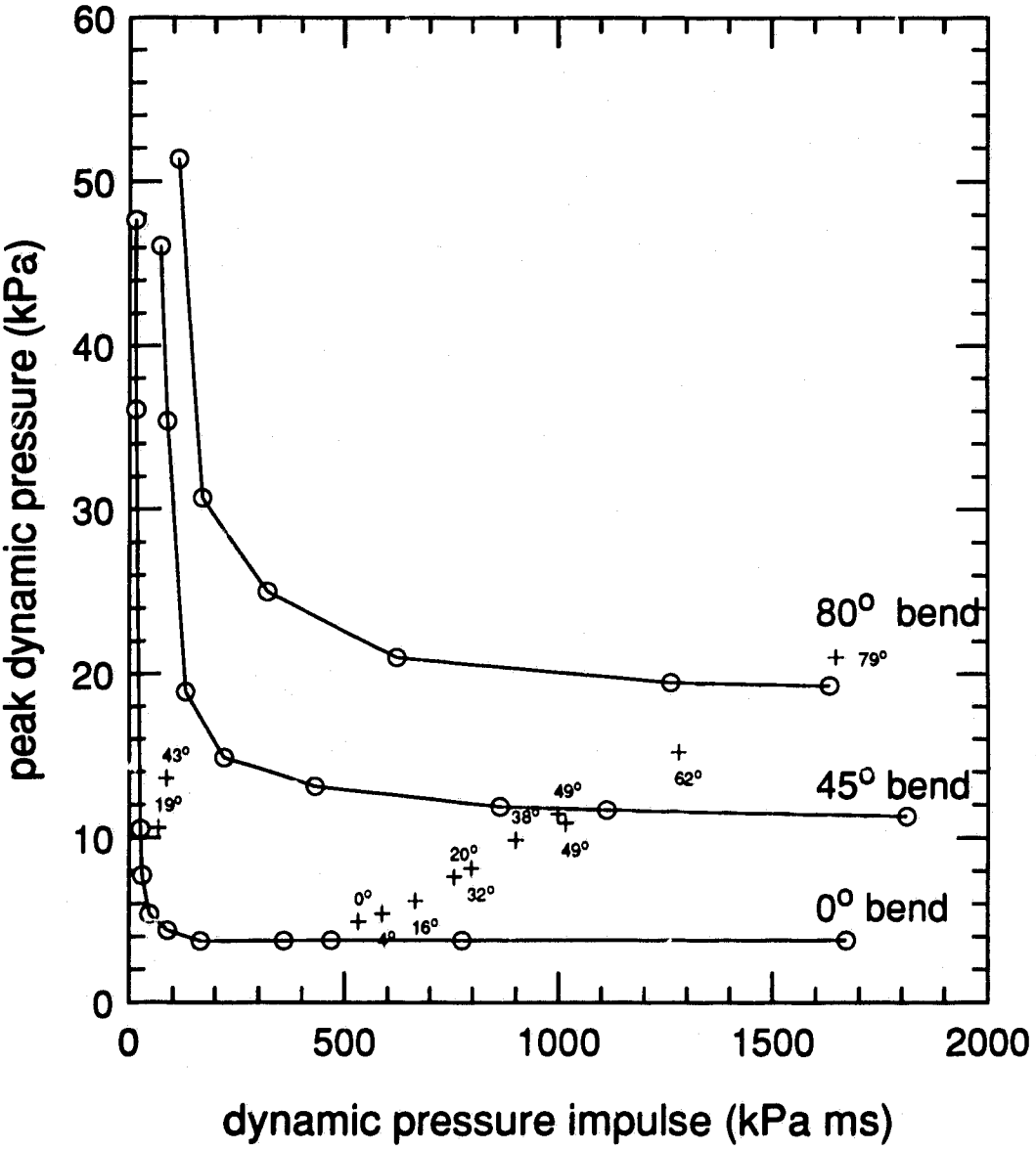

Figure 5.28: Dynamic pressure-impulse diagram for a cantilever made from aluminum 4043 0.15 m long, and 1.55 mm diameter. The isodamage curves were generated by the elastic-plastic model using theoretical loads created by *AirBlast*. The crosses are experimental data points.

in the shock tube experiments and in DISTANT IMAGE and MINOR UNCLE . The two data points on the left of the figure are from the shock tube experiments while the line of data points are from the two HE tests. As can be seen the agreement between the theory and experiment is good.

5.2.7 Horizontally mounted cantilevers

At DISTANT IMAGE four vertical arrays of cantilevers were mounted horizontally on vertical poles as described in chapter 4. Details of the cantilevers and the observed deformations are given in appendix B. This was a first attempt to use cantilevers to measure the variation of dynamic pressure with height above the ground. The lowest cantilever on each pole was mounted 10 cm above the ground and no significant variation of bending with height was observed. However there were regions where erratic bending. The first pole was at a radial distance of 382 m (1254 ft) and had uniform bending up to a height of 0.56 m (1.84 ft). Above this height the bending became erratic up to a height of 2.23 m (7.31 ft) after which uniform bending was again observed up to a height of 3.76 m (12.33 ft). The results from the pole at a radial distance of 534 m (1751 ft) showed a similar pattern of uniform and erratic bending although the region of erratic bending was confined between the heights of 1.01 m (3.31 ft) and 1.93 m (6.33 ft). The last two poles at radial distances of 610 m (2000 ft) and 686 m (2250 ft) did not show any regions of erratic bending. These results suggest that a region of disturbed flow may have existed between the indicated heights and that it dissipated somewhere between the radial distances of 534 m (1751 ft) and 610 m (2000 ft). Turbulent jets originating from within an explosive charge are often seen on high speed photographic records, and it is hypothesized that such a jet could have produced the erratic bend patterns seen on two of the poles.

There was no indication of any reduction of the dynamic pressure due to the

growth of the boundary layer behind the shock wave. The cantilever closest to the ground at all four stations was at a height of 0.10 m (4.0 in) and would be most affected by the boundary layer, but no obvious reduction in bend angle was observed. This null effect does not imply that there was no boundary layer and the explanation for this will be discussed later.

Mounting cantilevers poles provided only qualitative measurements of the variation of dynamic pressure with height since the 0.23 m diameter poles would change the characteristics of the flow and alter the dynamic pressure felt by the cantilevers. At MINOR UNCLE this factor was reduced by supporting the cantilevers on streamlined mounts, as described in chapter 4. Information about the horizontally mounted cantilevers are tabulated in appendix A for all the stations on the graded radial and for the two stations on ungraded ground. A photograph of the horizontal cantilevers at the 345 kPa (50 psi) overpressure level is given in figure 5.29. Each set of cantilevers mounted at distances corresponding to overpressure levels of 345, 207, 138, and 69 kPa (50, 30, 20, and 10 psi) over the graded ground had uniform angles of bend except for the lowest cantilever mounted 0.03 m above the ground. The bend angle of this cantilever was significantly less than that of the others indicating a reduction of dynamic pressure at this height. Uniform bending occurred at heights above 0.23 m (0.75 ft) at the 345, 207 and 138 kPa stations and above 0.13 m for the 69 kPa station indicating that the boundary layer detectable by the cantilevers did not propagate to these heights. At the 34 kPa station the bending at 0.03 m above the ground was greater than that at other heights. It is suggested that this effect may have been caused by the dust and small stones carried from higher pressure levels, *i.e.* from closer to the charge. The variation of bending angle versus height for all stations is plotted in figures 5.30 to 5.33.

The boundary layer over the ungraded ground affected the deformation of the cantilevers to a height of approximately 0.43 m (1.41 ft) at the 207 kPa station as compared to 0.23 m (0.75 ft) at the equivalent station over the graded area. This

Figure 5.29: Vertical array of horizontal cantilevers at the 345 kPa(50 psi) overpressure level showing the effect of the boundary layer only on the bottom cantilever. The bending was uniform above that height.

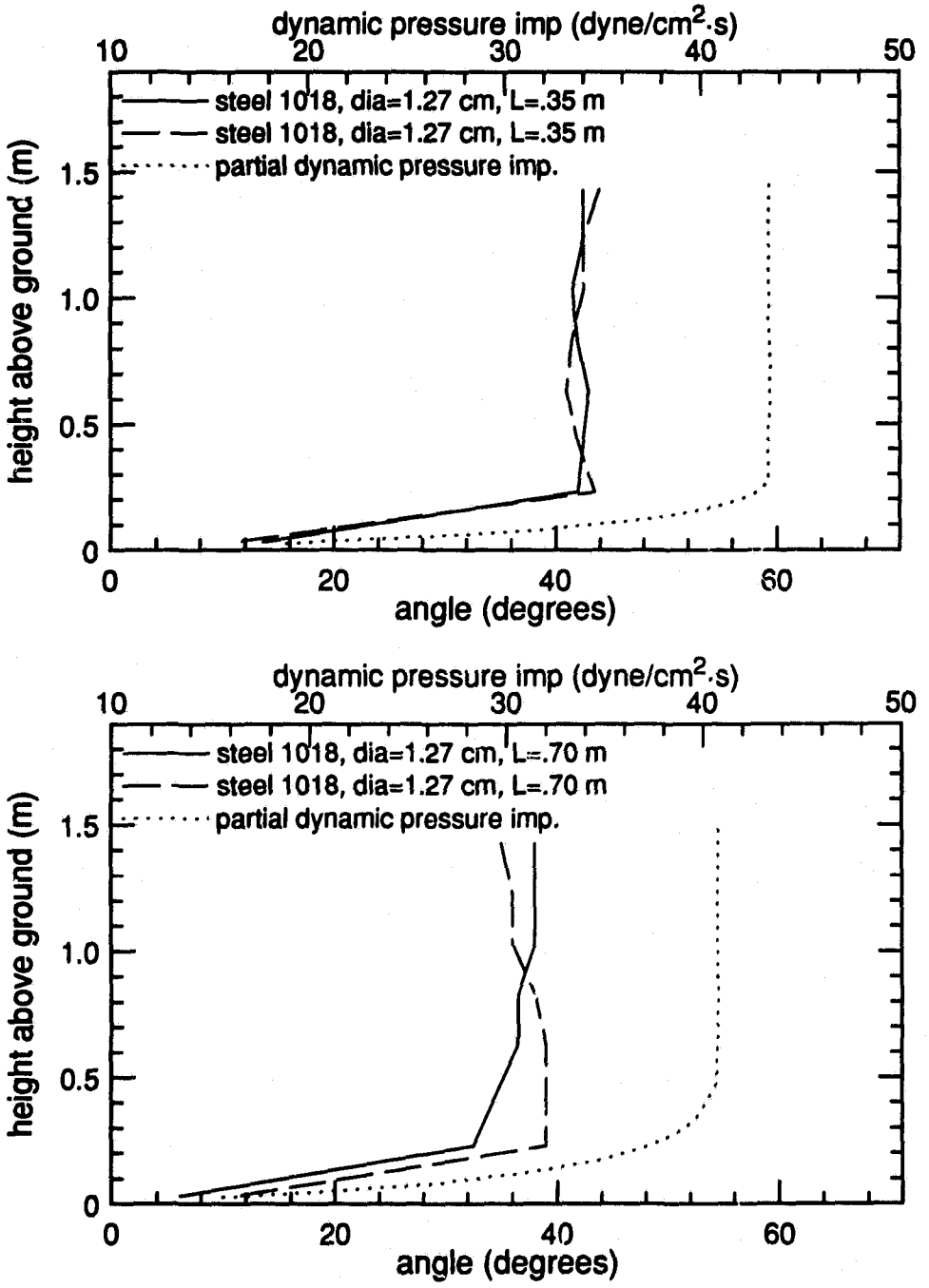

Figure 5.30: Bending profiles of horizontal cantilevers versus height for the 345 kPa(top) and 207 kPa(bottom) stations on graded ground and the calculated partial dynamic pressure impulses obtained from Needham, 1994.

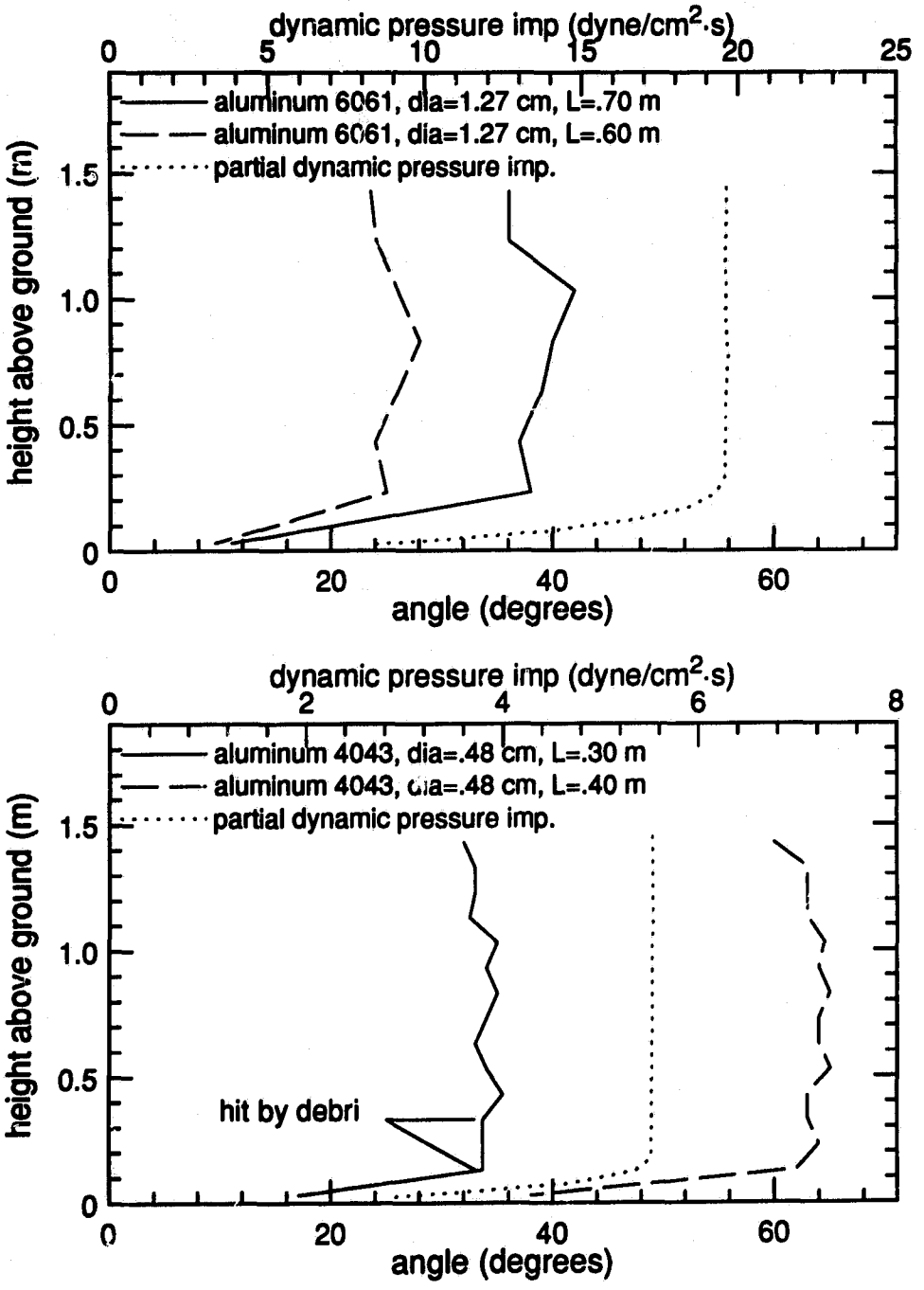

Figure 5.31: Bending profiles of horizontal cantilevers versus height for the 138 kPa(top) and 69 kPa(bottom) stations on graded ground and the calculated partial dynamic pressure impulses obtained from Needham, 1994.

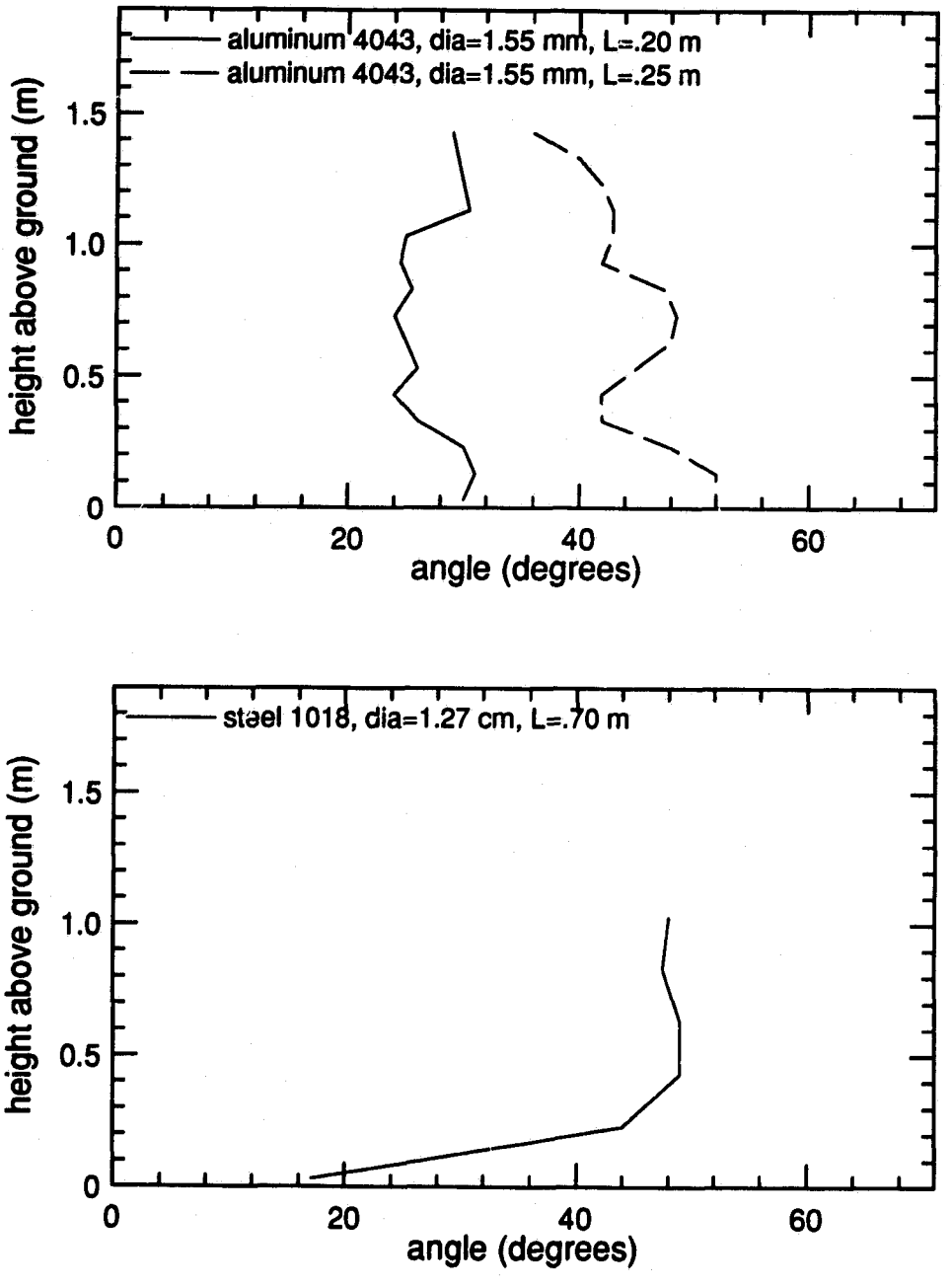

Figure 5.32: Bending profiles of horizontal cantilevers versus height for the 34 kPa(top) station on graded ground and the 207 kPa(bottom) station on ungraded ground.

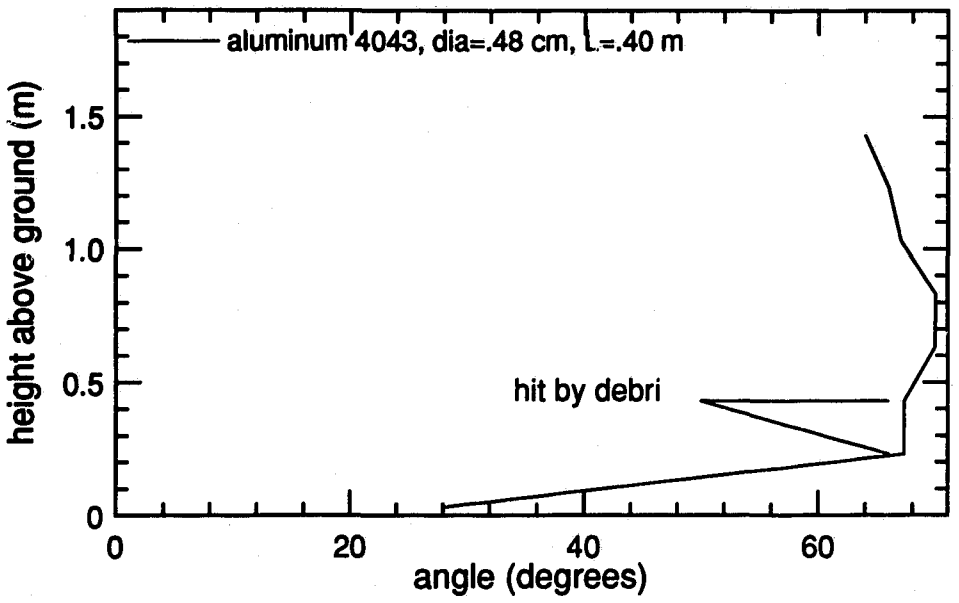

Figure 5.33: Bending profile of horizontal cantilevers versus height for the 69 kPa station on ungraded ground.

is to be expected since the speed of growth of the boundary layer is a function of the surface roughness. The average angle of bend for the highest cantilevers at this station, in theory unaffected by the boundary layer, bent to an angle of 48 degrees while over the graded ground identical cantilevers bent to an angle of 37 degrees. This difference is most likely due to an enhancement of the flow over the mounting structures since the structures used on the ungraded ground were approximately 30.0 cm thick with a blunt leading edge while on the graded ground were only 5.0 cm thick with a sharp leading edge. The comparison between the gauges over the two types of ground at the 10 psi stations could not be done since in both cases the second and third cantilevers above the ground were hit by debris.

Even though the boundary layer was not detected by the cantilevers higher than 0.23 m over the graded ground or 0.43 m over the ungraded ground this does not mean it did not propagate above these heights. The cantilevers only measure variations in the flow during the bending process and if the bending period of the cantilever

is significantly less than the positive phase duration of the blast wave it will only measure the extent of the boundary layer up to the bending period time. The cantilever results do not provide therefore the full boundary layer height.

The bending periods were obtained by using the elastic-plastic model and the measured values of dynamic pressure obtained from *AirBlast*. The theoretical values for the deformation times were calculated for the cantilevers at the 345, 207, 138, 69 and 34 kPa levels. The results of these calculations are given in table 5.2. Figure 5.34 gives an example of a time history of the bending process plotted with the dynamic pressure time history. The cantilever stops deforming plastically even though the blast wave induced flow has not yet terminated. These times limit the maximum possible growth rate of the boundary layer to the height of the lowest cantilever unaffected by the boundary layer. Therefore, if the growing boundary layer reaches a cantilever before this time its influence may be detected and conversely, if the boundary layer does not grow to the height of the cantilever within the bending time, that cantilever will not be influenced by the boundary layer.

Table 5.2: Response times for cantilevers.

psi level	material* and size (m)	height above ground (m)	time (sec)
50	s1018 L=.347, dia=.0127	0.23	0.0161
30	s1018 L=.700, dia=.0127	0.23	0.0448
20	a6061 L=.700, dia=.0127	0.23	0.0373
20	a6061 L=.600, dia=.0127	0.23	0.0293
10	a4043 L=.397, dia=.0048	0.13	0.0325
5	a4043 L=.200, dia=.0016	0.03	0.0245
5	a4043 L=.250, dia=.0016	0.03	0.0329
30rough	s1018 L=.700, dia=.0127	0.43	0.0448

* s = steel, a = aluminum, L = length, dia = diameter, rough = ungraded ground.

A two dimensional hydrodynamic simulation called the SHARC code was used

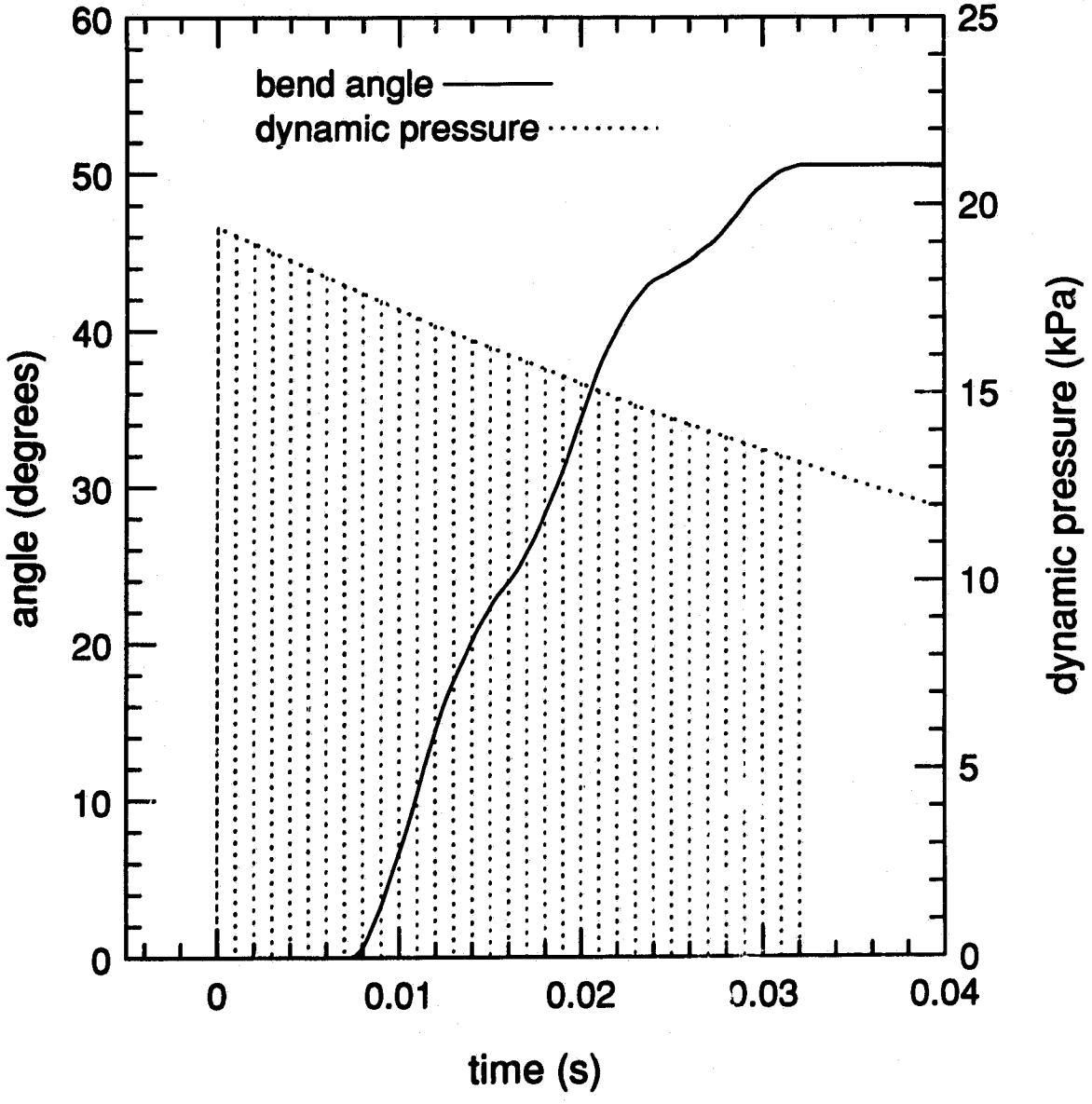

Figure 5.34: Time histories of dynamic pressure and deformation of a 0.397 m long, 4.8 mm diameter aluminum 4043 cantilever at a distance of 451 m from the MINOR UNCLE explosion(69 kPa level). The shaded area represents the impulse absorbed by the cantilever during the deformation and the deformation profile is obtained from the e-p model.

to simulate the growth of the boundary layer in the MINOR UNCLE blast wave. The calculations were performed by the S-CUBED division of Maxwell Industries (Albuquerque, N.M.) (Needham, 1994) at the overpressure levels of 345, 207, 138 and 69 kPa. The partial dynamic pressure impulse at the various cantilever heights was calculated based on the results of this hydrodynamic simulation. The partial impulses were obtained by integrating the dynamic pressure up to the cantilever response times given in table 5.2. The results of the partial dynamic pressure impulses are shown in figures 5.30 and 5.31 for the comparison with the cantilever results. The partial dynamic pressure impulse profiles correspond well with the observed deformation of the cantilevers at all stations. This agreement, although qualitative, does indicate that the use of cantilevers can be a viable method for measurement of the boundary layer growth of an unsteady flow such as that produced behind a blast wave.

Appendix A includes information on dust abrasion vs height obtained from the horizontally mounted cantilevers. This was obtained by a qualitative observation of the amount of dust abrasion on the surface of the leading edge of each cantilever at each station. At the 345 and 207 kPa stations the maximum surface abrasion occurred at a height of 0.23 m (.75 ft) and at the 138 kPa station it was observed at the 0.43 m (1.41 ft) height. At these three stations the maximum extent of the surface abrasion was observed up to a height of 1.03 m (3.4 ft). At the 69 kPa station no position of maximum abrasion could be identified, however uniform abrasion was observed up to 0.83 m (2.7 ft) above the ground. No surface abrasion effects were observed at the 34 kPa station although dust was deposited on the cantilevers.

5.2.8 Brittle cantilevers

The use of brittle cantilevers as a measurement of peak dynamic pressure was first attempted at the DISTANT IMAGE explosion using graphite pencil leads. Sets of these types of gauges were used at three distances from GZ as described in chapter 4. The first set was at a distance of 451 m (1480 ft) and at this station all cantilevers

were broken, indicating a peak dynamic pressure in excess of 76.7 kPa (based on equation 3.35). The electronic gauges measured a peak dynamic pressure of 19.9 kPa which is significantly less than the limit given by the cantilevers at that station. Recall the results of the horizontally mounted cantilevers at MINOR UNCLE where at the 10 psi station (451.0 m) abrasion effects were monitored up to a height of 0.83 m. The graphite cantilevers were mounted on streamlined platforms as described in chapter 4 at a height above the ground of about 0.6 m (2.0 ft). It is therefore reasonable to assume that the above discrepancy is most likely caused by an effective dynamic pressure enhancement due to entrained dust and small particles. Brittle cantilevers because of their nature are extremely sensitive to any variations in the flow and will generally break when struck by any debris.

At the 664.0 m (2181 ft) station the three tallest cantilevers broke and the four shorter ones were intact. Using this information with equation 3.35 and a drag coefficient of 1.2, indicates a peak dynamic pressure between 5.2 kPa and 7.76 kPa. Electronic gauges measured a peak dynamic pressure of 6.4 kPa at this distance which is consistent with the above result. None of the brittle cantilevers at a distance of 938 m (3080 ft) failed. This result provides an upper limit for the peak dynamic pressure of 2.75 kPa which is consistent with the electronic gauge result of 1.79 kPa. The results are summarized in table 5.3 below.

Table 5.3: Peak dynamic pressure measurements:DISTANT IMAGE.

Distance from GZ (m)	Brittle Cantilevers P_d (kPa)	Electronic Gauges P_d (kPa)
451.12	> 76.7	19.9
664.42	$5.2 < P_d < 7.76$	6.4
938.75	< 2.75	1.79

Six sets of brittle cantilevers were positioned at MINOR UNCLE between distances from the charge of 565 m (1853 ft) and 836 m (2743 ft). The stations were placed further from GZ than the closest brittle cantilever station at DISTANT IMAGE to reduce the chances of cantilever breakage by debris. The condition where the tallest cantilevers broke and the shorter remained intact occurred at all stations. The results for each station are given in appendix A.

If equation 3.35 was used with a C_d of 1.2 the values of peak dynamic pressure obtained were on average about 28% higher than those measured by the electronic gauges. A possible explanation for this discrepancy is that the graphite used at DISTANT IMAGE may have had some different material properties than the graphite used at the MINOR UNCLE explosion even though the measured yielding stresses required for breakage were the same.

A calibration was done for each set of cantilevers as described in section 5.1.4 and the resulting calibration curve is plotted in figure 4.5. This calibration was used with the observed breakage pattern to provide the peak dynamic pressure versus range for the brittle cantilevers at MINOR UNCLE. The results are plotted in figure 5.26 with the results obtained from the electronic gauges, the *AirBlast* program and the ductile cantilevers. The match is good although the peak dynamic pressure is higher than the results of the electronic gauges and the *AirBlast* program, but are consistent with the results of the ductile cantilevers. Referring back to figure 5.27 the yield ratio as determined by the brittle gauges was calculated to be 1.056. The numerical average of the yield fraction for all ductile and brittle gauges gives a yield for MINOR UNCLE of 0.91 that of DISTANT IMAGE. The actual size of DISTANT IMAGE is 2.650 kt and for MINOR UNCLE is 2.431 kt which gives a fraction of 0.92.

5.3 Applications

5.3.1 Evaluation of accidental explosions

In general there will be no electronic measuring devices near an accidental explosion and therefore the only method that can be applied to determine the various blast wave properties of the explosion is one which analyizes the damage to surrounding structures. Examples of simple structures such as cantilevers can be found near most explosions and the deformation of these can be correlated to the strength of the blast wave. The following paragraphs will describe how the peak dynamic pressure and the dynamic pressure impulse can be found from the deformation of a blast loaded cantilever and how this information can provide the TNT equivalent energy yield of the accidental explosion.

Let us assume that a cantilever of length 15.0 cm and diameter 0.15 cm has been found 100 meters from the center of an accidental explosion. The angle of the cantilever was measured to be 45° and it was subsequently removed and the material properties were tested. It was determined that the cantilever was made from aluminum 4043. A pressure-impulse diagram for this particular cantilever is given in figure 5.35 and was generated by the elastic-plastic numerical model. This figure is similar to figure 5.32 but also includes the isocharge curves. These curves are based on the hypothetical charges used to provide the blast waves for the theoretical loading imposed on the 15.0 cm aluminum cantilever.

The 45° angle of bend can be produced by very large charges if the cantilever is far from the charge or by very small charges if the cantilever is near to the charge. Figure 5.35 shows the peak dynamic pressure and impulse combinations for the surface burst TNT charges ranging from about 100 kg to 10^7 kg that produce the 45° bend but it does not directly provide any information about the distance the cantilever was from the center of the explosion. This information is provided by plotting the peak dynamic pressure versus range and the dynamic pressure impulse

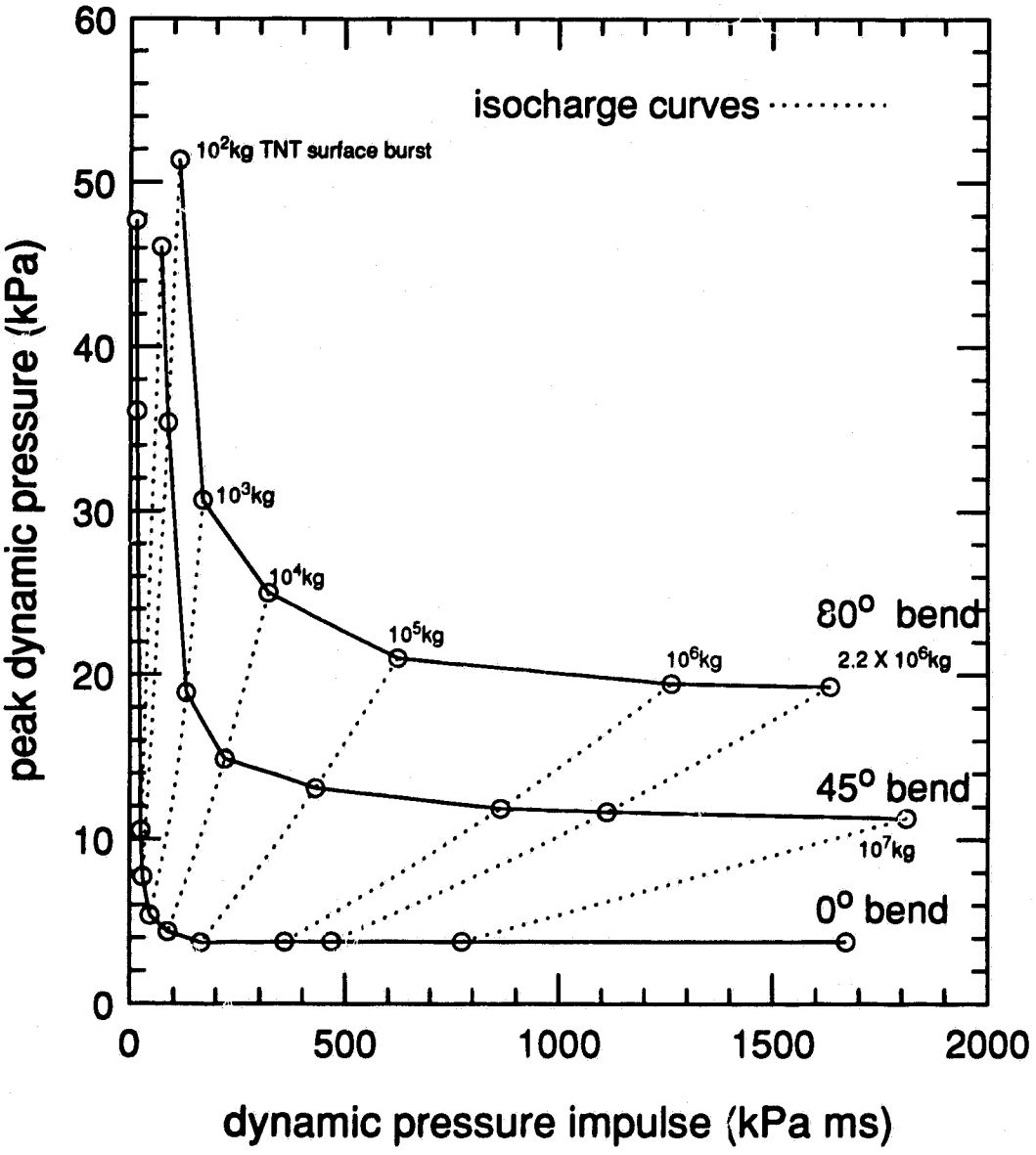

Figure 5.35: P-I diagram for an aluminum 4043 cantilever 15 cm long and 0.15 cm in diameter. The isodamage curves(0°, 45°, and 80°) were generated by the elastic-plastic model. Also plotted are the isocharge curves which indicate the peak dynamic pressure and dynamic pressure impulse combination required to produced the specified damage.

versus range for the various TNT charges as shown in figures 5.36 and 5.37. These curves can all be obtained from a program such as *AirBlast*, or if the variations of peak dynamic pressure and dynamic pressure impulse for a unit charge are obtained from a handbook, the other curves can be derived using cube root scaling.

The peak dynamic pressure and dynamic pressure impulse required to deform the cantilever to 45° can be found in figure 5.35 by finding the intersections of the various TNT charges with the 45° deformation curve. These values are plotted in figures 5.36 and 5.37 to produce the 45° deformation curves, as shown. The cantilever in question was discovered 100 m from the center of the accidental explosion and therefore the intersection of the 100 m line with the 45° deformation curves as shown in figures 5.36 and 5.37 provide the peak dynamic pressure and the dynamic pressure impulse combination that existed at the position of the cantilever during the explosion. The resulting peak dynamic pressure and the dynamic pressure impulse was found to be 14.7 kPa and 253 kPa ms respectively.

The energy yield of the explosion can be found from either value but it is easiest to use the peak dynamic pressure since the value of the peak dynamic pressure does not change as the impulse does through blast wave scaling (see section 2.4.3). The *AirBlast* program was used to determine that the measured peak dynamic pressure of 14.7 kPa exists at a radial distance from a 1 kg TNT surface burst charge of 3.99 m. This value can be used with cube root scaling to determine the effective yield as shown below:

$$W_{eff} = \left[\frac{100m}{3.99m}\right]^3 1.0kg = 15700kg \tag{5.1}$$

It can therefore be assumed that the blast wave at 100 m from the accidental explosion is similar to that produced by the detonation of 15,700 kg TNT on the ground surface. The peak dynamic pressure versus range for this charge is also plotted in figure 5.36.

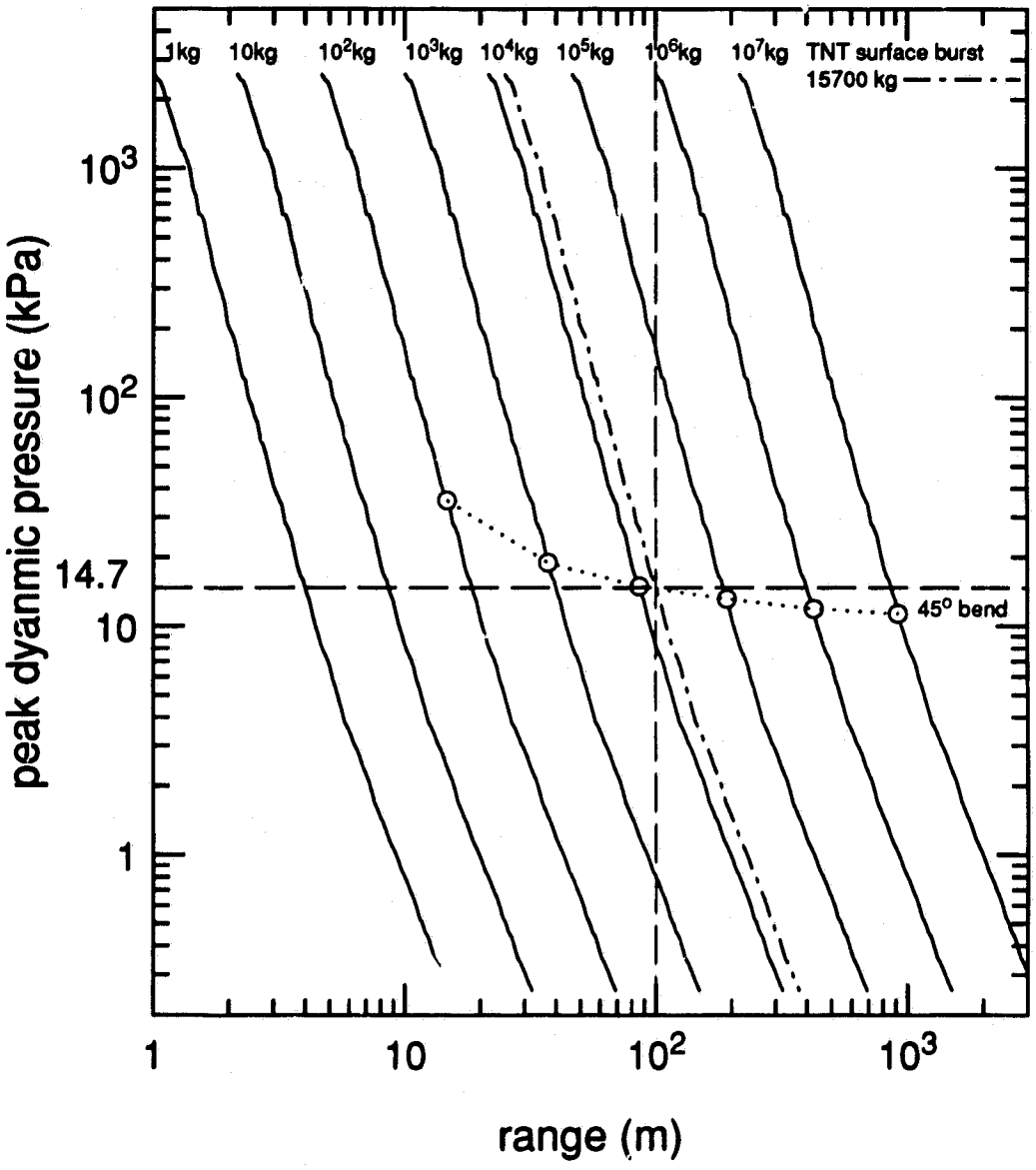

Figure 5.36: Peak dynamic pressure versus range for various TNT charge weights between 1 kg and 10^7 kg obtained from *AirBlast*. Also plotted is the 45° deformation line for the 15 cm aluminum cantilever. The intersection of this curve with the charge curves gives the peak dynamic pressure and distance from the charge needed to produce a 45° bend for this cantilever. Since the cantilever was assumed to be 100 m from the center of the explosion this identifies the peak dynamic pressure to be 14.7 kPa and the TNT equivalent charge size to be 15,700 kg.

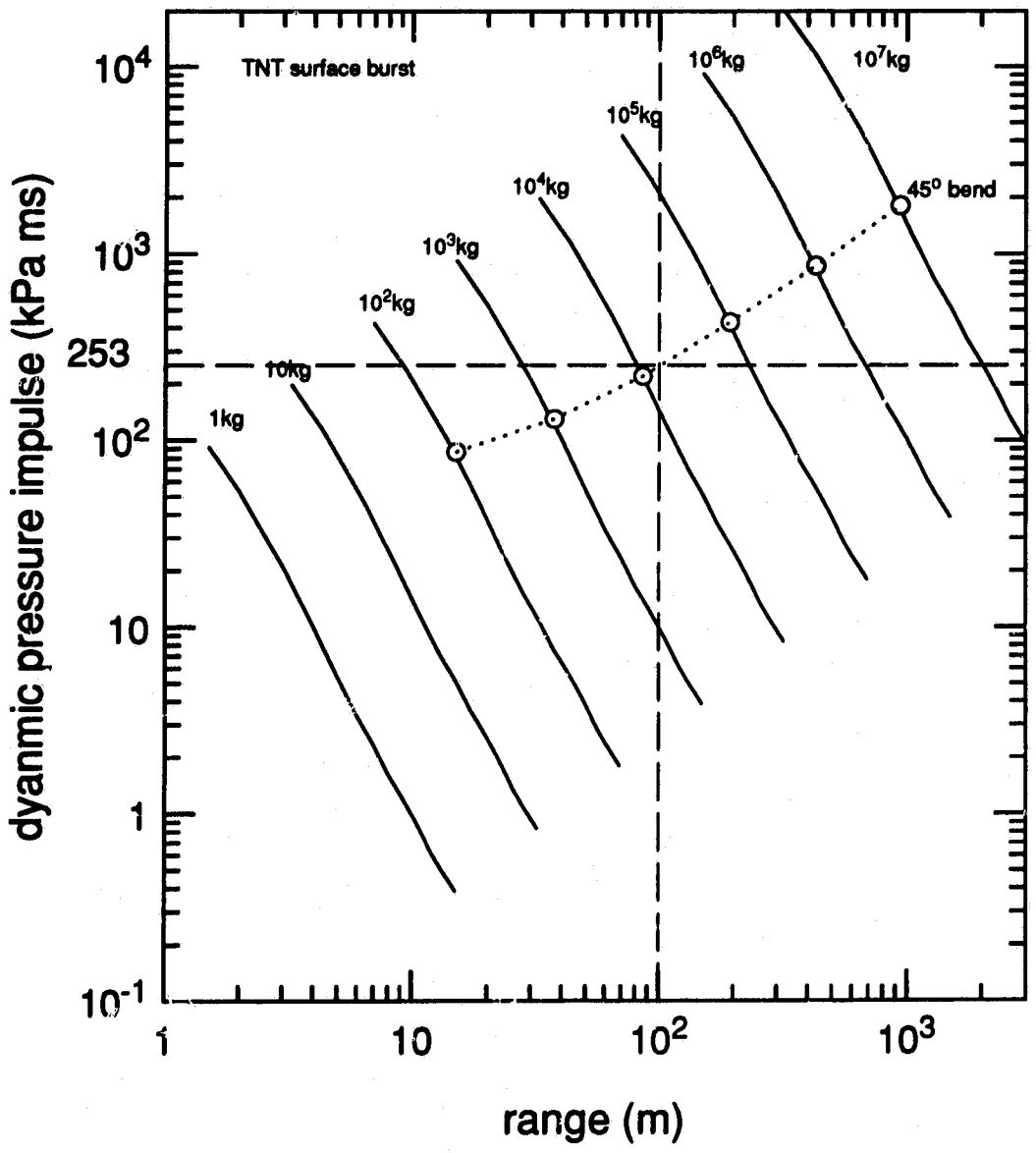

Figure 5.37: Dynamic pressure impulse versus range for various TNT charge weights between 1 kg and 10^7 kg obtained from *AirBlast*. Also plotted is the 45° deformation line for the 15 cm aluminum cantilever. The intersection of this curve with the charge curves gives the dynamic pressure impulse and distance from the charge needed to produce a 45° bend for this cantilever. Since the cantilever was assumed to be 100 m from the center of the explosion this identifies the dynamic pressure impulse to be 253 kPa ms.

5.3.2 Identification of potential cantilever gauges

If cantilevers are to be used as blast wave gauges at high explosive tests it will be useful to identify those cantilevers, made from readily available materials, which would provide useful angles of bend for the range of dynamic pressures expected at various locations. This can be determined by using plots similar to those described in section 5.3.1. For example, if the cantilever as described above was to be used as a blast wave gauge it should be placed at a radial distance from ground zero where a 45° bend would be expected. The distance can be found by observing the intersection points of the 45° curve with the various charge curves in either figure 5.36 or 5.37. For a charge thought to be similar to 100 kg TNT surface burst, this cantilever should be placed at about 15 meters from the charge center. If the charge were thought to be equivalent to 10^7 kg of TNT the cantilever should be placed at a distance of about 1000 meters. Plots such as shown in figures 5.35 to 5.37 can be made for a wide variety of cantilevers made from easily obtained materials so that at a given explosive event a variety of cantilevers could be placed at different distances to monitor the blast wave.

At most explosions the blast waves produced are far from the ideal blast wave expected for the given charge weight and it is therefore necessary to position cantilevers in such a way as to bracket the optimum 45° bend. This is done to ensure a reasonable measurement at all stations.

It is hoped to use this technique to develop a handbook and/or a software package that will provide experimentors with the information so that appropriate cantilever gauges can be made for expected blast conditions.

Chapter 6

Discussions and conclusions

The main objectives of this project were: to understand the relationships between the physical properties of shock and blast waves and the response of circular cross-section cantilevers exposed to those waves; to use that understanding to design cantilever gauges that can be used to monitor the physical properties of blast waves, and, to illustrate how the deformation of cantilever structures may be used to describe the source of blast waves produced by accidental explosions. These objectives have been met.

Two models were developed to describe the deformation of the blast loaded ductile cantilevers. These were based on the assumption that the cantilevers would respond to the blast wave either as a rigid-plastic or an elastic-plastic structure. The plastic deformation was assumed to occur at the clamped end of the cantilever. These models assumed that the loads could be related to the dynamic pressure and the drag coefficient, which were both time varying properties.

It was found that the rigid-plastic model would accurately describe the deformation of cantilevers made from solid solder. This model always overestimated the deformation for cantilevers made from other materials. However it does provide a good first order estimate of the deformation, and can be used to identify which cantilevers to be placed at various distances from an explosion so as to achieve bending of approximately 45°.

The elastic-plastic model was developed to improve the predicted response of

cantilevers made of other materials. This model allowed for an elastic response throughout the cantilever and also included strain hardening and strain-rate hardening of the material during the plastic deformation. The algorithm used was based on the premise that the curvature of the cantilever could not exceed a value which was determined by the yield stress of the material. The performance of this model was tested in experiments within the shock tube on cantilevers made of aluminum 4043 and 5056 and of various lengths from 0.06 m to 0.25 m. The model predicted the final angles of deformation in most cases to within a few degrees. The predicted dynamic response of the model was also tested. High speed photographic recording of the loading process revealed a similar response as that predicted by the model, although it was found that the elastic response was underestimated somewhat. To improve the model a true two dimensional simulation should be used. The deformation rate of the cantilever was found to oscillate due to elastic vibrations set up by the impulsive load. This was also observed in the film recordings. This result indicated that the plastic deformation of the cantilever was also dependent on the elastic properties of the material. The solutions provided by this model were sensitive to the properties assigned to the materials. Not all of the properties could be directly measured, these being mainly the strain and strain-rate hardening terms. The available information on these properties for the materials tested is limited and therefore approximate values were used.

Brittle cantilevers made from a graphite material were loaded by the shock tube flow to test a simplified brittle model. The experiments revealed that a drag coefficient of 1.2, the expected steady-state value, was not large enough to predict when a given cantilever would fail using this simplified model. Repeated experiments on brittle cantilevers whose lengths ranged from 7.50 cm to 3.25 cm showed that there was a decrease in the peak dynamic pressure required to produce failure with an increase in length except when the cantilever was about 4.0 cm long. A slight increase in length beyond this value yielded the unexpected result that the dynamic

pressure required to produce a failure of the specimen increased above that required to produce failure in the shorter cantilever. It was found that the duration of the loading was longer than 1/4 the natural period of the 4.0 cm cantilever and was shorter for a cantilever of length 4.6 cm. In otherwords the shorter cantilever was peak pressure sensitive while increasing the length slightly caused the cantilever to become impulse sensitive.

Over 800 cantilevers were deployed at the two high explosive events code named DISTANT IMAGE(2,650 tons ANFO) and MINOR UNCLE(2,431 tons ANFO). There was some scatter in the experimental data which was most likely caused by such effects as ejecta, dust entrainment and inconsistent material properties. The experimental deformations of the solder cantilevers at the same radial distance from the two events showed little statistical difference even though DISTANT IMAGE was a larger explosion than MINOR UNCLE. The rigid-plastic model appeared to predict the response of the solder cantilevers relatively well at both events.

There was good agreement between the response predicted by the elastic-plastic model and the observed deformations for cantilevers made from the materials tested within the shock tube, those being aluminum 4043 and aluminum 5056. The agreement was reasonable for steel 1018 and not as good for aluminum 6061. Lack of knowledge about the drag coefficient in unsteady flows, inaccuracies in the elastic and plastic properties of the ductile materials, and departures from ideal blast wave flows due to causes such as boundary layer effects and dust entrainment mean that a significantly better agreement between the deformations predicted by the elastic-plastic model and those observed in the experiments cannot reasonably be expected. A more detailed model could be developed by taking into account such effects as shear as well as allowing the entire cantilever to deform plastically in a true elastic-plastic fashion, but in view of the other uncertainty, such a development does not seem justified at this time.

The observed deformations of the ductile cantilevers on DISTANT IMAGE and

of the brittle cantilevers in the shock tube were used to calibrate the cantilevers on MINOR UNCLE as peak dynamic pressure gauges. The resulting variation of the peak dynamic pressure as a function of distance agreed very well with independent measurements using electronic gauges and the photo-diagnostic technique. The dynamic pressure variation used with the cube root scaling law indicated an energy yield ratio between MINOR UNCLE and DISTANT IMAGE of 0.91. The ratio of the charge masses was 0.92.

Vertical arrays of horizontally mounted cantilevers were used to measure the variation of dynamic pressure with height above the ground. At MINOR UNCLE five sets of these were positioned on graded ground at radial distances of 218 m, 270 m, 321 m, 451 m and 664 m, and two sets on ungraded ground at radial distances of 270 m and 451 m. Over the graded ground the observations indicated that during the response time of the cantilevers at 218 m, 270 m, and 321 m from the charge, the edge of the boundary layer had not risen higher than 0.23 m and for the cantilevers mounted a distance of 451 m from the charge the boundary layer did not reach higher than 0.13 m in their response times. At 664 m the boundary layer did not appear affect the cantilever deformations. In fact the maximum in bending was at the lowest cantilever, and this was possibly due to the presence of dust entrained from regions closer to the charge. Over the ungraded ground at a distance from the charge of 270 m no variation in bending was found above 0.43 m. In other words the boundary layer appears to have grown to a height of no higher than 0.43 m during the response time of the cantilevers mounted at that station.

It is concluded that the rigid-plastic model, in the case of solder cantilevers only, and the elastic-plastic model in the case of the other ductile materials gave valid predictions of the deformations of circular cross-section cantilevers exposed to blast waves. The present uncertainty about some of the material properties and about the unsteady drag coefficient, together with variations in the blast wave properties due to such effects as the boundary layer and entrained dust, do not appear to justify a

more sophisticated model at this time.

Using the appropriate model, it has been shown how cantilever gauges made from easily available materials can be selected to monitor blast waves, whose properties are known approximately. From an array of such gauges the values of the peak dynamic pressure and/or the dynamic pressure impulse can be determined. Cantilever gauges also give a clear mapping of the direction of the blast wave flow from non-symmetrical sources. This information can be used to provide the TNT equivalent energy yield of an explosion.

In the case of an accidental explosion it has been shown how the observed bending of a cantilever structure at a known distance from the center of the explosion, can be used to estimate its yield and the physical properties of the blast wave.

Bibliography

Baker, W.E., Ewing, W.O., Hanna, J.W., 1958, *Laws for Large Elastic Response and Permanent Deformation of Model Structures Subjected to Blast Loading*, Ballistic Research Laboratories, Rept. 1060.

Baker, W.E., Cox, P.A., Westine, P.S., Kulesz, J.J., Strehlow, R.A., 1983, *Explosion Hazards and Evaluation*, Elesevier Science Publishing Company Inc., New York.

Binninger, G., Deel, C., Thomas, C., 1981, *Air Blast Drag Loading Experiments, MIGHTY MACH III*, Defence Nuclear Agency 5719F.

Binninger, G., Deel, C., 1983, *Air Blast Drag Loading Experiments, Events MILL RACE and MIGHTY MACH IV*, Defence Nuclear Agency, TR-81-332.

Bodner, S.R., Symonds, P.S., 1962, *Experimental and Theoretical Investigation of the Plastic Deformation of Cantilever Beams Subjected to Impulsive Loading*, J. Appl. Mech. **29**, 719-728.

Book, D.L., Boris, J.P., Hain, K., 1975, *Flux Corrected Transport 2: Generalizations of the Method*, J. Computational Phys., **18**, 248-283.

Deel C., 1984, *Airblast Drag Loading Experiments event DIRECT COURSE*, Defence Nuclear Agency, TR-84-61.

Dewey, J.M., 1962, *Surface Burst of a 100 ton TNT Hemispherical Charge Wire Drag Gauge Measurements*, Suffield Experimental Station, T.N. 80.

Dewey, J.M., McMillin, D.J., 1989, *A Computer System for Presenting the Properties of Blast Waves*, Proc. 11^{th} Int. Symp. on Military Application of Blast Simulation. MABS11, **1**, 554-561.

Dewey, J.M., McMillin, D.J., 1992, *Smoke Puff Photo Diagnostics*, DISTANT IMAGE symp. rept., Defence Nuclear Agency, POR 7379-2, **2**.

Dewey, J.M., McMillin, D.J., 1995, *Smoke Puff Photo Diagnostics*, MINOR UNCLE symp. rept., Defence Nuclear Agency, POR 7453-2, **2**.

Ekler, R.G. Kennedy, L.W., Needham, C.E., 1995, *Boundary Layer Modeling*, MINOR UNCLE symp. rept., Defence Nuclear Agency, POR 7453-2.

Ewing, W.O., Hanna J.W., 1957, *A Cantilever For Measuring Air Blast*, Ballistic Research Laboratories, T.N. 1139.

Ethridge, N., Dixon-Hiester, L.A., Jackson, W.F., Peterson,R.S., 1990, *Dust Measurements*, MISERS GOLD Symp., Defence Nuclear Agency, POR 7352-3, **3**.

Ethridge, N., 1992, *Displacement of Cubes by Blast*, DISTANT IMAGE Symp., Defence Nuclear Agency, POR 7379-3, **3**.

Gere, J.M., Timoshenko, S.P., 1984, *Mechanics of Materials*, Wadsworth Inc., California.

Glasstone, S, Dolan, P.J., 1977, *The Effects of Nuclear Weapons*, U.S. Atomic Energy Commission, rev. ed.

Hoerner, S.F., 1965, *Fluid Dynamic Drag*, published by author, Midland Park, New Jersey.

Hopkinson, B., 1915, British Ordnance Board Minutes 13565.

Hugoniot, H., 1887, Journal de l'Ecole Polytechnique.

Kinney, G.F., Graham, K.J., 1962, *Explosive Shocks in Air*, MacMillian, New York, New York.

Kim, Y.S., Ukrainetz, P.R., 1971_a, *Airblast Response of a Circular Cantilever Beam (U)*, Defence Research Establishment Suffield, Tech. Pap., 385.

Kim, Y.S., Ukrainetz, P.R., 1971_b, *Drag Loading on a Circular Cylinder from an Air Blast Wave (U)*, Defence Research Establishment Suffield, Tech. Pap., 392.

Manjoine M.J., 1944, *Influence of Rate of Strain and Temperature on Yield Stresses in Mild Steel*, J. Appl. Mech. **11**, 211.

Martin, V.C., Mead, K.F., Uppard, J.E., 1967, *The Drag on a Circular Cylinder in a Shock Wave*, Atomic Weapons Research Establishment, rept. O-34/67.

McMillin, D.J., Dewey, J.M., 1995, *Boundary layer Measurements using Miniature Smoke Trails*, MINOR Symp. rep., Defence Nuclear Agency, POR 7453-5, **5**.

Mellsen, S.B., 1971, *Measurements of Drag Cylinders by the Free Flight Method-Event DIAL PACK (u)*, Defence Research Establishment Suffield Tech. Pap., 382.

Mellsen, S.B., Naylor, R., 1969, *Aerodynamic Drag Measurements and Flow Studies on a Circular Cylinder in a Shock Tube (U)*, Defence Research Establishment Suffield, Suffield Mem. 7/69.

Mendelson, A., 1968, *PLASTICITY: Theory and Application*, The Macmillan company, New York.

Needham, C.E. et al, 1991, *ANFO.EXE: Revised User's Manual*, Defence Nuclear Agency, POR 7375.

Needham, C.E., 1994, personal communications.

Parkes, E.W., 1958, *The Permanent Deformation of an Encastre Beam Struck Transversely at Any Point in Its Span*, Proceedings of the Institution of Civil Engineers, **10** 277.

Penny, Lord, 1969, *The Nuclear Explosive Yields at Hiroshima and Nagasaki*, Roy. Soc. Phil. Trans., **266**, 357-424.

Rankine, W.J.M., 1870, *The Thermodynamic Theory of Waves of Finite Longitudinal Disturbance* , Phil. Trans. Roy. Soc., **160**.

Schlicting, H., 1960, *Boundary Layer Theory*, McGraw-Hill, New York.

Stephens, R.W.B., Bate, A.E., 1966, *Acoustics and Vibrational Physics*, Edward Arnold Publishers LTD, London.

Teel, G., 1992, *Free field air blast diagnostics*, DISTANT IMAGE symp. rep., Defence Nuclear Agency, POR 7379-1, **1**.

Teel, G., 1995, *Free field air blast diagnostics*, MINOR UNCLE symp. rep., Defence Nuclear Agency, POR 7453-1, **1**.

Thomson, W.T., 1972, *Theory of Vibration with Applications*, Prentice-Hall Inc., New Jersey.

Ting, T.C.T., Symonds, P.S., 1962, *Impact of a Cantilever Beam With Strain Rate Sensitivity*, Brown University, Office of Naval Research, T.R. 73.

van Netten, A.A., Dewey, J.M., 1992 *Cantilever gauges*, DISTANT IMAGE Symp. Defence Nuclear Agency, POR 7379-5, **5**.

Whitten, B.T., 1969, *Calibration of a Shock Tube by Analysis of the Particle Trajectories*, M.Sc. thesis, University of Victoria.

Appendix A

MINOR UNCLE:cantilever data

Table A.1: CANTILEVER POSITIONS AND TYPE:MINOR UNCLE.

Station and Cant. Number	Type	Distance (m) - (ft)	Length (m)	Diameter (m) - (in)	Bend Angle (°)
1-1	steel 1018	117.65-386	.493	.0254-1.	90^+
1-2	steel 1018		.302	.0254-1.	42.0
1-3	steel 1018		.407	.0254-1.	90^+
2-4	steel 1018	120.70-396	.499	.0254-1.	90^+
2-5	steel 1018		.301	.0254-1.	39.5
2-6	steel 1018		.399	.0254-1.	66.0
3-7	steel 1018	123.75-406	.504	.0254-1.	90^+
3-8	steel 1018		.298	.0254-1.	31.5
3-9	steel 1018		.404	.0254-1.	63.0
4-10	steel 1018	126.80-416	.498	.0254-1.	76.0
4-11	steel 1018		.297	.0254-1.	24.0
4-12	steel 1018		.402	.0254-1.	65.0
5-13	steel 1018	129.84-426	.501	.0254-1.	90^+
5-14	steel 1018		.297	.0254-1.	21.0
5-15	steel 1018		.400	.0254-1.	51.0
6-16	steel 1018	132.89-436	.498	.0254-1.	90^+
6-17	steel 1018		.299	.0191-.75	62.0
6-18	steel 1018		.194	.0127-.5	67.5
6-19	steel 1018		.402	.0254-1.	52.0
7-20	steel 1018	139.90-459	.496	.0254-1.	90^+
7-21	steel 1018		.400	.0191-.75	90^+
7-22	al 6061-T6		.227	.0191-.75	71.5

Table A–1(continued)

Station and Cant. Number	Type	Distance (m) - (ft)	Length (m)	Diameter (m) - (in)	Bend Angle (°)
7-23	steel 1018		.400	.0254-1.	38.0
8-24	steel 1018	146.91-482	.497	.0254-1.	68.0
8-25	steel 1018		.400	.0191-.75	90^+
8-26	al 6061-T6		.220	.0191-.75	64.0
8-27	steel 1018		.395	.0254-1.	40.5
9-28	steel 1018	153.92-505	.500	.0254-1.	53.0
9-29	steel 1018		.400	.0191-.75	65.5
9-30	al 6061-T6		.216	.0191-.75	43.5
9-31	steel 1018		.400	.0254-1.	25.0
10-32	al 6061-T6	160.93-528	.500	.0254-1.	42.5
10-33	steel 1018	161.93-528	.399	.0191-.75	57.5
10-34	al 6061-T6		.227	.0191-.75	33.0
10-35	steel 1018		.750	.0254-1.	90^+
11-36	steel 1018	175.26-575	.502	.0254-1.	45.0
11-37	steel 1018		.400	.0191-.75	44.5
11-38	al 6061-T6		.224	.0191-.75	25.0
11-39	steel 1018		.746	.0254-1.	73.0
12-40	steel 1018	189.59-622	.499	.0254-1.	14.0
12-41	steel 1018		.398	.0191-.75	33.0
12-42	al 6061-T6		.225	.0191-.75	9.0
12-43	steel 1018		.749	.0254-1.	54.0
13-44	steel 1018	203.91-669	.499	.0254-1.	8.0
13-45	steel 1018		.402	.0191-.75	11.5
13-46	al 6061-T6		.223	.0191-.75	3.5
13-47	steel 1018		.750	.0254-1.	34.0
14-48	steel 1018	218.24-716	.502	.0254-1.	0.0
14-49	steel 1018		.401	.0191-.75	0.0
14-50	al 6061-T6		.496	.0191-.75	46.5
14-51	steel 1018		.750	.0254-1.	47.5
15-52	steel 1018	244.14-801	.750	.0254-1.	5.0
15-53	al 6061-T6		.498	.0191-.75	42.5
15-54	al 6061-T6		.504	.0191-.75	56.0
15-55	al 6061-T6		1.004	.0254-1.	90^+
16-56	al 6061-T6	257.25-844	.550	.0191-.75	22.5
16-57	al 6061-T6		.996	.0254-1.	66.0
17-58	al 6061-T6	270.05-886	.535	.0191-.75	3.0
17-59	al 6061-T6		1.662	.0254-1.0	73.0
18-60	al 6061-T6	283.00-929	.500	.0191-.75	3.5

Table A–1(continued)

Station and Cant. Number	Type	Distance (m) - (ft)	Length (m)	Diameter (m) - (in)	Bend Angle (°)
18-61	al 6061-T6		1.658	.0254-1.	42.0
19-62	al 6061-T6	295.95-971	.500	.0191-.75	2.5
19-63	al 6061-T6		1.660	.0254-1.	37.5(hit)
20-64	al 6061-T6	308.91-1014	.498	.0191-.75	2.0
20-65	al 6061-T6		1.662	.0254-1.	24.0
21-66	al 6061-T6	321.87-1056	1.661	.0254-1.	14.0
21-67	al 6061-T6		1.000	.0127-.5	57.5
21-68	al 6061-T6		.600	.0127-.5	18.5
21-69	steel 1018		.996	.0127-.5	18.0
22-70	al 6061-T6	338.02-1109	1.663	.0254-1.	10.5
22-71	al 6061-T6	338.02-1109	.995	.0127-.5	62.0(hit)
23-72	al 6061-T6	354.18-1162	1.663	.0254-1.	7.0
23-73	al 6061-T6		1.001	.0127-.5	40.0
24-74	al 6061-T6	370.33-1215	1.657	.0254-1.	8.0
24-75	al 6061-T6		1.002	.0127-.5	35.5
25-76	al 6061-T6	386.49-1268	1.001	.0127-.5	27.0
25-77	al 6061-T6		1.000	.0095-.375	65.5
26-78	al 6061-T6	402.64-1321	.998	.0127-.5	22.5
26-79	al 6061-T6		.999	.0095-.375	hit
27-80	al 6061-T6	418.80-1374	1.004	.0127-.5	18.0
27-81	al 6061-T6		1.005	.0095-.375	44.0
28-82	al 6061-T6	434.94-1427	1.000	.0095-.375	45.0
28-83	al 6061-T6		.800	.0064-.25	67.0
29-84	al 6061-T6	451.10-1480	1.000	.0095-.375	38.0
29-85	al 6061-T6		.801	.0064-.25	50.0
29-86	al 6061-T6		.702	.0064-.25	44.0
29-87	al 6061-T6		.700	.0064-.25	44.0
30-88	al 6061-T6	473.96-1555	1.000	.0095-.375	28.5
30-89	al 6061-T6		.802	.0064-.25	46.5
31-90	al 6061-T6	493.47-1619	1.002	.0095-.375	26.5
31-91	al 6061-T6		.805	.0064-.25	37.0
32-92	al 6061-T6	519.68-1705	.804	.0064-.25	28.0
32-93	wire stand				
33-94	al 6061-T6	542.54-1780	.803	.0064-.25	24.5
33-95	wire stand				
34-96	al 6061-T6	565.40-1855	.804	.0064-.25	21.0
34-97	wire stand				
35-98	al 6061-T6	588.26-1930	1.006	.0064-.25	27.0

Table A–1(continued)

Station and Cant. Number	Type	Distance (m) - (ft)	Length (m)	Diameter (m) - (in)	Bend Angle (°)
35-99	wire stand				
36-100	wire stand	626.36-2055			
36-101	al 6061-T6		1.002	.0064-.25	21.0
37-102	wire stand	664.46-2180			
37-103	wire stand				
37-104	wire stand				
37-105	al 6061-T6		1.004	.0064-.25	10.0
38-106	wire stand	698.75-2293			
38-107	wire stand				
39-108	wire stand	733.04-2405			
39-109	wire stand				
40-110	wire stand	767.33-2518			
40-111	wire stand				
41-112	wire stand	801.62-2630			
41-113	wire stand				
42-114	wire stand	835.91-2743			
42-115	wire stand				
43-116	wire stand	870.20-2855			
43-117	wire stand				
44-118	wire stand	904.49-2968			
44-119	wire stand				
45-120	wire stand	938.78-3080			
45-121	wire stand				

†"s" indicates a cantilever which was sheared off.

‡90^{+} indicates a cantilever which was bent through an angle of at least 90°.

Wire stands supported several wire cantilevers. The data for these cantilevers are presented in table A–2.

Table A.2: WIRE STAND POSITIONS, TYPE AND RESULTS:MINOR UNCLE

Station 32 number 93: G.Z. distance=519.68 m (1705 ft)

Wire Number	Type	Length (m)	Diameter (mm)	Bend Angle (°)	comments
1	al 4043	.15	1.55	39.0	hit
2	al 5056	.20	1.55	35.0	hit
3	solder	.04	1.0	45.0	
4	solder	.04	1.0	43.0	
5	solder	.04	1.0	46.0	
6	al 4043	.15	1.55	51.0	
7	al 5056	.20	1.55	34.0	

Station 33 number 95: G.Z. distance=542.54 m (1780 ft)

Wire Number	Type	Length (m)	Diameter (mm)	Bend Angle (°)	comments
1	al 4043	.15	1.55	34.0	
2	al 5056	.20	1.55	30.0	
3	solder	.04	1.0	46.0	
4	solder	.04	1.0	41.0	
5	solder	.04	1.0	42.5	
6	al 4043	.15	1.55	42.0	
7	al 5056	.20	1.55	30.0	

Table A–2(continued)

Station 34 number 97: G.Z. distance=565.40 m (1855 ft)

Wire Number	Type	Length (m)	Diameter (mm)	Bend Angle (°)	comments
1	graphite	.056	0.5	na	broken
2	graphite	.053	0.5	na	broken
3	graphite	.051	0.5	na	broken
4	graphite	.0475	0.5	na	broken
5	graphite	.045	0.5	na	broken
6	graphite	.043	0.5	na	broken
7	graphite	.040	0.5	na	broken
8	graphite	.038	0.5	na	broken
9	graphite	.035	0.5	na	broken
10	graphite	.033	0.5	na	
11	graphite	.030	0.5	na	
12	graphite	.028	0.5	na	
13	graphite	.025	0.5	na	broken
14	graphite	.0225	0.5	na	
15	graphite	.021	0.5	na	broken

Station 35 number 99: G.Z. distance=588.26 m (1930 ft)

Wire Number	Type	Length (m)	Diameter (mm)	Bend Angle (°)	comments
1	al 4043	.15	1.55	20.0	
2	al 5056	.20	1.55	20.5	
3	solder	.04	1.0	16.0	
4	solder	.04	1.0	15.0	
5	solder	.04	1.0	17.0	
6	al 4043	.15	1.55	20.5	
7	al 5056	.20	1.55	19.0	

Table A–2(continued)

Station 36 number 100: G.Z. distance=626.36 m (2055 ft)

Wire Number	Type	Length (m)	Diameter (mm)	Bend Angle (°)	comments
1	graphite	.055	0.5	na	broken
2	graphite	.0525	0.5	na	broken
3	graphite	.050	0.5	na	broken
4	graphite	.0475	0.5	na	broken
5	graphite	.045	0.5	na	broken
6	graphite	.0425	0.5	na	broken
7	graphite	.040	0.5	na	broken
8	graphite	.0375	0.5	na	
9	graphite	.035	0.5	na	
10	graphite	.0325	0.5	na	
11	graphite	.030	0.5	na	
12	graphite	.0275	0.5	na	
13	graphite	.025	0.5	na	
14	graphite	.0225	0.5	na	
15	graphite	.020	0.5	na	

Station 37 number 102: G.Z. distance=664.46 m (2180 ft)

Wire Number	Type	Length (m)	Diameter (mm)	Bend Angle (°)	comments
1	graphite	.065	0.5	na	broken
2	graphite	.0625	0.5	na	broken
3	graphite	.060	0.5	na	broken
4	graphite	.0575	0.5	na	broken
5	graphite	.055	0.5	na	broken
6	graphite	.0525	0.5	na	broken
7	graphite	.050	0.5	na	broken
8	graphite	.0470	0.5	na	broken
9	graphite	.045	0.5	na	
10	graphite	.0425	0.5	na	
11	graphite	.040	0.5	na	
12	graphite	.0375	0.5	na	
13	graphite	.035	0.5	na	broken
14	graphite	.0325	0.5	na	broken
15	graphite	.030	0.5	na	

Table A–2(continued)

Station 37 number 103: G.Z. distance=664.46 m (2180 ft)

Wire Number	Type	Length (m)	Diameter (mm)	Bend Angle (°)	comments
1	al 4043	.15	1.55	0.0	
2	al 5056	.20	1.55	6.0	
3	solder	.04	1.0	0.0	
4	solder	.04	1.0	0.0	
5	solder	.04	1.0	0.0	
6	al 4043	.15	1.55	0.0	
7	al 5056	.20	1.55	6.5	

Station 37 number 104: G.Z. distance=664.46 m (2180 ft)

Wire Number	Type	Length (m)	Diameter (mm)	Bend Angle (°)	comments
1	al 4043	.25	1.55	38.0	
2	al 5056	.25	1.55	11.0	
3	solder	.07	1.0	90^+	
4	solder	.07	1.0	90^+	
5	solder	.07	1.0	90^+	
6	al 4043	.25	1.55	39.0	
7	al 5056	.25	1.55	15.0	

Station 38 number 106: G.Z. distance=698.75 m (2293 ft)

Wire Number	Type	Length (m)	Diameter (mm)	Bend Angle (°)	comments
1	al 4043	.25	1.55	37.0	
2	al 5056	.25	1.55	10.0	
3	solder	.07	1.0	67.0	
4	solder	.07	1.0	69.0	
5	solder	.07	1.0	69.0	
6	al 4043	.25	1.55	34.0	
7	al 5056	.25	1.55	10.0	

Table A–2(continued)

Station 38 number 107: G.Z. distance=698.75 m (2293 ft)

Wire Number	Type	Length (m)	Diameter (mm)	Bend Angle (°)	comments
1	graphite	.075	0.5	na	broken
2	graphite	.073	0.5	na	broken
3	graphite	.070	0.5	na	broken
4	graphite	.0675	0.5	na	broken
5	graphite	.065	0.5	na	broken
6	graphite	.0625	0.5	na	broken
7	graphite	.060	0.5	na	broken
8	graphite	.0570	0.5	na	broken
9	graphite	.055	0.5	na	broken
10	graphite	.0525	0.5	na	broken
11	graphite	.050	0.5	na	$\frac{1}{2}$ broken
12	graphite	.0475	0.5	na	
13	graphite	.045	0.5	na	
14	graphite	.0425	0.5	na	
15	graphite	.040	0.5	na	

Station 39 number 108: G.Z. distance=733.04 m (2405 ft)

Wire Number	Type	Length (m)	Diameter (mm)	Bend Angle (°)	comments
1	al 4043	.25	1.55	28.0	
2	al 5056	.25	1.55	8.0	
3	solder	.07	1.0	51.0	
4	solder	.07	1.0	50.0	
5	solder	.07	1.0	54.0	
6	al 4043	.25	1.55	19.0	
7	al 5056	.25	1.55	5.0	

Table A–2(continued)

Station 39 number 109: G.Z. distance=733.04 m (2405 ft)

Wire Number	Type	Length (m)	Diameter (mm)	Bend Angle (°)	comments
1	al 4043	.225	1.55	12.5	
2	al 5056	.225	1.55	3.5	
3	solder	.07	1.0	53.5	
4	solder	.07	1.0	55.0	
5	solder	.07	1.0	50.0	
6	al 4043	.225	1.55	15.0	
7	al 5056	.225	1.55	3.5	

Station 40 number 110: G.Z. distance=767.33 m (2518 ft)

Wire Number	Type	Length (m)	Diameter (mm)	Bend Angle (°)	comments
1	graphite	.075	0.5	na	broken
2	graphite	.0725	0.5	na	broken
3	graphite	.070	0.5	na	broken
4	graphite	.0675	0.5	na	broken
5	graphite	.065	0.5	na	broken
6	graphite	.0625	0.5	na	broken
7	graphite	.060	0.5	na	broken
8	graphite	.0570	0.5	na	$\frac{1}{2}$ broken
9	graphite	.055	0.5	na	
10	graphite	.0525	0.5	na	
11	graphite	.050	0.5	na	
12	graphite	.0475	0.5	na	
13	graphite	.045	0.5	na	
14	graphite	.0425	0.5	na	
15	graphite	.040	0.5	na	

Table A–2(continued)

Station 40 number 111: G.Z. distance=767.33 m (2518 ft)

Wire Number	Type	Length (m)	Diameter (mm)	Bend Angle (°)	comments
1	al 4043	.25	1.55	14.0	
2	al 5056	.25	1.55	4.0	
3	solder	.07	1.0	44.0	
4	solder	.07	1.0	45.0	
5	solder	.07	1.0	40.0	
6	al 4043	.25	1.55	21.0	
7	al 5056	.25	1.55	4.0	

Station 41 number 112: G.Z. distance=801.62 m (2630 ft)

Wire Number	Type	Length (m)	Diameter (mm)	Bend Angle (°)	comments
1	al 4043	.25	1.55	6.0	
2	al 5056	.25	1.55	3.0	
3	solder	.07	1.0	27.5	
4	solder	.07	1.0	27.0	
5	solder	.07	1.0	30.0	
6	al 4043	.25	1.55	7.5	
7	al 5056	.25	1.55	3.0	

Station 41 number 113: G.Z. distance=801.62 m (2630 ft)

Wire Number	Type	Length (m)	Diameter (mm)	Bend Angle (°)	comments
1	solder	.08	1.0	59.0	sagged ?
2	solder	.08	1.0	56.0	sagged ?
3	solder	.08	1.0	67.0	sagged ?
4	solder	.08	1.0	61.5	sagged ?
5	solder	.08	1.0	58.5	sagged ?
6	solder	.08	1.0	56.0	sagged ?
7	solder	.08	1.0	55.0	sagged ?

Table A–2(continued)

Station 42 number 114: G.Z. distance=835.91 m (2743 ft)

Wire Number	Type	Length (m)	Diameter (mm)	Bend Angle (°)	comments
1	graphite	.075	0.5	na	broken
2	graphite	.0725	0.5	na	broken
3	graphite	.070	0.5	na	
4	graphite	.0675	0.5	na	
5	graphite	.065	0.5	na	
6	graphite	.0625	0.5	na	
7	graphite	.060	0.5	na	
8	graphite	.0570	0.5	na	
9	graphite	.055	0.5	na	
10	graphite	.0525	0.5	na	
11	graphite	.050	0.5	na	
12	graphite	.0475	0.5	na	
13	graphite	.045	0.5	na	
14	graphite	.0425	0.5	na	
15	graphite	.040	0.5	na	

Station 42 number 115: G.Z. distance=835.91 m (2743 ft)

Wire Number	Type	Length (m)	Diameter (mm)	Bend Angle (°)	comments
1	al 4043	.25	1.55	9.0	
2	al 5056	.25	1.55		hit
3	solder	.07	1.0		hit
4	solder	.07	1.0	14.5	
5	solder	.07	1.0	19.0	
6	al 4043	.25	1.55	6.5	
7	al 5056	.25	1.55	2.0	

Table A–2(continued)

Station 43 number 116: G.Z. distance=870.2 m (2855 ft)

Wire Number	Type	Length (m)	Diameter (mm)	Bend Angle (°)	comments
1	al 4043	.25	1.55	4.0	
2	al 5056	.25	1.55	0.0	
3	solder	.07	1.0	12.5	
4	solder	.07	1.0	12.0	
5	solder	.07	1.0	12.0	
6	al 4043	.25	1.55	5.0	
7	al 5056	.25	1.55	0.0	

Station 43 number 117: G.Z. distance=870.20 m (2855 ft)

Wire Number	Type	Length (m)	Diameter (mm)	Bend Angle (°)	comments
1	solder	.08	1.0	37.0	sagged ?
2	solder	.08	1.0	32.0	sagged ?
3	solder	.08	1.0	37.0	sagged ?
4	solder	.08	1.0	37.0	sagged ?
5	solder	.08	1.0	40.0	sagged ?
6	solder	.08	1.0	42.0	sagged ?
7	solder	.08	1.0	40.0	sagged ?

Station 44 number 118: G.Z. distance=904.49 m (2968 ft)

Wire Number	Type	Length (m)	Diameter (mm)	Bend Angle (°)	comments
1	al 4043	.25	1.55	2.0	
2	al 5056	.25	1.55	0.0	
3	solder	.07	1.0	10.0	
4	solder	.07	1.0	9.0	
5	solder	.07	1.0	10.0	
6	al 4043	.25	1.55	5.0	
7	al 5056	.25	1.55	0.0	

Table A–2(continued)

Station 44 number 119: G.Z. distance=904.49 m (2968 ft)

Wire Number	Type	Length (m)	Diameter (mm)	Bend Angle (°)	comments
1	solder	.08	1.0	35.0	sagged ?
2	solder	.08	1.0	30.0	sagged ?
3	solder	.08	1.0	30.0	sagged ?
4	solder	.08	1.0	28.0	sagged ?
5	solder	.08	1.0	27.0	sagged ?
6	solder	.08	1.0	26.5	sagged ?
7	solder	.08	1.0	33.5	sagged ?

Station 45 number 120: G.Z. distance=938.78 m (3080 ft)

Wire Number	Type	Length (m)	Diameter (mm)	Bend Angle (°)	comments
1	solder	.08	1.0	24.0	sagged ?
2	solder	.08	1.0	26.0	sagged ?
3	solder	.08	1.0	16.0	sagged ?
4	solder	.08	1.0	19.0	sagged ?
5	solder	.08	1.0	15.0	sagged ?
6	solder	.08	1.0	16.0	sagged ?
7	solder	.08	1.0	22.0	sagged ?

Station 45 number 121: G.Z. distance=938.78 m (3080 ft)

Wire Number	Type	Length (m)	Diameter (mm)	Bend Angle (°)	comments
1	al 4043	.30	1.55	5.0	
2	al 4043	.30	1.55	4.0	
3	al 4043	.30	1.55	5.0	
4	al 4043	.30	1.55	6.0	
5	al 4043	.30	1.55	7.0	
6	al 4043	.30	1.55	7.0	
7	al 4043	.30	1.55	5.0	hit?

‡ sagged means the wire may have deformed under its own weight before it could be measured.

Table A.3: RESULTS FOR HORIZONTAL CANTILEVERS:MINOR UNCLE

50 psi station. Distance from GZ = 218 m (718 ft), material: $\frac{1}{2}$in diam. steel 1018

Wire Number	Height (m)	Length		Bend Angle(°)		Dust abrasion
		left (cm)	right (cm)	left	right	
1	1.43	34.7	34.9	44.0	42.5	
2	1.23	34.8	34.9	42.5	42.5	
3	1.03	34.7	34.8	42.5	41.5	max extent
4	.83	34.7	34.7	41.5	42.0	
5	.63	34.6	34.7	41.0	43.0	
6	.43	34.7	34.7	42.0	42.5	
7	.23	34.7	34.7	43.5	42.0	max abrasion
8	.03	34.9	34.8	11.0	13.5	

30 psi station. Distance from GZ = 270 m (887 ft), material: $\frac{1}{2}$in diam. steel 1018

Wire Number	Height (m)	Length		Bend Angle(°)		Dust Abrasion
		left (cm)	right (cm)	left	right	
1	1.43	71.0	69.9	35.0	38.0	
2	1.23	70.5	69.9	36.0	38.0	
3	1.03	69.9	69.8	36.0	38.0	max extent
4	.83	69.9	69.8	38.0	36.5	
5	.63	69.7	69.8	39.0	36.5	
6	.43	69.8	69.8	39.0	34.5	
7	.23	69.9	69.9	39.0	32.5	max abrasion
8	.03	69.9	70.0	11.0	6.0	

20 psi station. Distance from GZ = 321 m (1058 ft), material: $\frac{1}{2}$in diam. al 6061

Wire Number	Height (m)	Length		Bend Angle(°)		Dust Abrasion
		left (cm)	right (cm)	left	right	
1	1.43	71.0	59.9	36.0	23.5	
2	1.23	69.9	59.9	36.0	24.0	
3	1.03	69.7	59.8	42.0	26.0	max extent
4	.83	69.6	59.8	40.0	28.0	
5	.63	69.6	59.9	39.0	26.0	
6	.43	69.6	59.8	37.0	24.0	max abrasion
7	.23	69.7	59.9	38.0	25.0	
8	.03	69.9	59.9	11.0	9.5	

Table A–3(continued)

10 psi station. Distance from GZ = 451 m (1478 ft), material: $\frac{3}{16}$in diam. al 4043

Wire Number	Height (m)	Length		Bend Angle(°)		Dust Abrasion
		left (cm)	right (cm)	left	right	
1	1.43	29.8	39.7	32.0	60.0	
2	1.33	29.8	39.7	33.0	63.0	
3	1.23	29.8	39.7	33.0	63.0	
4	1.13	29.7	39.7	32.5	63.0	
5	1.03	29.7	39.7	35.0	64.5	
6	.93	29.6	39.7	34.0	64.0	
7	.83	29.6	39.7	35.0	65.0	max extent
8	.73	29.6	39.7	34.0	64.0	
9	.63	29.6	39.7	33.0	64.0	
10	.53	29.6	39.7	34.0	65.0	
11	.43	29.6	39.7	35.5	63.0	
12	.33	29.6	39.7	hit	63.0	
13	.23	29.7	39.7	hit	64.0	
14	.13	29.8	39.7	hit	62.0	
15	.03	29.8	39.7	17.0	38.0	

5 psi station. Distance from GZ = 664 m (2181 ft), material: $\frac{1}{16}$in diam. al 4043

Wire Number	Height (m)	Length		Bend Angle(°)		Dust Abrasion
		left (cm)	right (cm)	left	right	
1	1.43	20.0	25.0	29.0	36.0	
2	1.33	20.0	25.0	29.5	40.0	
3	1.23	20.0	25.0	30.0	42.0	
4	1.13	20.0	25.0	30.5	43.0	
5	1.03	20.0	25.0	25.0	43.0	
6	.93	20.0	25.0	24.5	42.0	
7	.83	20.0	25.0	25.5	47.5	
8	.73	20.0	25.0	24.0	48.5	
9	.63	20.0	25.0	25.0	48.0	
10	.53	20.0	25.0	26.0	45.0	
11	.43	20.0	25.0	24.0	42.0	
12	.33	20.0	25.0	26.0	42.0	
13	.23	20.0	25.0	30.0	48.0	
14	.13	20.0	25.0	31.0	52.0	
15	.03	20.0	25.0	30.0	52.0	

Table A–3(continued)

RESULTS FOR CANTILEVERS MOUNTED ROUGH GROUND

30 psi station. Distance from GZ = 270 m (887 ft), material: $\frac{1}{2}$in diam. steel 1018

Wire Number	Height (m)	Length		Bend Angle(°)		Dust Abrasion
		left (cm)	right (cm)	left	right	
1	1.03	69.9		48.0		
2	.83	69.9		47.5		
3	.63	69.9		49.0		
4	.43	69.9		49.0		
5	.23	69.9		44.0		
6	.03	69.9		17.0		

10 psi station. Distance from GZ = 451 m (1478 ft), material: $\frac{3}{16}$in diam. al 4043

Wire Number	Height (m)	Length		Bend Angle(°)		Dust Abrasion
		left (cm)	right (cm)	left	right	
1	1.43	39.7		64.0		
2	1.23	39.7		66.0		
3	1.03	39.7		67.0		
4	.83	39.7		70.0		
5	.63	39.7		69.9		
6	.43	39.7		hit		
7	.23	39.7		hit		
8	.03	39.7		28.0		

Appendix B

DISTANT IMAGE:cantilever data

Table B.1: CANTILEVER POSITIONS AND TYPE:DISTANT IMAGE

Station and Cant. Number	Type	Distance (m) - (ft)	Length (m)	Diameter (m) - (in)	Bend Angle (°)
1-1	steel 1018	117.77-386.39	.401	.0254-1.	66.0
1-2	al 6061-T6	117.75-386.33	.201	.0254-1.	s†
1-3	al 6061-T6	117.76-386.36	.400	.0254-1.	s
1-4	al 6061-T6	117.81-386.50	.300	.0254-1.	s
1-5	al 6061-T6	117.77-386.40	.148	.0127-.5	90^{+}‡
1-6	al 6061-T6	117.82-386.55	.228	.0191-.75	90^{+}
1-7	steel 1018	117.83-386.59	.398	.0191-.75	90^{+}
2-8	al 6061-T6	120.83-396.43	.298	.0254-1.	s
2-9	al 6061-T6	120.76-396.18	.225	.0191-.75	86.5
3-10	al 6061-T6	123.69-405.82	.222	.0191-.75	84.5
3-11	al 6061-T6	123.81-406.20	.301	.0254-1.	s
4-12	al 6061-T6	126.87-416.24	.223	.0191-.75	86.5
4-13	al 6061-T6	126.83-416.12	.292	.0254-1.	s
5-14	al 6061-T6	129.95-426.35	.224	.0191-.75	84.0
5-15	al 6061-T6	129.98-426.45	.298	.0254-1.	s
6-16	al 6061-T6	132.97-436.24	.150	.0127-.5	90^{+}
6-17	al 6061-T6	132.94-436.17	.222	.0191-.75	77.5
6-18	steel 1018	132.98-436.28	.500	.0254-1.	73.5
6-19	al 6061-T6	132.98-436.28	.303	.0254-1.	90^{+}
6-20	steel 1018	132.94-436.17	.200	.0127-.5	54.0
6-21	steel 1018	132.97-436.25	.296	.0191-.75	55.5
6-22	steel 1018	132.93-436.11	.400	.0191-.75	86.0

Table B–1(continued)

Station and Cant. Number	Type	Distance (m) - (ft)	Length (m)	Diameter (m) - (in)	Bend Angle (°)
7-23	al 6061-T6	139.95-459.15	.227	.0191-.75	81.0
7-24	steel 1018	140.05-459.45	.401	.0191-.75	85.5
8-25	steel 1018	147.00-482.28	.398	.0191-.75	79.0
8-26	al 6061-T6	147.00-482.28	.226	.0191-.75	73.5
9-27	steel 1018	153.99-505.21	.399	.0191-.75	71.5
9-28	al 6061-T6	153.97-505.16	.228	.0191-.75	56.5
10-29	steel 1018	160.99-528.17	.513	.0254-1.	run over
10-30	al 6061-T6	161.03-528.31	.303	.0127-.5	90^+
10-31	al 6061-T6	161.03-528.33	.752	.0254-1.	s
10-32	al 6061-T6	161.02-528.29	.504	.0191-.75	90^+
10-33	al 6061-T6	161.02-528.29	.201	.0127-.5	85.0
10-34	steel 1018	161.03-528.31	.404	.0191-.75	67.0
10-35	steel 1018	160.98-528.14	.499	.0191-.75	87.5
10-36	al 6061-T6	160.98-528.16	.223	.0191-.75	41.5
10-37	steel 1018	160.98-528.16	.505	.0254-1.	46.5
11-38	steel 1018	176.22-578.15	.399	.0191-.75	49.0
11-39	al 6061-T6	176.23-578.19	.398	.0191-.75	86.0
12-40	steel 1018	189.69-622.33	.400	.0191-.75	33.5
12-41	al 6061-T6	189.68-622.31	.403	.0191-.75	85.0
13-42	steel 1018	203.99-669.27	.400	.0191-.75	21.0
13-43	al 6061-T6	203.94-669.11	.410	.0191-.75	75.0
14-44	al 6061-T6	218.33-716.29	.605	.0127-.5	80.0
14-45	al 6061-T6	218.33-716.31	.504	.0127-.5	88.5
14-46	al 6061-T6	218.25-716.04	.304	.0127-.5	71.0
14-47	steel 1018	218.35-716.37	.400	.0191-.75	6.5
14-48	al 6061-T6	218.35-716.36	.505	.0191-.75	77.0
14-49	al 6061-T6	218.33-716.29	.399	.0191-.75	46.0
14-50	al 6061-T6	218.30-716.21	.754	.0254-1.	61.5
14-51	steel 1018	218.30-716.20	.505	.0254-1.	2.5
15-52	al 6061-T6	244.22-801.24	.605	.0127-.5	90^+
15-53	al 6061-T6	244.28-801.43	.501	.0191-.75	40.0
16-54	al 6061-T6	270.20-886.49	.500	.0191-.75	10.5
16-55	al 6061-T6	270.15-886.31	.596	.0127-.5	81.5
16-56	al 6061-T6	270.16-886.34	1.700	.0254-1.	s
17-57	al 6061-T6	296.04-971.27	1.648	.0254-1.	42.5
17-58	al 6061-T6	296.05-971.28	.504	.0191-.75	2.5
18-59	al 4043	321.88-1056.05	.400	.0064-.25	82.0
18-60	al 6061-T6	321.87-1055.99	1.003	.0127-.5	83.5

Table B–1(continued)

Station and Cant. Number	Type	Distance (m) - (ft)	Length (m)	Diameter (m) - (in)	Bend Angle (°)
18-61	al 6061-T6	321.84-1055.89	1.666	.0254-1.	23.5
18-62	al 4043	321.88-1056.05	.300	.0064-.25	75.5
18-63	al 6061-T6	321.94-1056.23	.608	.0127-.5	33.5
18-64	al 6061-T6	321.95-1056.26	.502	.0191-.75	1.0
18-65	al 4043	321.85-1055.95	.400	.0064-.25	90^+
18-66	al 6061-T6	321.89-1056.07	1.003	.0095-.375	90^+
18-67	al 4043	321.85-1055.94	.200	.0064-.25	23.5
18-68	steel 1018	321.91-1056.15	.504	.0127-.5	1.0
18-69	al 4043	321.86-1055.97	.200	.0064-.25	33.0
18-70	al 6061-T6	321.93-1056.19	.447	.0064-.25	s
18-71	al 6061-T6	321.91-1056.12	.502	.0095-.375	43.5
18-72	al 4043	321.87-1056.02	.300	.0064-.25	78.0
18-73	steel 1018	321.93-1056.21	1.000	.0127-.5	27.5
19-74	al 6061-T6	354.19-1162.05	1.664	.0254-1.	13.5
19-75	al 6061-T6	354.28-1162.33	.596	.0127-.5	18.0
20-76	steel 1018	386.50-1268.06	.998	.0127-.5	6.5
20-77	al 6061-T6	386.51-1268.08	.610	.0127-.5	8.0
21-78	al 6061-T6	418.83-1374.12	.603	.0127-.5	1.0
21-79	al 6061-T6	418.78-1373.94	.654	.0064-.25	56.0
22-80	ree-bar	451.12-1480.04	1.880	.0159-.625	0.0
22-81	al 6061-T6	451.13-1480.10	1.000	.0064-.25	90^+
22-82	wire stand	451.16-1480.19			
22-83	galv. steel	451.06-1479.86	1.681	.0159-.625	7.5
22-84	wire stand	451.08-1479.93			
22-85	wire stand	451.14-1480.13			
22-86	wire stand	451.12-1480.04			
22-87	al 6061-T6	451.11-1480.02	.700	.0064-.25	53.0
22-88	wire stand	451.11-1480.02			
22-89	al 6061-T6	451.15-1480.14	.500	.0064-.25	45.0
22-90	al 6061-T6	451.10-1480.00	1.000	.0095-.375	43.0
23-91	wire stand	493.34-1618.58			
23-92	al 6061-T6	493.39-1618.75	1.000	.0064-.25	90^+
24-93	wire stand	541.27-1775.81			
24-94	al 6061-T6	541.31-1775.95	1.000	.0064-.25	s
25-95	wire stand	588.15-1929.64			
25-96	al 6061-T6	588.21-1929.83	1.000	.0064-.25	24.0
25.5-97	wire stand	633.90-2079.73			

Table B–1(continued)

Station and Cant. Number	Type	Distance (m) - (ft)	Length (m)	Diameter (m) - (in)	Bend Angle (°)
25.5-98	al 6061-T6	633.94-2079.87	1.000	.0064-.25	19.5
26-99	wire stand	664.46-2179.99			
26-100	wire stand	664.42-2179.87			
26-101	wire stand	664.41-2179.81			
26-102	al 4043	664.43-2179.88	.875	.0064-.25	20.0
26-103	al 6061-T6	664.43-2179.90	.500	.0032-.125	8.0
26-104	al 6061-T6	664.44-2179.93	1.000	.0032-.125	40.5
26-105	al 4043	664.40-2179.80	.500	.0032-.125	29.5
26-106	wire stand	664.42-2179.87			
26-107	wire stand	664.41-2179.82			
26-108	wire stand	664.41-2179.81			
27-109	wire stand	732.98-2404.78			
27-110	al 6061-T6	733.02-2404.91	1.000	.0032-.125	47.5
28-111	wire stand	801.55-2629.75			
28-112	al 6061-T6	801.57-2629.83	1.000	.0032-.125	32.0
29-113	wire stand	870.18-2854.91			
29-114	al 6061-T6	870.20-2855.00	1.000	.0032-.125	17.0
30-115	wire stand	938.78-3079.99			
30-116	wire stand	938.74-3079.84			
30-117	wire stand	938.73-3079.83			
30-118	al 4043	938.74-3079.84	.875	.0032-.125	12.0
30-119	al 6061-T6	938.73-3079.83	1.000	.0032-.125	8.0
30-120	al 4043	938.77-3079.96	1.000	.0032-.125	47.5
30-121	wire stand	938.75-3079.88			
30-122	wire stand	938.76-3079.91	1.000	.0032-.125	32.0
30-123	wire stand	938.76-3079.92			

†"s" indicates a cantilever which was sheared off.

‡90^+ indicates a cantilever which was bent through an angle of at least 90°.

Wire stands supported several wire cantilevers. The data for these cantilevers are presented in table B–2.

Table B.2: WIRE STAND POSITIONS, TYPE AND RESULTS:DISTANT IMAGE

Station 22 number 82: G.Z. distance=451.16 m (1480.19 ft)

Wire Number	Type	Length (m)	Diameter (mm)	Bend Angle (°)	comments
1	al 4043	.05	1.55	35.0	hit
2	al 4043	.08	1.55	15.0	hit
3	al 4043	.10	1.55	31.0	
4	al 4043	.15	1.55	79.0	
5	al 4043	.15	1.55	80.0	
6	al 4043	.15	1.55	79.0	
7	al 4043	.15	1.55	79.0	

Station 22 number 84: G.Z. distance=451.08 m (1479.93 ft)

Wire Number	Type	Length (m)	Diameter (mm)	Bend Angle (°)	comments
1	al 5056	.08	1.55	0.0	
2	al 5056	.125	1.55		s†
3	al 5056	.15	1.55	41.0	
4	al 5056	.20	1.55	67.0	
5	al 5056	.15	1.55		hit
6	al 5056	.15	1.55	44.0	
7	al 5056	.15	1.55	44.0	

Station 22 number 85: G.Z. distance=451.14 m (1480.13 ft)

Wire Number	Type	Length (m)	Diameter (mm)	Bend Angle (°)	comments
1	solder	.02	1.0	0.0	
2	solder	.03	1.0	35.0	
3	solder	.03	1.0		hit
4	solder	.035	1.0		hit
5	solder	.04	1.0		hit
6	solder	.0508	1.0		hit
7	solder	.06	1.0		hit

Table B–2(continued)

Station 22 number 86: G.Z. distance=451.12 m (1480.04 ft)

Wire Number	Type	Length (m)	Diameter (mm)	Bend Angle (°)	comments
1	graphite	.117	2.0	na	broken
2	graphite	.074	0.5	na	broken
3	graphite	.108	2.0	na	broken
4	graphite	.064	0.5	na	broken
5	graphite	.0975	2.0	na	broken
6	graphite	.054	0.5	na	broken
7	graphite	.088	2.0	na	broken
8	graphite	.044	0.5	na	broken
9	graphite	.077	2.0	na	broken
10	graphite	.034	0.5	na	broken
11	graphite	.0675	2.0	na	broken
12	graphite	.024	0.5	na	broken
13	graphite	.0575	2.0	na	broken
14	graphite	.014	0.5	na	broken

Station 22 number 88: G.Z. distance=451.11 m (1480.02 ft)

Wire Number	Type	Length (m)	Diameter (mm)	Bend Angle (°)	comments
1	solder	.02	1.0	0.0	sand sprayed
2	solder	.03	1.0	31.0	sand sprayed
3	solder	.03	1.0	42.0	sand sprayed
4	solder	.03	1.0	42.0	sand sprayed
5	solder	.03	1.0	43.0	sand sprayed
6	solder	.03	1.0	42.0	sand sprayed
7	solder	.03	1.0	42.0	sand sprayed

Table B–2(continued)

Station 23 number 91: G.Z. distance=493.34 m (1618.58 ft)

Wire Number	Type	Length (m)	Diameter (mm)	Bend Angle (°)	comments
1	al 4043	.15	1.55	65.0	hit
2	al 5056	.15	1.55	30.0	hit
3	solder	.04	1.0	68.0	
4	solder	.04	1.0	60.0	
5	solder	.04	1.0	67.5	
6	al 4043	.15	1.55	59.0	
7	al 5056	.15	1.55	29.0	

Station 24 number 93: G.Z. distance=541.27 m (1775.81 ft)

Wire Number	Type	Length (m)	Diameter (mm)	Bend Angle (°)	comments
1	al 4043	.15	1.55	49.0	
2	al 5056	.15	1.55	16.5	
3	solder	.04	1.0	47.0	
4	solder	.04	1.0	47.0	
5	solder	.04	1.0	44.0	
6	al 4043	.15	1.55	49.0	
7	al 5056	.15	1.55	17.0	

Station 25 number 95: G.Z. distance=588.15 m (1929.64 ft)

Wire Number	Type	Length (m)	Diameter (mm)	Bend Angle (°)	comments
1	al 4043	.15	1.55	31.0	
2	al 5056	.15	1.55	7.0	
3	solder	.04	1.0	21.0	
4	solder	.04	1.0	21.0	
5	solder	.04	1.0	20.0	
6	al 4043	.15	1.55	33.0	
7	al 5056	.15	1.55	7.0	

Table B–2(continued)

Station 25.5 number 97: G.Z. distance=633.90 m (2079.73 ft)

Wire Number	Type	Length (m)	Diameter (mm)	Bend Angle (°)	comments
1	al 4043	.15	1.55	16.0	
2	al 5056	.15	1.55	2.0	
3	solder	.04	1.0	3.0	
4	solder	.04	1.0	4.0	
5	solder	.04	1.0	2.5	
6	al 4043	.15	1.55	16.0	
7	al 5056	.15	1.55	1.0	

Station 26 number 99: G.Z. distance=664.46 m (2179.99 ft)

Wire Number	Type	Length (m)	Diameter (mm)	Bend Angle (°)	comments
1	al 4043	.10	1.55	0.0	hit
2	al 4043	.15	1.55	3.5	hit
3	al 4043	.20	1.55	18.0	
4	al 4043	.225	1.55	28.0	
5	al 4043	.225	1.55	29.5	
6	al 4043	.225	1.55	28.0	
7	al 4043	.225	1.55	29.0	

Station 26 number 100: G.Z. distance=664.42 m (2179.87 ft)

Wire Number	Type	Length (m)	Diameter (mm)	Bend Angle (°)	comments
1	al 5056	.1	1.55	0.0	platform hit
2	al 5056	.15	1.55	0.0	
3	al 5056	.2	1.55	7.5	
4	al 5056	.225	1.55	12.0	
5	al 5056	.225	1.55	11.5	
6	al 5056	.225	1.55	15.0	
7	al 5056	.225	1.55	14.0	

Table B–2(continued)

Station 26 number 101: G.Z. distance=664.41 m (2179.81 ft)

Wire Number	Type	Length (m)	Diameter (mm)	Bend Angle (°)	comments
1	solder	.07	1.0	77.5	
2	solder	.07	1.0	80.0	
3	solder	.06	1.0	50.0	
4	solder	.06	1.0	53.0	
5	solder	.06	1.0	48.5	
6	solder	.08	1.0	90^+	
7	solder	.08	1.0	90^+	

Station 26 number 106: G.Z. distance=664.42 m (2179.87 ft)

Wire Number	Type	Length (m)	Diameter (mm)	Bend Angle (°)	comments
1	graphite	.014	0.5	na	
2	graphite	.024	0.5	na	
3	graphite	.034	0.5	na	
4	graphite	.044	0.5	na	
5	graphite	.054	0.5	na	broken
6	graphite	.064	0.5	na	broken
7	graphite	.074	0.5	na	broken

Station 26 number 106: G.Z. distance=664.42 m (2179.87 ft)

Wire Number	Type	Length (m)	Diameter (mm)	Bend Angle (°)	comments
1	solder	.0508	1.0	20.0	
2	solder	.0508	1.0	23.5	
3	solder	.0508	1.0	19.0	
4	solder	.0508	1.0	13.5	
5	solder	.0508	1.0	14.0	hit
6	solder	.0508	1.0	18.5	
7	solder	.0508	1.0	21.0	

Table B–2(continued)

Station 26 number 108: G.Z. distance=664.41 m (2179.81 ft)

Wire Number	Type	Length (m)	Diameter (mm)	Bend Angle (°)	comments
1	al 4043	.2	1.55	22.0	
2	al 4043	.2	1.55	23.0	
3	al 4043	.2	1.55	22.0	
4	al 4043	.2	1.55	22.0	
5	al 5056	.2	1.55	8.0	
6	al 5056	.2	1.55	9.0	
7	al 5056	.2	1.55	9.0	

Station 27 number 109: G.Z. distance=732.98 m (2404.78 ft)

Wire Number	Type	Length (m)	Diameter (mm)	Bend Angle (°)	comments
1	al 4043	.225	1.55	17.0	
2	al 5056	.225	1.55	7.0	
3	solder	.07	1.0	44.5	
4	solder	.07	1.0	44.5	
5	solder	.07	1.0	50.0	
6	al 4043	.225	1.55	16.0	
7	al 5056	.225	1.55	7.0	

Station 28 number 111: G.Z. distance=801.55 m (2629.75 ft)

Wire Number	Type	Length (m)	Diameter (mm)	Bend Angle (°)	comments
1	al 4043	.225	1.55	5.0	
2	al 5056	.225	1.55	2.5	
3	solder	.07	1.0	25.5	
4	solder	.07	1.0	22.5	
5	solder	.07	1.0	26.0	
6	al 4043	.225	1.55	4.0	
7	al 5056	.225	1.55	1.5	

Table B–2(continued)

Station 29 number 113: G.Z. distance=870.18 m (2854.91 ft)

Wire Number	Type	Length (m)	Diameter (mm)	Bend Angle (°)	comments
1	al 4043	.225	1.55	4.0	
2	al 5056	.225	1.55	0.0	
3	solder	.07	1.0	15.5	
4	solder	.07	1.0	14.5	
5	solder	.07	1.0	15.0	
6	al 4043	.225	1.55	3.0	
7	al 5056	.225	1.55	1.0	

Station 30 number 115: G.Z. distance=938.78 m (3079.99 ft)

Wire Number	Type	Length (m)	Diameter (mm)	Bend Angle (°)	comments
1	al 4043	.3	1.55	7.0	
2	al 4043	.3	1.55	5.0	
3	al 4043	.3	1.55	4.0	
4	al 4043	.3	1.55	5.0	
5	al 4043	.3	1.55	6.5	
6	al 4043	.3	1.55	5.0	
7	al 4043	.3	1.55	6.5	

Station 30 number 116: G.Z. distance=938.74 m (3079.84 ft)

Wire Number	Type	Length (m)	Diameter (mm)	Bend Angle (°)	comments
1	al 5056	.35	1.55	4.0	
2	al 5056	.35	1.55	4.5	
3	al 5056	.35	1.55	0.0	
4	al 5056	.35	1.55	3.0	
5	al 5056	.35	1.55	2.0	
6	al 5056	.35	1.55	1.5	
7	al 5056	.35	1.55	2.0	

Table B–2(continued)

Station 30 number 117: G.Z. distance=938.73 m (3079.83 ft)

Wire Number	Type	Length (m)	Diameter (mm)	Bend Angle (°)	comments
1	solder	.08	1.0	12.5	
2	solder	.08	1.0	11.5	
3	solder	.08	1.0	11.5	
4	solder	.08	1.0	11.5	
5	solder	.08	1.0	11.5	
6	solder	.08	1.0		hit
7	solder	.08	1.0	12.0	

Station 30 number 121: G.Z. distance=938.75 m (3079.88 ft)

Wire Number	Type	Length (m)	Diameter (mm)	Bend Angle (°)	comments
1	graphite	.014	0.5	na	not broken
2	graphite	.024	0.5	na	not broken
3	graphite	.034	0.5	na	not broken
4	graphite	.044	0.5	na	not broken
5	graphite	.054	0.5	na	not broken
6	graphite	.064	0.5	na	not broken
7	graphite	.074	0.5	na	not broken

Station 30 number 122: G.Z. distance=938.76 m (3079.91 ft)

Wire Number	Type	Length (m)	Diameter (mm)	Bend Angle (°)	comments
1	solder	.1	1.0		sagged‡
2	solder	.1	1.0		sagged
3	solder	.1	1.0		sagged
4	solder	.1	1.0		sagged
5	solder	.1	1.0		sagged
6	solder	.1	1.0		sagged
7	solder	.1	1.0		sagged

Table B–2(continued)

Station 30 number 123: G.Z. distance=938.76 m (3079.92 ft)

Wire Number	Type	Length (m)	Diameter (mm)	Bend Angle (°)	comments
1	al 4043	.35	1.55	7.5	
2	al 4043	.35	1.55	7.5	
3	al 4043	.35	1.55	8.0	
4	al 4043	.35	1.55	5.5	
5	al 4043	.35	1.55	7.0	
6	al 4043	.35	1.55	7.5	
7	al 4043	.35	1.55	18.5	hit?

‡ sagged means the wire may have deformed under its own weight before it could be measured.

Table B.3: RESULTS FOR POLE MOUNTED CANTILEVERS:DISTANT IMAGE

Pole N13. Distance from GZ = 382.24 m (1254.08 ft), material: $\frac{3}{16}$in diam. al 4043

Wire Number	Height (m)	Bend Angle(°)		comments
		0.2 m rods	0.3 m rods	
1	.10	41.0	77.0	
2	.25	43.0	78.0	
3	.41	44.0	82.0	
4	.56	47.0	88.0	erratic bend
5	.71	45.0	78.0	erratic bend
6	.86	46.0	80.0	erratic bend
7	1.01		86.0	erratic bend
8	1.17	46.0		erratic bend
9	1.32	46.0	83.0	erratic bend
10	1.62	46.0		erratic bend
11	1.93	43.0		erratic bend
12	2.23	43.0	83.0	
13	2.54	41.0	77.0	
14	2.84	32.0	67.0	
15	3.15	31.0	72.0	
16	3.45	26.0	70.0	
17	3.76	47.0	80.0	

Table B–3(continued)

Pole N6. Distance from GZ = 533.67 m (1750.87 ft), material: $\frac{3}{16}$in diam. al 4043

Wire Number	Height (m)	Bend Angle(°)		comments
		0.35 m rods	0.5 m rods	
1	.10	23.0	51.0	
2	.25	32.0	54.0	
3	.41	32.0	54.0	
4	.56	27.0	52.0	
5	.71	25.0	54.0	
6	.86	25.0	47.5	
7	1.01	24.0	51.0	erratic bend
8	1.17	34.0	54.0	
9	1.32		53.0	erratic bend
10	1.62	22.0	54.0	erratic bend
11	1.93	20.0		erratic bend
12	2.23	20.0	51.0	
13	2.53	20.0	56.0	
14	2.84	16.0	52.0	
15	3.15	20.0	45.0	
16	3.48	11.0	49.0	

Table B–3(continued)

Pole N7. Distance from GZ = 609.66 m (2000.18 ft), material: $\frac{1}{8}$in diam. al 4043

Wire Number	Height (m)	Bend Angle(°)		comments
		0.3 m rods	0.5 m rods	
1	.10	30.0	46.0	
2	.25	28.0	50.0	erratic bend
3	.41	42.0	50.0	
4	.56	24.0	47.0	
5	.71	18.0	46.5	
6	.86	19.0	46.0	
7	1.01	19.0	48.0	
8	1.17	18.0	45.0	
9	1.32	18.0	47.0	
10	1.62	17.0	48.0	
11	1.93	12.0	34.0	
12	2.23	22.0	41.0	
13	2.54	24.0	38.0	
14	2.84	27.0	31.0	
15	3.15	14.0	36.0	
16	3.45	10.0	42.0	

Table B–3(continued)

Pole N8. Distance from GZ = 685.83 m (2250.10 ft), material: $\frac{1}{8}$in diam. al 4043

Wire Number	Height (m)	Bend Angle(°)		comments
		0.3 m rods	0.5 m rods	
1	.10	32.0		
2	.25	30.0	24.0	
3	.41	4.0	22.0	
4	.56	4.0	25.0	
5	.71	20.0	23.0	
6	.86	15.0	22.0	
7	1.01	10.0	22.0	
8	1.17	20.0	24.0	
9	1.32	10.0	24.0	
10	1.62	9.0	25.0	
11	1.93	11.0	30.0	
12	2.23	27.0	29.0	
13	2.54	23.0	22.0	
14	2.84	13.0	23.0	
15	3.15	5.0	21.0	
16	3.45	hit	24.0	

Appendix C

Elastic-plastic model results

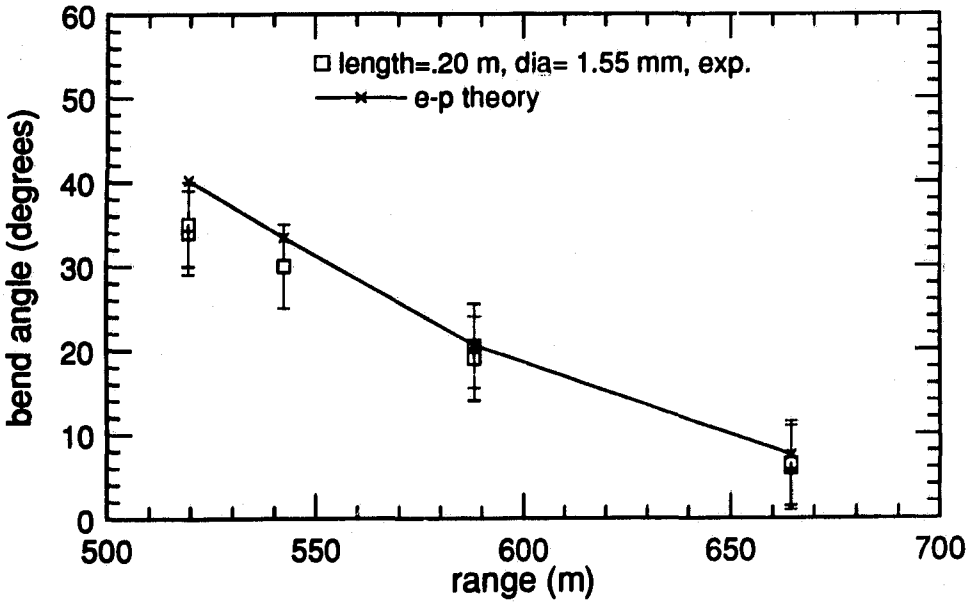

Figure C.1: Experimental and theoretical deformation angle versus range for aluminum 5056 cantilevers at MINOR UNCLE.

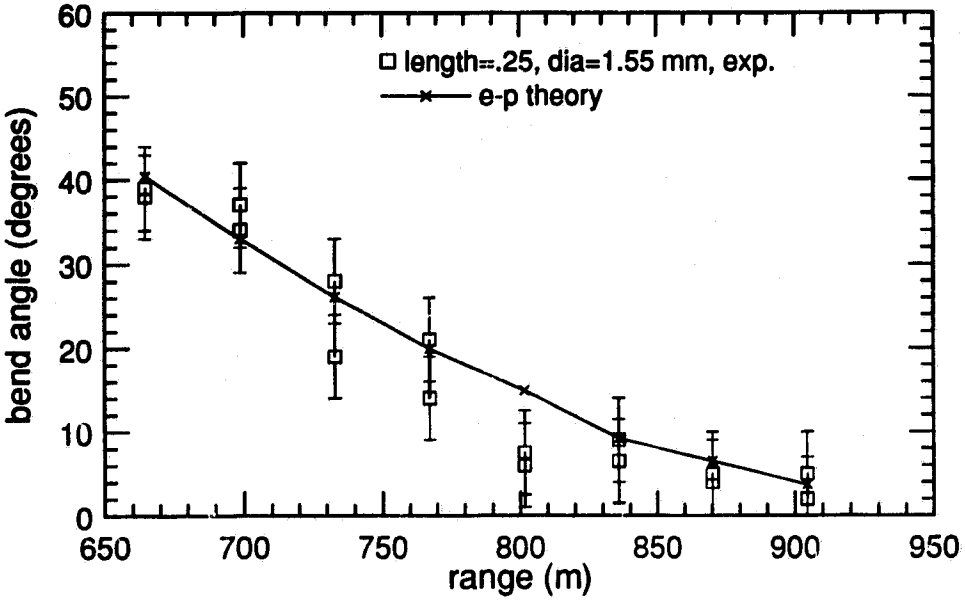

Figure C.2: Experimental and theoretical deformation angle versus range for aluminum 4043 cantilevers at MINOR UNCLE.

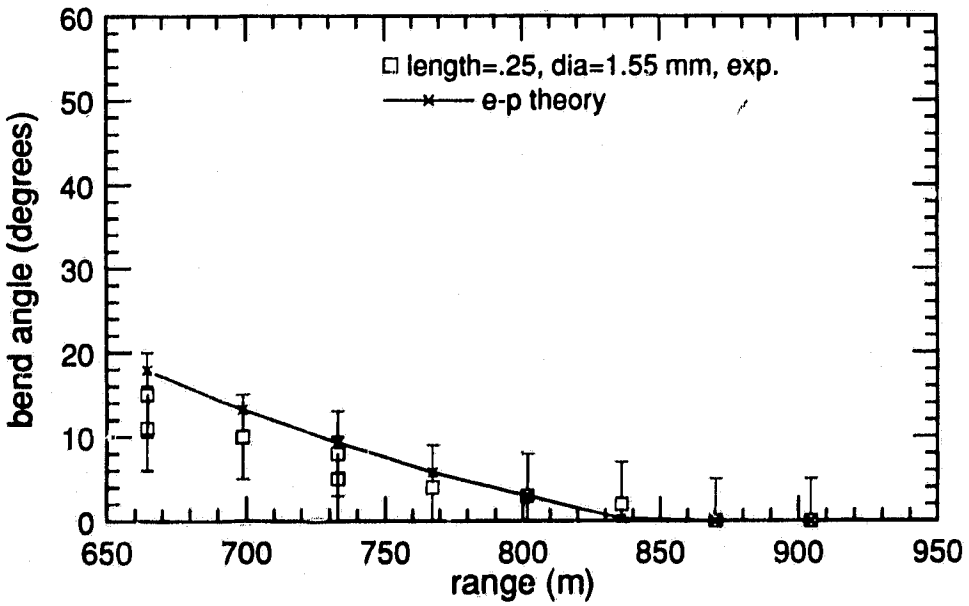

Figure C.3: Experimental and theoretical deformation angle versus range for aluminum 5056 cantilevers at MINOR UNCLE.

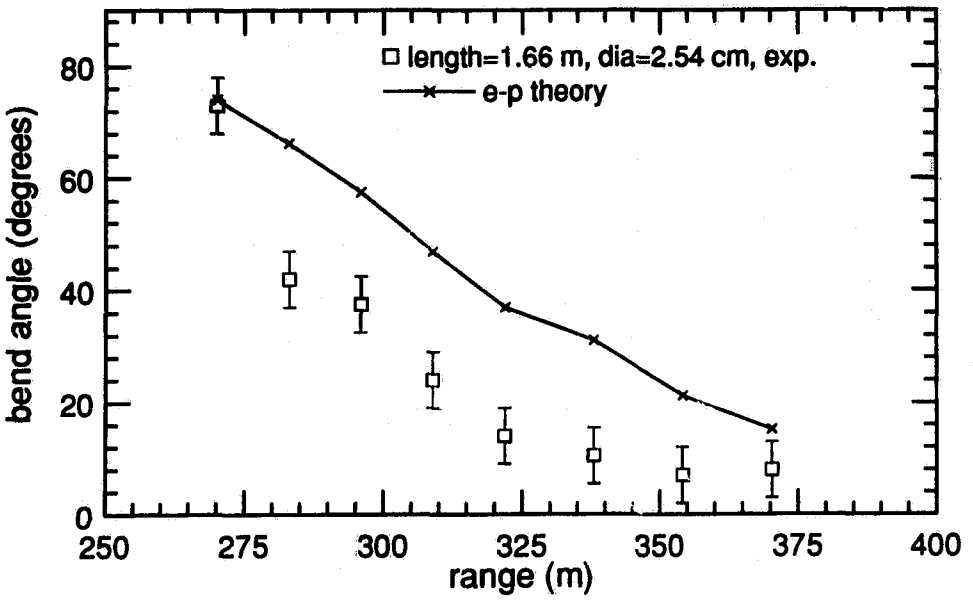

Figure C.4: Experimental and theoretical deformation angle versus range for aluminum 6061 cantilevers at MINOR UNCLE.

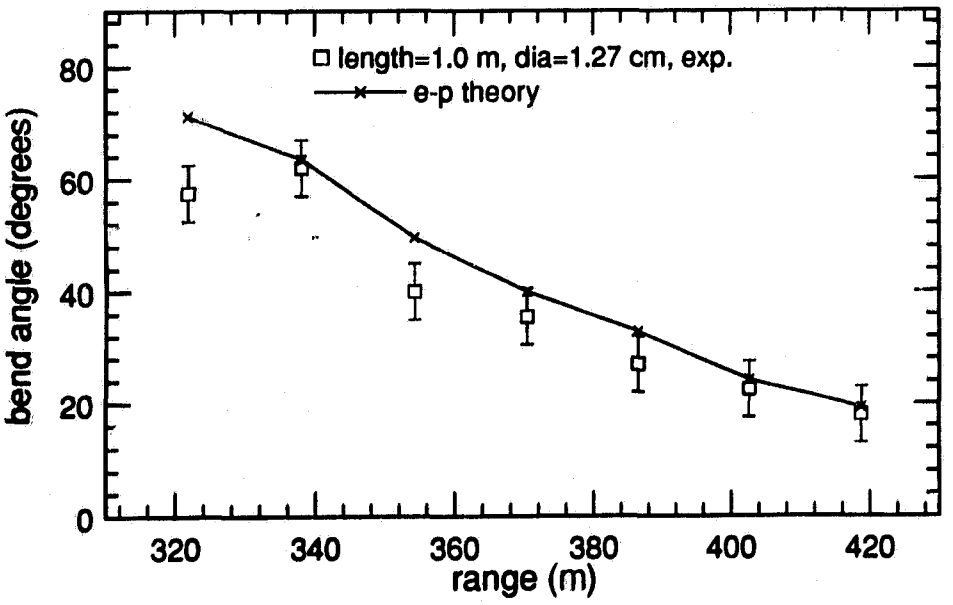

Figure C.5: Experimental and theoretical deformation angle versus range for aluminum 6061 cantilevers at MINOR UNCLE.

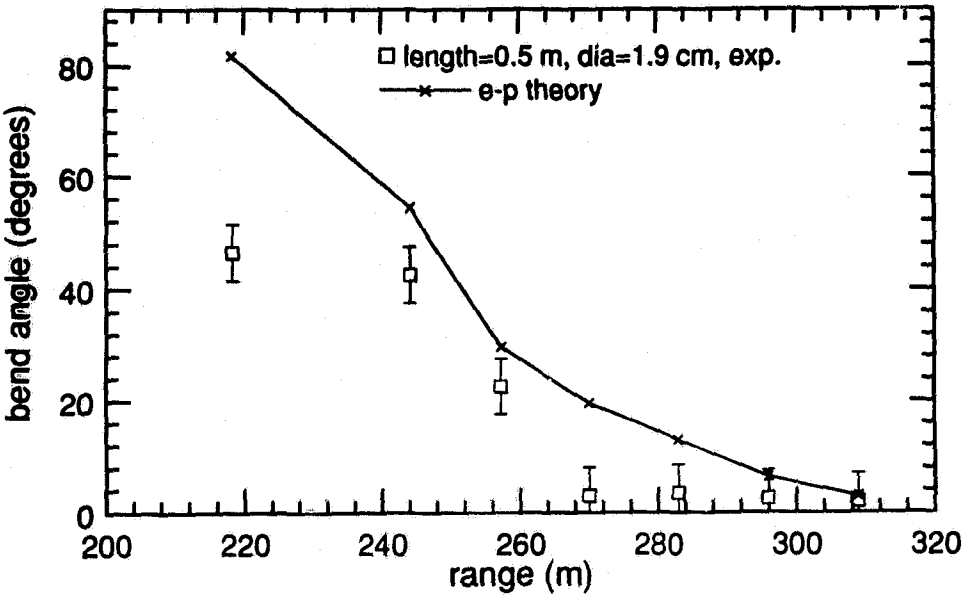

Figure C.6: Experimental and theoretical deformation angle versus range for aluminum 6061 cantilevers at MINOR UNCLE.

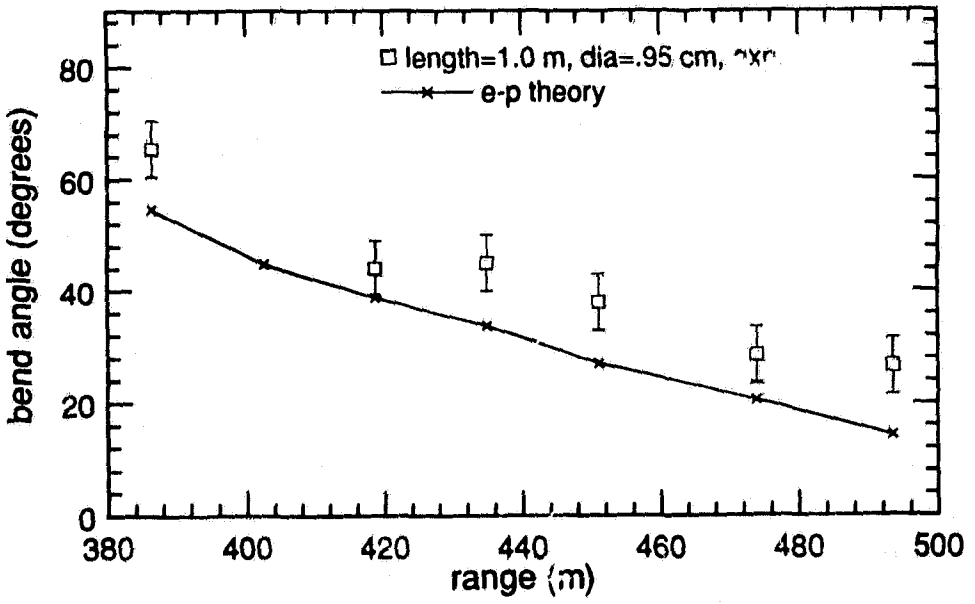

Figure C.7: Experimental and theoretical deformation angle versus range for aluminum 6061 cantilevers at MINOR UNCLE.

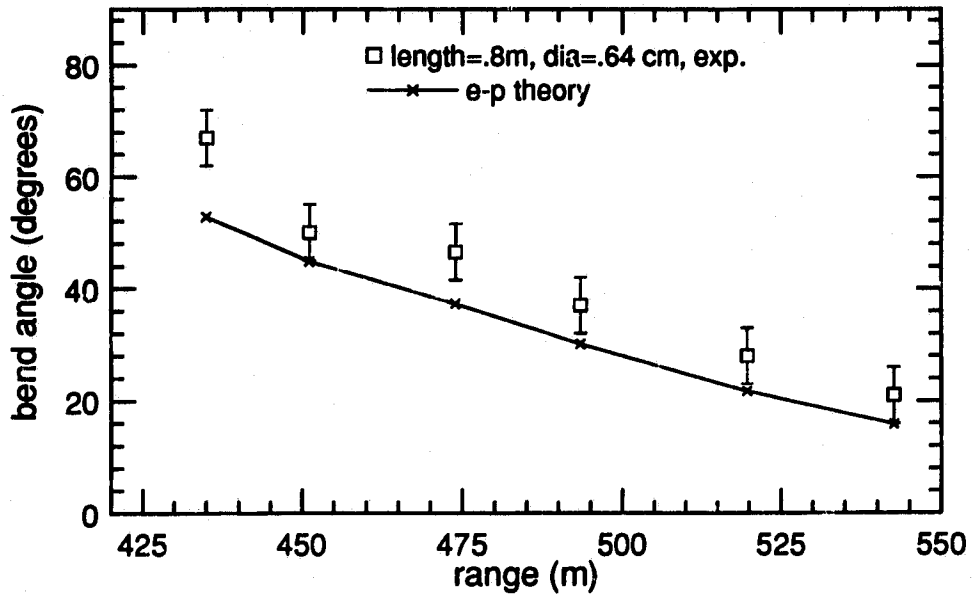

Figure C.8: Experimental and theoretical deformation angle versus range for aluminum 6061 cantilevers at MINOR UNCLE.

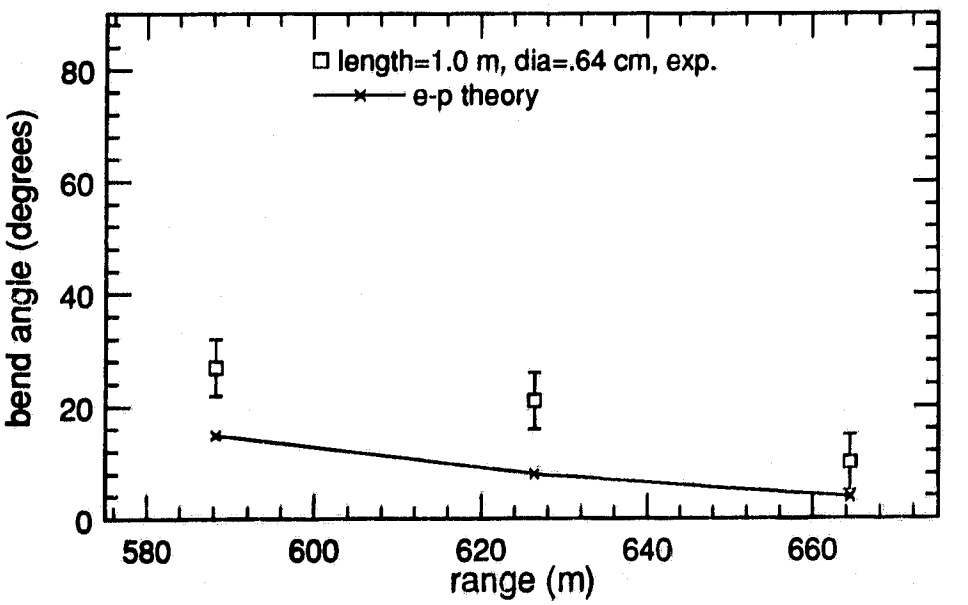

Figure C.9: Experimental and theoretical deformation angle versus range for aluminum 6061 cantilevers at MINOR UNCLE.

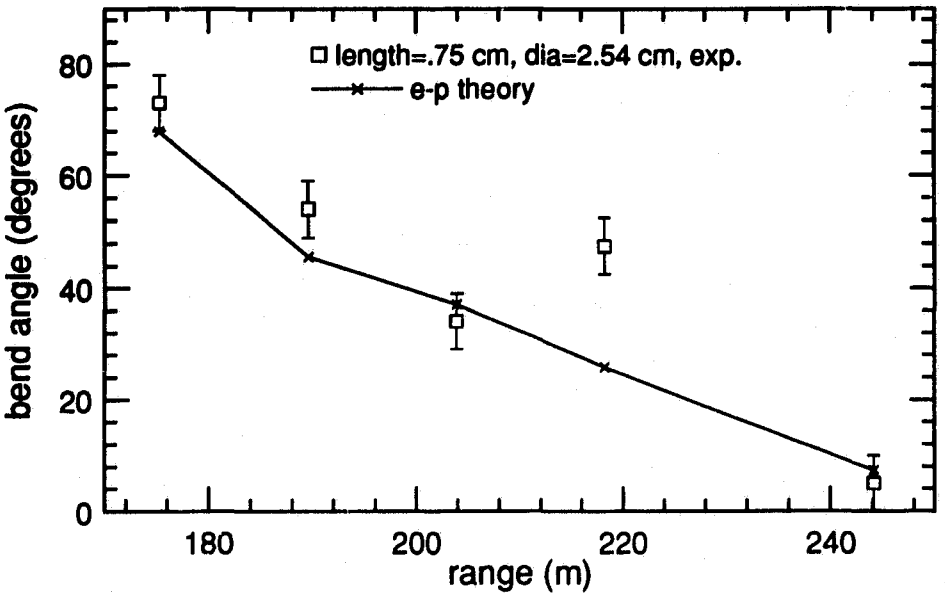

Figure C.10: Experimental and theoretical deformation angle versus range for steel 1018 cantilevers at MINOR UNCLE.

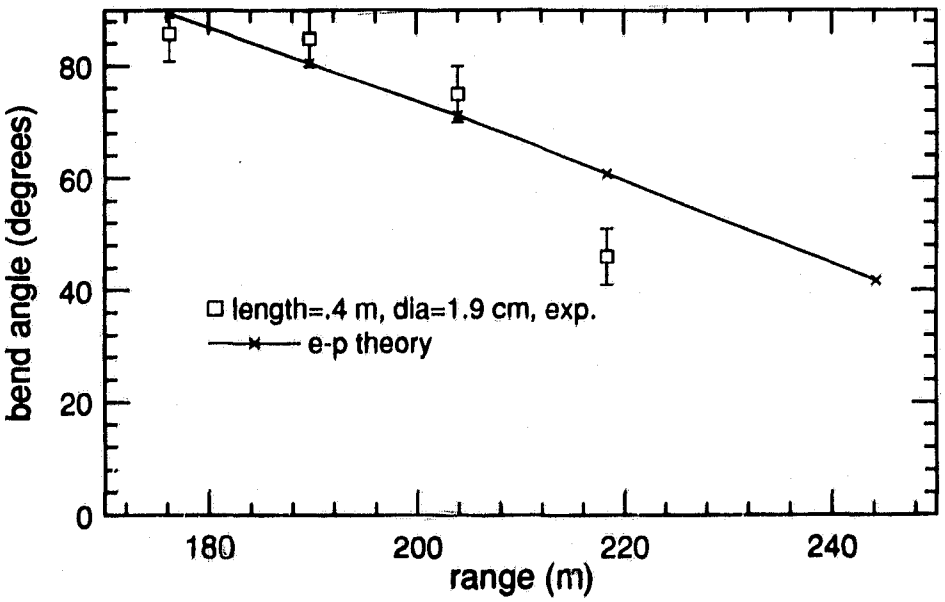

Figure C.11: Experimental and theoretical deformation angle versus range for aluminum 6061 cantilevers at DISTANT IMAGE.

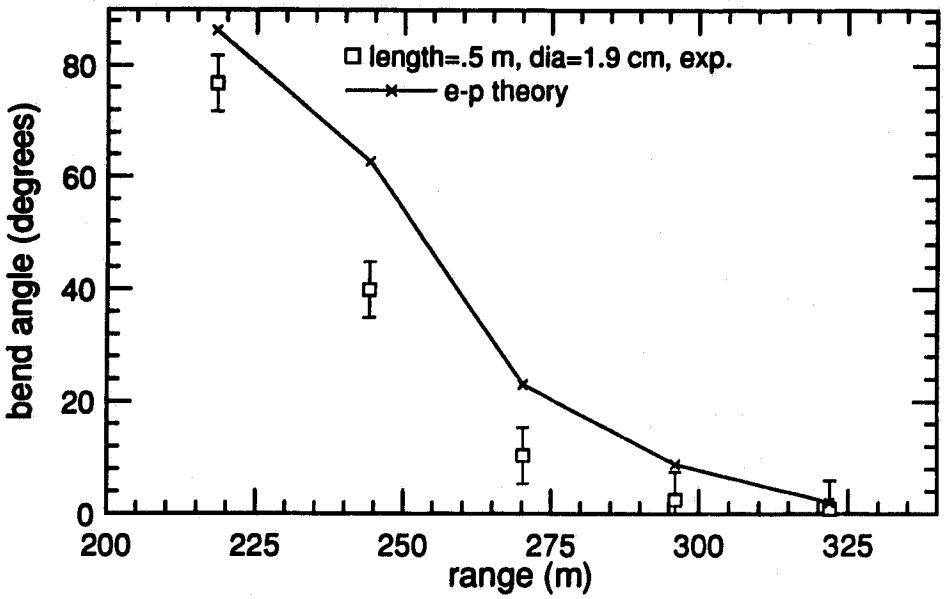

Figure C.12: Experimental and theoretical deformation angle versus range for aluminum 6061 cantilevers at DISTANT IMAGE.

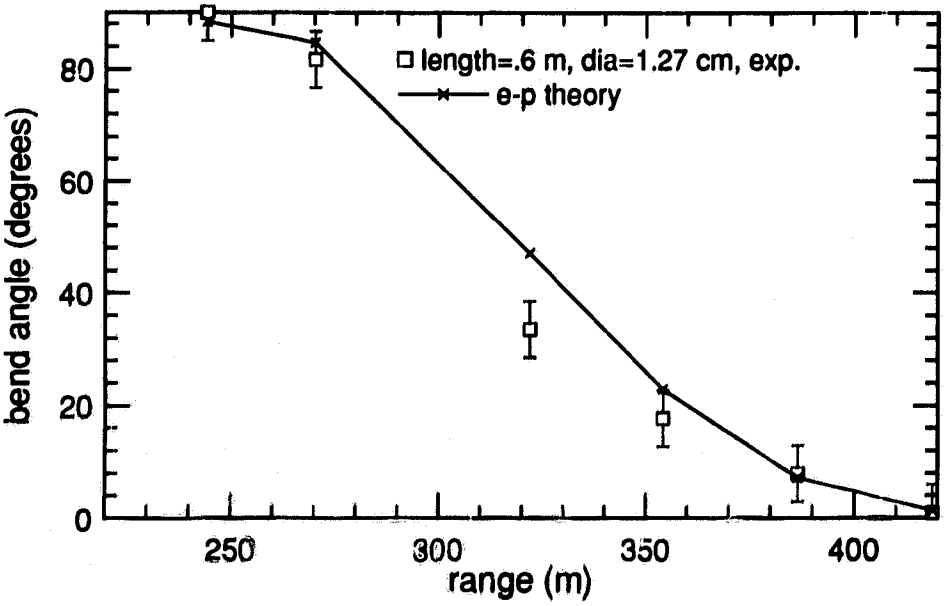

Figure C.13: Experimental and theoretical deformation angle versus range for aluminum 6061 cantilevers at DISTANT IMAGE.

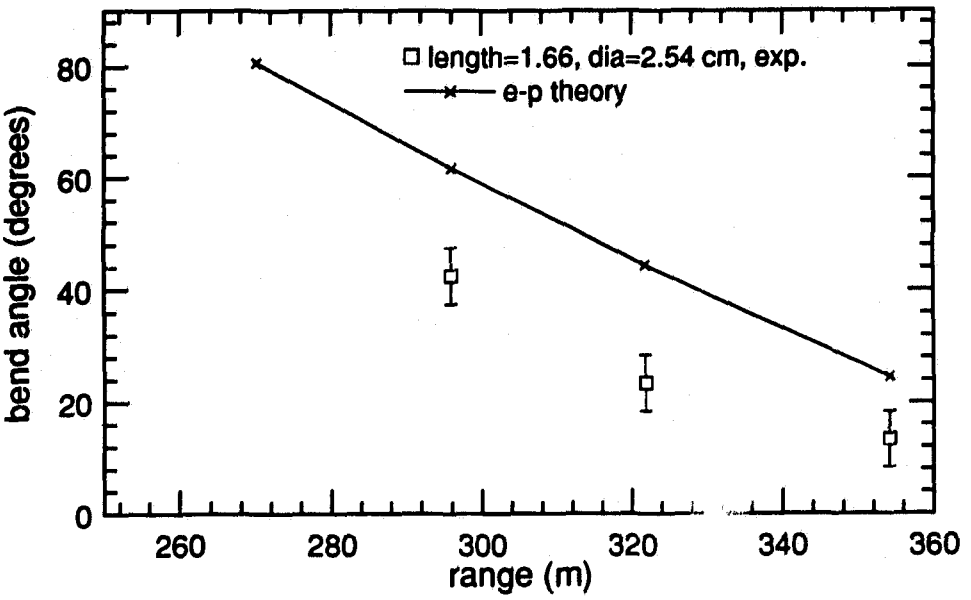

Figure C.14: Experimental and theoretical deformation angle versus range for aluminum 6061 cantilevers at DISTANT IMAGE.

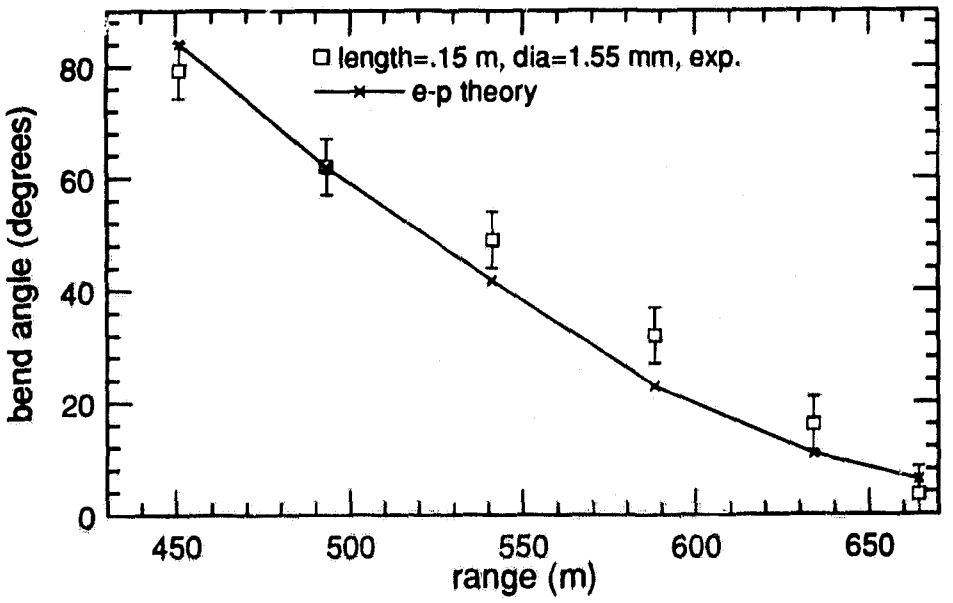

Figure C.15: Experimental and theoretical deformation angle versus range for aluminum 4043 cantilevers at DISTANT IMAGE.

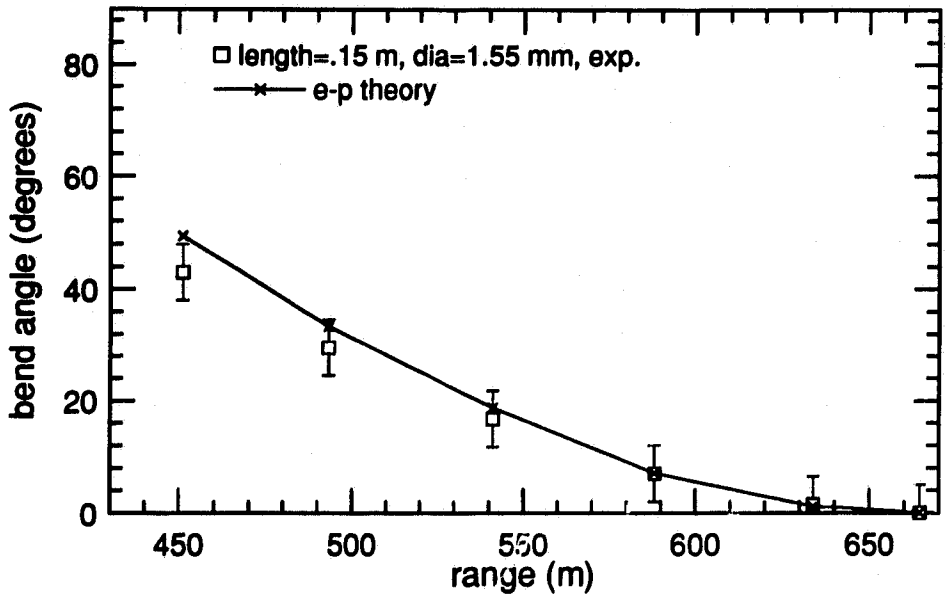

Figure C.16: Experimental and theoretical deformation angle versus range for aluminum 5056 cantilevers at DISTANT IMAGE.

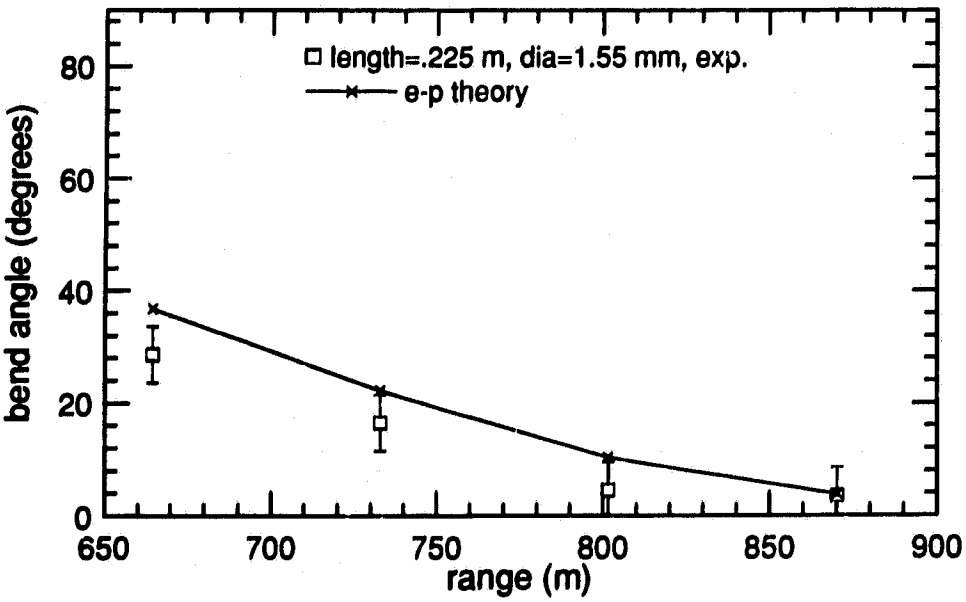

Figure C.17: Experimental and theoretical deformation angle versus range for aluminum 4043 cantilevers at DISTANT IMAGE.

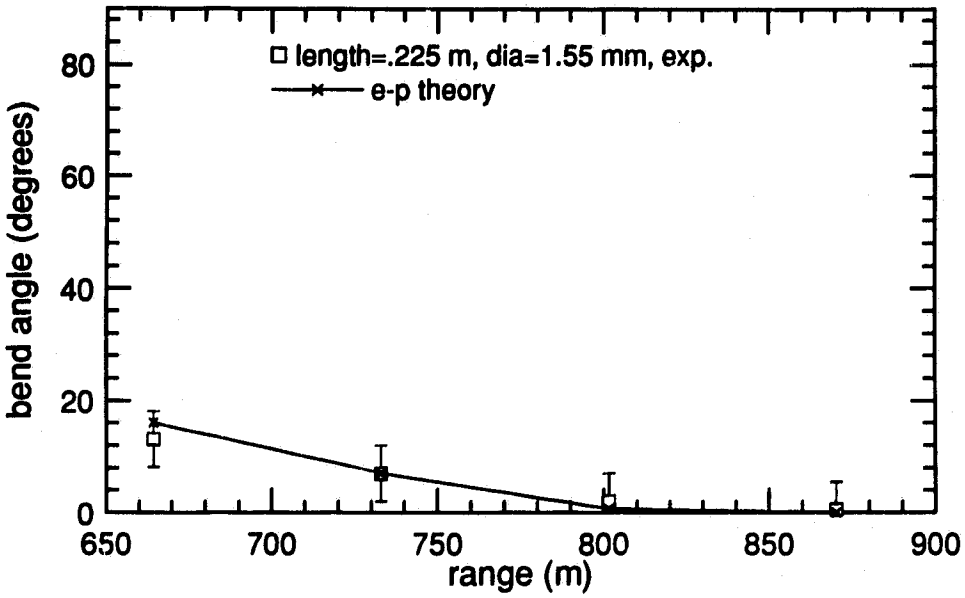

Figure C.18: Experimental and theoretical deformation angle versus range for aluminum 5056 cantilevers at DISTANT IMAGE.

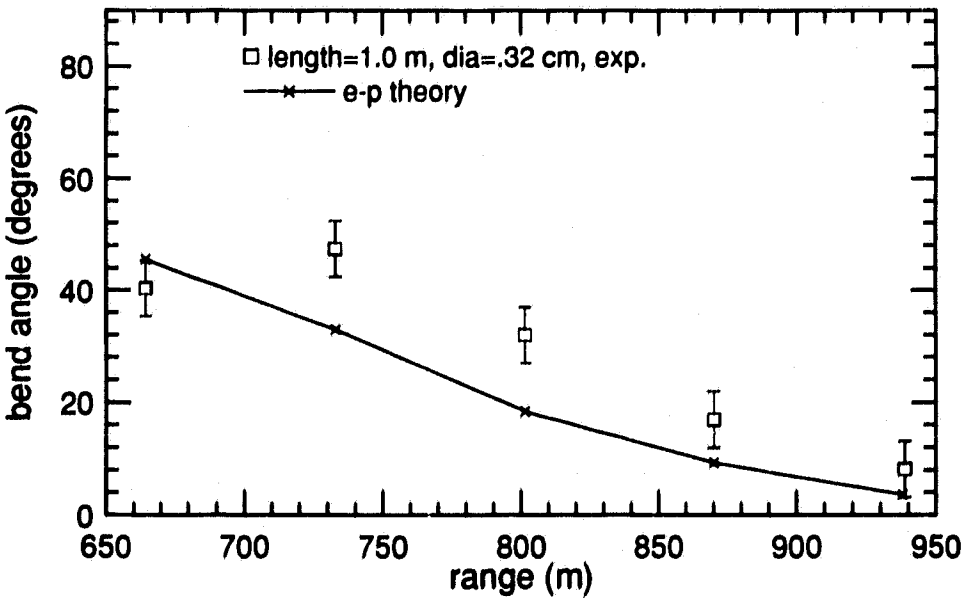

Figure C.19: Experimental and theoretical deformation angle versus range for aluminum 6061 cantilevers at DISTANT IMAGE.